THE EFFECT OF SENSITIZATION ON THE CORROSION SUSCEPTIBILITY AND TENSILE PROPERTIES OF AA5083 ALUMINUM

A Thesis Submitted to the College of Graduate Studies and Research in Partial Fulfillment of the Requirements for the Degree of

Master of Science

in the Department of Mechanical Engineering

University of Saskatchewan

Saskatoon, Saskatchewan

Canada

By

Olusegun John Adigun

PERMISSION TO USE

In presenting this thesis in partial fulfillment of the requirements for the Masters degree from the University of Saskatchewan, I agree that the Libraries of this University may make it freely available for inspection. I further agree that permission for copying of this thesis in any manner, in whole or in part, for scholarly purposes may be granted by Professors S. Yannacopoulos and I. N. A. Oguocha who supervised my thesis work or, in their absence, by the Head of Department of Mechanical Engineering or the Dean of the College in which my thesis work was done. It is understood that any copying or publication or use of this thesis or parts thereof for financial gain shall not be allowed without my written permission. It is also understood that due recognition shall be given to me and to the University of Saskatchewan in any scholarly use which may be made of any material in my thesis.

Request for permission to copy or to make other use of material in this thesis in whole or part should be addressed to:

Head of the Department of Mechanical Engineering

57 Campus Drive

University of Saskatchewan

Saskatoon, Canada, S7N 5A9

ABSTRACT

Aluminum-magnesium alloy (AA5083-H116) is primarily designed for marine applications such as in ship hulls and deckhouses. Its excellent combination of physical and mechanical properties makes it useful for other applications such as aircraft construction, military equipment and vehicles and automobiles.

This study investigated the effect of time and temperature of sensitization on the mechanical and chemical properties of AA5083-H116 such as tensile strength, yield strength and susceptibility to intergranular corrosion (IGC). Test specimens were sensitized at various temperatures (80^{o}C, 100^{o}C, 175^{o}C and 200^{o}C) for up to 672 h (4 weeks). Microhardness measurements, tensile testing, scanning electron microscopy (SEM), energy dispersive X-ray spectrometry (EDS), inductively coupled plasma/mass spectrometry (ICP/MS) and nitric acid mass loss tests (NAMLT) were used to evaluate these effects.

The results obtained show that the mechanical properties of AA5083-H116 deteriorated with increasing sensitization temperature and time. The adverse effect on these properties was attributed to reduction in dislocation density and recrystallization at higher temperatures. The as-received specimens and those sensitized at 80^{o}C showed no susceptibility to IGC. However, at higher sensitization temperatures and longer resident

times, resistance to IGC decreased dramatically. The reduction in IGC resistance was attributed to precipitation of secondary phases along the grain boundaries.

ACKNOWLEDGEMENT

I would like to express my sincere appreciation to my supervisors, Professors S. Yannacopoulos and I. N. A. Oguocha for their timely advice, constant guidance and thoughtful insights throughout the research. Special thanks to Alcan Aluminum, Kingston, Ontario, for the supply of the test material. My appreciation goes to the members of my supervisory committee, Prof. M. Mahfoud and Prof. R. Evitts. Technical assistance provided by Mr. Dave Crone, Mr. Hans Steinmetz and Mr. D. Fisher (Civil Engineering Department), Dr. R. O. Idem and his staff (Lauren Erickson and Robyl Fahman) at the University of Regina and John Vandorp at the University of Manitoba, Winnipeg, is sincerely acknowledged.

I appreciate the support and encouragement I received from my parents and siblings in Nigeria and from my colleagues in the Materials Science Research Group. Financial assistance from NSERC grant to my supervisors, scholarship from Mechanical Engineering Department and study leave from Ladoke Akintola University of Technology (LAUTECH), Ogbomoso, Nigeria are gratefully acknowledged.

DEDICATION

This thesis is dedicated to my darling wife, (Oyinlade Dorcas) and lovely children, (Oluwaseyi Esther) and (Oluwasayo Samuel).

TABLE OF CONTENTS

LIST OF TABLES

LIST OF FIGURES

NOMENCLATURE

Abbreviations

AEM	Analytical electron microscopy
CF	Corrosion fatigue
CFC	Corrosion fatigue cracking
EELS	Electron energy loss spectrometry
CERT	Constant extension rate testing
EIC	Environmentally induced corrosion
HIC	Hydrogen-induced cracking
IGC	Intergranular corrosion
IGSCC	Intergranular stress corrosion cracking
ICP/MS	Induced coupled plasma/mass spectroscopy
LD	Longitudinal direction
NAMLT	Nitric acid mass loss test
OCP	Open circuit potential
ppb	Parts per billion
SEM	Scanning electron microscope
SCC	Stress corrosion cracking
STEM	Scanning transmission electron microscopy
TB	Solution heat treated and naturally aged

TF	Solution heat treated and artificially aged
TEM	Transmission electron microscopy
TD	Transverse direction
LD	Longitudinal direction
VHN	Vickers Hardness Number
XRD	X-ray diffractrometry

1. INTRODUCTION

1.1 Background

The use of aluminum alloys is increasing in automobile, marine, aerospace and sport equipment industries due to their high strength-to-weight ratio and other useful properties. Light-weight strong materials are desired in the transportation industry in order to increase fuel efficiency without impairing safety. This has led to an increased interest in aluminum alloys with properties adequate to serve as structural elements [1-3]. Aluminum-magnesium alloys (AA5XXX series) are choice materials for components that require moderate strength, formability, atmospheric corrosion resistance and weldability. As produced, Al-Mg alloy AA5083 with 4.5 wt% Mg meets these goals. However, aluminum alloys with greater than 3 wt% Mg show susceptibility to intergranular corrosion (IGC) and stress corrosion cracking (SCC) following low temperature heat treatments or thermal exposures as low as 90^{o}C [4-5]. The use of 5XXX series aluminum alloys is therefore limited as a result of this anticipated susceptibility to IGC and SCC at elevated temperatures. SCC failures in aluminum alloys are generally intergranular, the microstructure along the grain boundaries play a primary role in determining SCC susceptibility.

SCC is a form of environmentally induced cracking (EIC), which is a process of gradual deterioration, degrading or damage of a material resulting from combined action of mechanical stress and corrosive environment. Different types of EIC occur in many engineering alloys over a broad range of environments and affect structural performance and reliability. These include SCC, corrosion fatigue cracking (CFC) and hydrogen-induced cracking (HIC). In the case of SCC, cracking is caused by static tensile stress in a material in the presence of a specific corrosion medium. Corrosion fatigue cracking is the process in which a metal fractures prematurely under conditions of simultaneous corrosion and cyclic loading at a lower stress level or a lower number of cycles than would be required in the absence of the corrosive environment. Also, hydrogen-induced cracking occurs when atomic hydrogen from either reduction of water or acid penetrates and diffuses into the structure of an alloy resulting in brittle mechanical fracture.

Aluminum alloy AA5083 is a medium strength, non-heat treatable alloy with excellent atmospheric corrosion resistance. It is one of the most widely used aluminum alloys, especially in the transportation industry. Typical applications for this alloy include ship and boat hulls, aircraft construction, TV towers, drilling rigs, missile components, armour plates and tanker lorries. However, this alloy is prone to sensitization which gives rise to IGC and SCC when exposed to a temperature range of 50 to 200^{o}C for long periods of time [6]. This has limited its use to those applications where the service temperature is less than 65^{o}C [7].

Sensitization is the precipitation of a new phase at grain boundaries of an alloy upon exposure to elevated temperatures for a certain length of time. Different metallic alloys have specific phases that crystallize at their grain boundaries. For example, chromium carbide precipitates at the grain boundaries of austenitic stainless steels upon sensitization. Other aluminum alloys and metallic alloys such as brass and carbon steels are also prone to sensitization in different environments. Many researchers [3-30] have reported that SCC of AA5083 is due to the precipitation of β phase (Al_3Mg_2) at grain boundaries. Thus, understanding the decomposition of magnesium in this alloy is of paramount importance to finding solutions to the stress corrosion related problems which always arises as a result of intergranular corrosion.

1.2 Motivation

Studies [3-30] carried out on AA5083 alloy with various tempers such as O and H321 have revealed that precipitation of β phase at the grain boundaries is the cause of SCC in this alloy. Temper O is a simple annealing of the material in which there is lowest strength and greatest ductility while H321 is a strain hardened temper in which the amount of strain hardening is controlled during hot and cold working. To the best of the author's knowledge, no work carried out on the intergranular corrosion and SCC of AA5083-H116 has been reported in the open literature. Temper H116 is a special strain hardening treatment with special control of temperature for enhancement of corrosion resistance of aluminum-magnesium alloys. AA5083 alloys with H321 and H116 tempers have been materials of choice over the years for manufacturing ship hulls and tanker lorries because they posses good combination of properties. However, it was

reported recently that boat hulls manufactured from AA5083-H116 have severe cracks all over the surfaces that could lead to waste of property and loss of life [10]. Consequently, the need to ensure adequate security of life and property and better understanding of AA5083-H116 behaviour at elevated temperature calls for detailed study of its IGC which often leads to SCC.

1.3 Objectives

The main objectives of this study are:

1. To investigate the effect of sensitization on the IGC and mechanical properties of AA 5083–H116.
2. To relate the microstructure to sensitization of AA5083-H116.
3. To design and construct a test apparatus for studying the SCC of AA5083-H116.

The potential contributions of this study include:

1. Complementing the existing database and improving knowledge of stress corrosion cracking of sensitized AA5083–H116.
2. Determining whether AA5083-H116 should continue to be used for marine applications.

1.4 Methods of Evaluation

The following tests were performed to achieve the aforementioned objectives.

1. Susceptibility to intergranular corrosion by mass loss after exposure to nitric acid (ASTM G 67).
2. Tensile testing and hardness measurements.
3. Metallography examination and fractography using electron microscopy (SEM, TEM).

1.5 Thesis Outline

There are five chapters in this thesis. Chapter 1 provides general information about aluminum-magnesium alloys, environmentally induced cracking, objectives and motivation for the thesis. Chapter 2 gives a comprehensive literature review of intergranular corrosion and stress corrosion cracking of aluminum alloys. Chapter 3 describes the materials and experimental methods employed in this study. Results obtained from this research are reported and discussed in Chapter 4. Conclusions from the results and recommendations for future work are presented in Chapter 5. A list of references and the appendix are included following Chapter 5.

2. LITERATURE REVIEW

This chapter contains a survey of aluminum alloy systems and their properties. The three categories of environmentally induced cracking, namely: stress corrosion cracking (SCC), corrosion fatigue (CF) and hydrogen induced cracking (HIC) are differentiated. The mechanisms of SCC are reviewed. Finally, the intergranular corrosion (IGC) and SCC of aluminum alloys and other alloys are discussed.

2.1 Aluminum Alloy Systems

Aluminum is a silvery white reactive metal that is usually covered by a film oxide coating. This renders it inert to atmospheric condition, but it is attacked by alkalis. It does not corrode like steel. However, the commercial usefulness of pure aluminum is limited due to its low strength. As such, strength improvement is a major objective in the design of aluminum alloy systems which are now being widely used in different applications. Aluminum is a very reactive element and, as a result, most of the existing metallic elements readily alloy with it. However, only a few are important ingredients in commercial alloys. Aluminum alloy systems can be grouped into two categories, namely: cast and wrought aluminum alloys [28,30]. The mode of manufacturing is the major difference between wrought and cast aluminum alloys.

Wrought aluminum alloys are the alloys produced from metal ingots through forming processes such as rolling, extrusion and forging. A system of four-digit numerical designations is used for identification of wrought aluminum alloys. The first digit indicates the alloy group while the last two digits identify the aluminum alloy or aluminum purity. The second digit indicates the modification on the original alloy or impurity limits [26,30]. Table 2.1 shows the classification of wrought aluminum alloys [30].

Wrought aluminum alloys can be further grouped into heat treatable and non-heat treatable (work hardening) alloys. The former are subjected to thermal treatment at elevated temperature, quenched and aged (natural or artificial) while the latter depend upon plastic deformation by rolling or drawing for the development of microstructure and properties required for commercial applications. Most of the alloys in the 2XXX (Aluminum-Copper-Magnesium), 6XXX (Aluminum-Magnesium-Silicon) and 7XXX (Aluminum-Zinc-Magnesium) groups are heat treatable. Non-heat treatable alloys include all the various grades of pure aluminum and all other alloys in which strength is developed by solid solution hardening and strain hardening from annealed temper. The useful properties found in non-heat treatable alloys result from elements that are present or added as major impurities. Alloys in the 3XXX (Aluminum-Manganese), 4XXX (Aluminum-Silicon) and 5XXX (Aluminum-Magnesium) groups are mostly non-heat treatable.

Table 2.1. Classification of wrought aluminum alloys [30].

Aluminum alloys grouped by major elements	
Aluminum, 99.9 percent minimum and greater	1XXX
Copper	2XXX
Manganese	3XXX
Silicon	4XXX
Magnesium	5XXX
Magnesium and Silicon	6XXX
Zinc	7XXX
Other element	8XXX
Unused series	9XXX

Cast aluminum alloys are those aluminum alloys produced by casting, which is simply the process of filling a mould with a liquid metal that then solidifies in the shape of the mould cavity. Casting is used to produce complex structures and metal ingots. Cast aluminum alloys also include both heat treatable and non-heat treatable groups. A system of four-digit numerical designations is used for cast alloys. The first digit indicates the group; the next two digits identify the aluminum alloy or aluminum purity. The last digit, which is separated from others by a decimal point, indicates the product form. A serial letter before the numerical designation indicates a modification of the original alloy or impurity limits. Table 2.2 shows the classification of cast aluminum alloys [30].

Table 2.2. Cast aluminum alloy groups [30].

Aluminum alloys grouped by major elements	
Aluminum, 99.9 percent minimum and greater	1XX.X
Copper	2XX.X
Silicon, with added copper and / or magnesium	3XX.X
Silicon	4XX.X
Magnesium	5XX.X
Zinc	7XX.X
Tin	8XX.X
Other element	9XX.X
Unused series	6XX.X

2.2 Temper Designations

The non-heat treatable wrought materials whose strength is attained by alloying and cold working (strain hardening) are referred to as work hardening alloys. Work hardening alloys and heat treatable alloys have different temper designations. Aluminium-magnesium alloys are work hardening alloys; therefore, temper designation of work hardening alloys alone will be discussed in this section.

The degree of work hardening is expressed as a temper ‘H’ with different numbers. For any of the alloys, the higher the number, the greater the amount of cold deformation applied to the material, indicating increasing strength. The amount of cold work is usually expressed as the reduction of cross-sectional area which must be employed to

attain a given temper. Table 2.3 shows the temper designations for strain-hardened aluminum alloys. The severely cold worked or full-hard condition (H18 temper) is usually obtained with cold work approximately equal to 75% reduction in area. The H19 temper identifies products with substantially higher strengths because of greater reduction. The H16, H14 and H12 tempers are obtained with lesser amounts of cold working, and they represent three-quarter-hard, half-hard, and quarter-hard conditions, respectively. A combination of strain hardening and partial annealing is used to produce the H28, H26, H24, and H22 series tempers; the products are strain hardened more than is required to achieve the desired properties and then are reduced in strength by partial annealing. A series of strain-hardened and stabilized tempers such as H38, H36, H34, and H32 are used for aluminum-magnesium alloys.

2.3 Properties of Wrought Aluminum Alloys

The properties to be discussed in this section are classified into three groups, namely: physical, mechanical and chemical properties. These properties are function of the manufacturing process which determines the microstructure of the materials.

2.3.1 Physical Properties

Physical properties of a given alloy do not depend much on the size, shape and temper or heat treatment condition as do the mechanical properties. Physical properties of some alloys have been established for different tempers or heat treatment conditions.

Table 2.3. Temper designations for strain-hardened alloys [26]

Temper	Descrpition
F	As-fabricated. No control over the amount of strain hardening.
O	Annealed recrystallized. Temper with the lowest strength and greatest ductility
H1	Strain hardened
H2	Strain hardened and partially annealed.
H3	Strain hardened and stabilized.
H112	Strain hardened during fabrication.
H321	Strain hardened during fabrication.
H116	Special strain hardened, corrosion resistant temper for aluminum-magnesium alloys

2.3.1.1 Density

The density of pure aluminum is 2.70 g/cm^3 but it increases slightly with the level of impurity. The manganese-bearing alloy AA3103 has a density of 2.73 g/cm^3. In AA3105, any increase due to manganese is counteracted by the magnesium content. In the 5XXX series alloys, there is a general decrease in density with increase in magnesium but again the manganese and chromium contents modify the effect of magnesium. The densities of 6XXX series alloys are similar to that of unalloyed aluminum. The net effect of alloying elements in the 2XXX series is to increase densities to the range 2.75-2.80 g/cm^3. The densities of the 7XXX series alloys fall into the same range as the 2XXX series [28].

2.3.1.2 Thermal and Electrical Conductivities

Pure aluminum is a very good thermal and electrical conductor. The thermal conductivity of unalloyed aluminum ranges from 226 to 244 W/m^{o}C. As the level of impurity reduces, the thermal conductivity increases. For the 3XXX series having small contents of manganese or manganese and magnesium the value falls to 172 W/m^{o}C. In the 5XXX series, the thermal conductivity decreases with increasing magnesium content. For 5005 and 5083, it is 201 and 109 W/m^{o}C, respectively. The heat treatable 6XXX series alloys have thermal conductivity values from 172-197 W/m^{o}C for the TB temper and 184-214 W/m^{o}C for the TF temper. For 2XXX series, values of 151 and 152 W/m^{o}C, and 151-168 W/m^{o}C are reported for TB temper and alloys which respond to artificial ageing, respectively [28]. The 7XXX series alloys have values of 130-134 W/m^{o}C for the TF temper. Electrical conductivity is quantified in terms of the international annealed copper standard (IACS). The conductivities of alloys decreases with increasing alloy content.Aluminum alloys of the 3XXX and 5XXX series have electrical conductivities in the range of 28-50% IACS [28].

2.3.1.3 Elasticity

The elastic moduli of aluminum alloys are approximately one-third of those of carbon steels. The low value of these moduli may be of advantage in some circumstances such as when loaded under shock conditions. The low value of elastic modulus indicates that, for the same rigidity, an aluminum beam should have a greater moment of inertia than a steel beam. The geometrical shape of the section and the elastic constants, modulus of

elasticity and rigidity, are pertinent factors controlling stability and prevention of failure due to buckling torsion and local failure rather the strength properties.

2.3.2 Mechanical Properties

2.3.2.1 Tensile Strength

Internal structural changes due to work hardening have serious effects on mechanical properties such as tensile strength. The forms of typical stress-strain curves for aluminum and its alloys are shown in Figure 2.1. The tensile properties normally determined are proof stress, tensile strength, yield strength and percent elongation. Cold working increases the strength at the expense of ductility, as measured by the percentage of elongation in a tensile test and by reduced formability in operations such as bending and drawing. Consequently, the strain hardened tempers are not usually used where high ductility and formability are required.

2.3.3 Chemical Properties

Aluminum is a very reactive element and is easily oxidized. In the form of commercially pure aluminum and in many of its alloys, the metal possesses high resistance to the effects of weather and of many products of the chemical, food and allied industries. The high resistance of aluminum to corrosion is due to the formation of thin oxide film

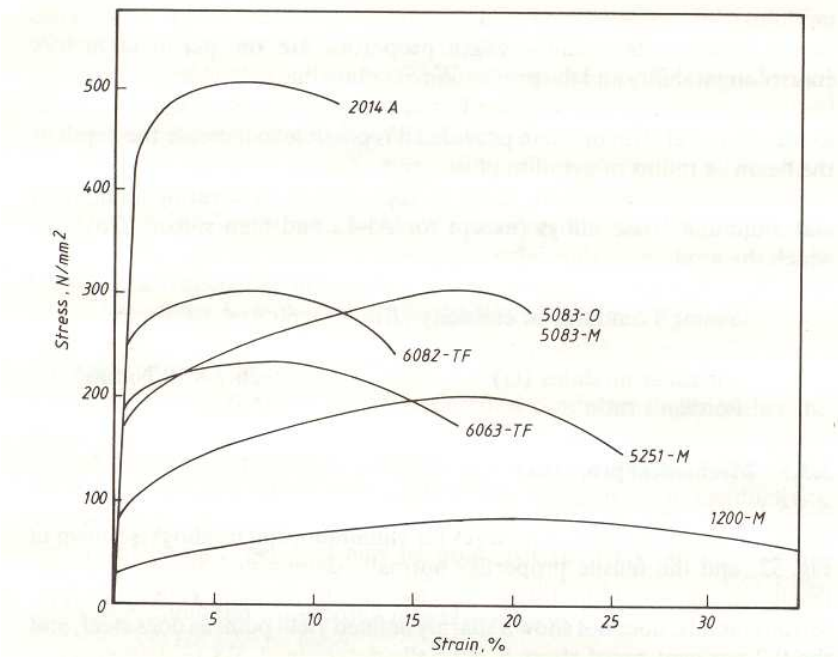

Figure 2.1. Stress-strain curves for typical wrought aluminum alloys [29].

immediately after the metal is exposed to air and slowly increases in thickness until no further oxidation takes place unless the film is ruptured. It forms more rapidly and attains a greater thickness at high temperature. The oxide film renders aluminum passive and is not soluble in water.

The oxide is composed of two layers [31], namely: (i) inner (barrier) oxide and (ii) outer oxide. The inner oxide next to the metal is a compact amorphous barrier layer whose thickness depends on the environmental temperature. The barrier layer is in turn covered by thicker and more permeable outer layer of hydrated oxide. Most of the interpretations of the aluminum corrosion process are developed in terms of the chemical properties of these oxide layers. The conditions for thermodynamic stability of the oxide film are expressed by Pourbaix (potential-pH) diagram shown in Figure 2.2.

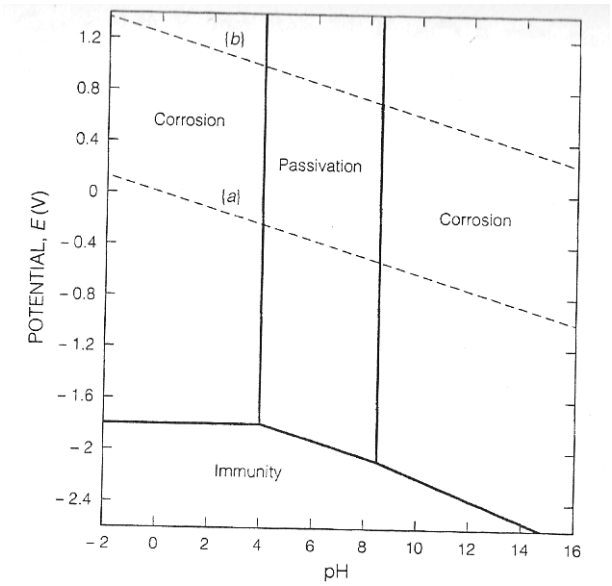

Figure 2.2. Pourbaix diagram for aluminum with an $Al_2O_3.3H_2O$ film at 25°C (SHE). Note: (a) hydrogen and (b) oxygen lines [26].

Aluminum is passive (protected by its oxide film) in the pH range of about 4 to 8.5. Beyond the limits of its passive range, aluminum alloys corrode beyond the limit in aqueous solutions because their oxides are soluble in several acids and bases yielding Al^{3+} ions in the former and AlO_2^- ions in the latter.

2.3.4 Effect of Directionality on Properties.

Directionality generally is not critical in sheet and thin plate products, but it assumes importance as the section thickness increases in plate, extrusions, and forgings. In the plates or thicker products, directionality influences mechanical properties as well as other characteristics such as resistance to stress-corrosion cracking. The directional effects are related to the design of the section or to the direction of working. Figures 2.3

and 2.4 show directional metallurgical structures and identify grain direction in flat rolled products and rolled rod of 7075-T6 alloy. Tensile and yield strengths along different directions for 7075-T6 are shown on Table 2.4. In general, tensile strengths are higher in the longitudinal direction than in the long and short transverse directions. Properties along longitudinal direction are always specified for work hardened materials.

Table 2.4. Effect of directionality on mechanical properties 7075-T6 [29].

	Tensile strength		Yield strength		Elongation in 50mm
Test direction	MPa	Ksi	MPa	Ksi	%
Longitudinal	505	73.2	420	60.9	9
Long transverse	490	71.1	405	58.8	4
Short transverse	475	68.9	400	58.0	3

2.4 Environmentally Induced Cracking

Environmentally induced cracking (EIC) is a general term for brittle mechanical failures resulting from a combined action of mechanical stress and corrosive environment. This process leads to crack initiation, propagation and final fracture of materials. EIC can be grouped into three types of attack, namely: stress corrosion cracking (SCC), corrosion fatigue (CF) and hydrogen induced cracking (HIC). Figures 2.5 (a)-(c) show micrographs of SCC, CF and HIC phenomena in plain carbon steel. They are differentiated by the nature of the stress present. SCC is the brittle fracture at relatively low constant tensile stress of an alloy exposed to a specific corrosive environment.

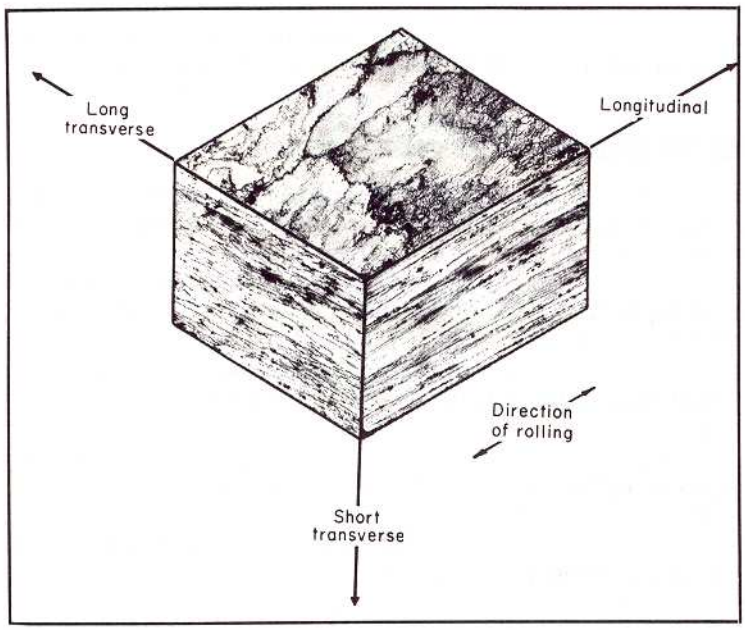

Figure 2.3. Composite of micrographs of flat rolled 7075-T6 [29].

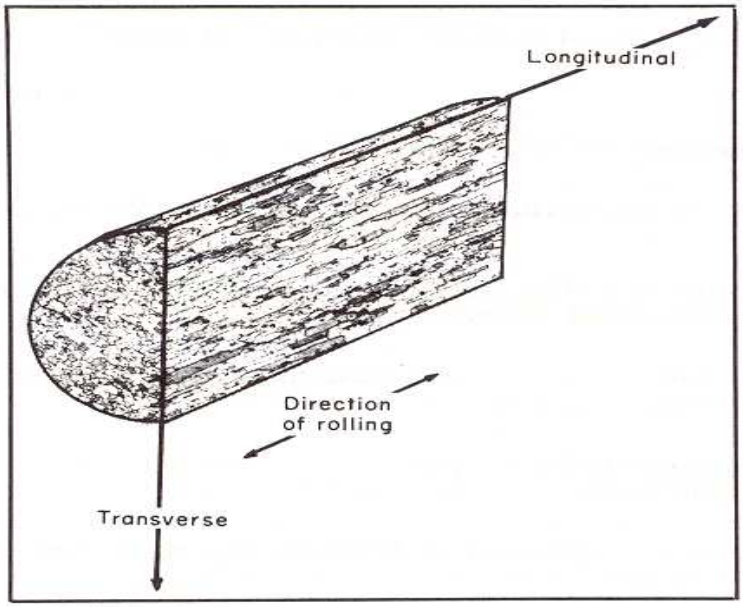

Figure 2.4. Composite of micrographs of 7075-T6 rolled rod [29].

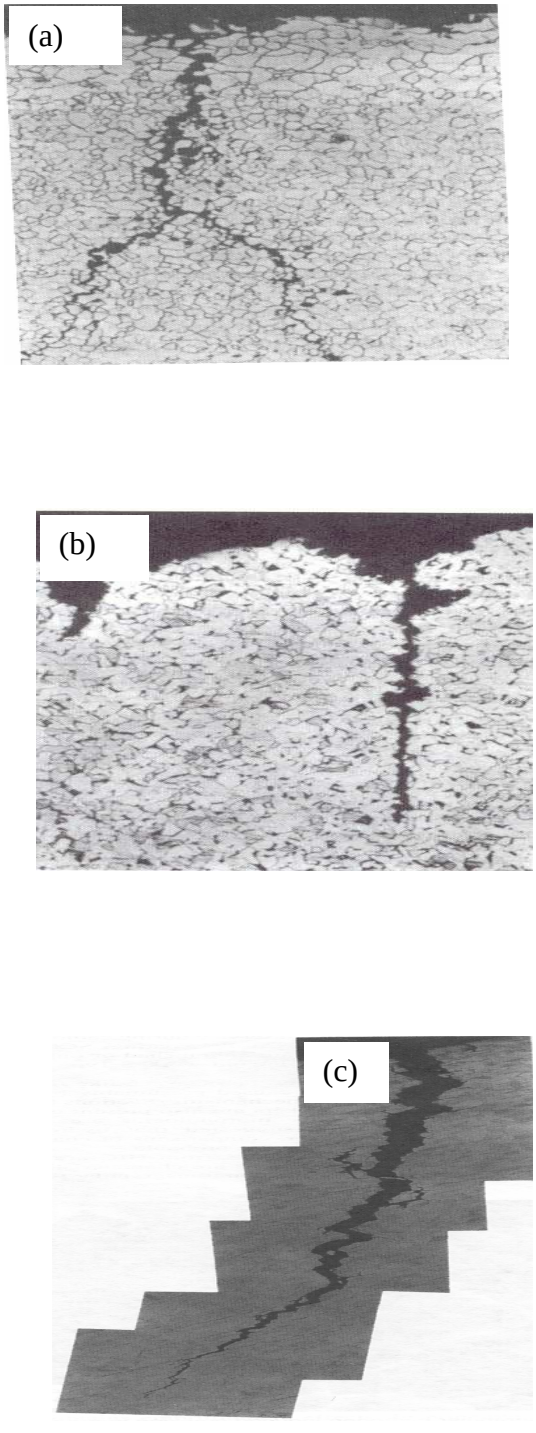

Figure 2.5. (a) Stress corrosion cracking of carbon steel, (b) Corrosion fatigue of carbon steel and (c) Hydrogen-induced cracking [32].

There are three conditions that must be satisfied for SCC to occur: a susceptible alloy, tensile stress, and corrosive environment [32].

Some alloys such as low carbon steels, brasses, stainless steels, titanium and aluminum alloys have been found to suffer stress corrosion cracking under specific conditions. For example, hot aqueous chloride solutions readily crack stainless steels and aluminum alloys such as 2XXX, 5XXX, and 7XXX but do not have the same effect on carbon steels. Also, carbon steels can experience SCC in ammonium nitrate solutions. The term SCC is normally used to describe failures in metallic alloys alone. Nevertheless, other classes of materials also exhibit SCC. Ceramics exhibit EIC [31] and polymeric materials constantly exhibit craze cracking as a result of a combination of applied stress and corrodent [33-36]. Also, mechanical properties of composites degrade due to the attack of the matrix, the reinforcing phase, or the matrix-reinforcement interface by the corrosive environment. If crack propagation results during static loading, then this degradation is SCC.

Corrosion fatigue is a failure caused by the simultaneous action of a fluctuating stress and corrosion attack. It is similar to SCC but requires neither a specific corrodent nor low corrosion rate. It cracks slowly and corrosion products are more likely to be present in the crack. All metals which are susceptible to corrosion are susceptible to corrosion fatigue in any corrosive environment and this is not limited to certain metallurgical conditions of the metal. HIC is caused by hydrogen diffusion into the alloy lattice when hydrogen evolution reaction produces atomic hydrogen at the surface during corrosion,

electroplating and cathodic protection. Cathodic polarization suppresses both SCC and CF but accelerates HIC [37].

2.5 Mechanisms of Stress Corrosion Cracking

Stress corrosion cracking occurs when certain critical conditions are achieved. These conditions include electrochemical, mechanical and metallurgical factors. A change in any of these factors may eliminate SCC; therefore, a clear understanding of these critical factors is important in system design. For years, the mechanism of SCC in aluminum alloys was believed to be primarily electrochemical [38-40] but later, hydrogen embrittlement of grain boundaries was found to play a major role in the SCC of high-strength steels and titanium. D. O. Sprowls [39] later reported that no such mechanism appeared to play a role in the SCC of aluminum alloys. However, it was reported by Gest *et al.* [41] and Albrecht [42] that hydrogen is unable to enter 7075 alloy cathodically protected at -1.5 V saturated calomel electrode (SCE) at a sufficient rate to cause hydrogen embrittlement but at -2.0 V SCE the hydrogen permeation rate rises substantially, and at such a potential SCC occurred. It was reported by Koch [43] that atomic hydrogen is absorbed by aluminum and causes embrittlement of certain aluminum alloys. The role of hydrogen in the SCC of aluminum-zinc-magnesium-copper alloys was confirmed by Green *et al.* [44] and Scamans *et al.* [45]. Tuck [46] reported that magnesium hydride formation can occur in aluminum-magnesium alloy during exposure to moist air. Change in SCC susceptibility of aluminum-zinc-magnesium alloys may be related to the magnesium content of the surface oxide film, which can affect the ease of hydrogen entry into the metal [47]. SCC failures in

aluminum alloys are generally intergranular, the microstructure along the grain boundaries plays a primary role in determining SCC susceptibility.

Several mechanisms have been proposed for the occurrence of stress corrosion cracking and they can be grouped into two basic categories: anodic and cathodic mechanisms. Active dissolution and removal of material from the crack tip is an anodic mechanism while hydrogen evolution, absorption, diffusion and embrittlement are cathodic mechanisms. The sequence of events involved in the SCC process are crack initiation, crack propagation and final fracture.

2.5.1 Crack-Initiation Physical Processes

There are three different types of crack-initiation physical processes, namely: (i) crack-initiation at surface discontinuities, (ii) crack initiation at corrosion pits and (iii) crack-initiation by intergranular corrosion or slip dissolution. These processes will be discussed further in the following paragraphs.

(i) Crack initiation at surface discontinuities

Stress corrosion cracking frequently initiates at pre-existing or corrosion-induced surface features. These features include grooves, laps or burrs caused by fabrication processes. The highly sensitized recrystallized material could also become the site of crack initiation by intergranular corrosion (IGC). Figure 2.6(a) shows lap that was recrystallized during welding and which could then act as a crevice where deleterious

anions or cations concentrate. Figure 2.6(b) shows a cold worked layer and surface burrs that can also aid crack initiation.

(ii) Crack initiation at corrosion pits.

Stress corrosion cracks can initiate at pits that form during cleaning operations such as pickling of type 304 stainless steel before fabrication and exposure to service environment.

Pits form as a result of breakdown of the film or at the inclusions that intersect the free surface. Parkins *et al.* [48] and Tamaki *et al.* [49] had shown that both pitting and SCC potentials were identical for steel in nitrite solutions. SCC is controlled by various parameters such as electrochemistry at the base of the pit, pit geometry, chemistry of the material and stress strain rate at the base of the pit. Figure 2.7 shows the SCC that initiates at pits that form during exposure to service environment.

(iii) Crack initiation by intergranular corrosion.

In the absence of pitting, stress corrosion crack initiation can also occur by intergranular corrosion. For crack initiation to occur by this process, the chemistry of local grain-boundary must be different from the bulk material. This condition occurs in sensitized aluminum alloys, austenitic stainless steels or with segregation of impurities such as phosphorous, sulphur or silicon in a variety of materials. In other words, intergranular corrosion leads to SCC problem whenever the material is subjected to tensile stress.

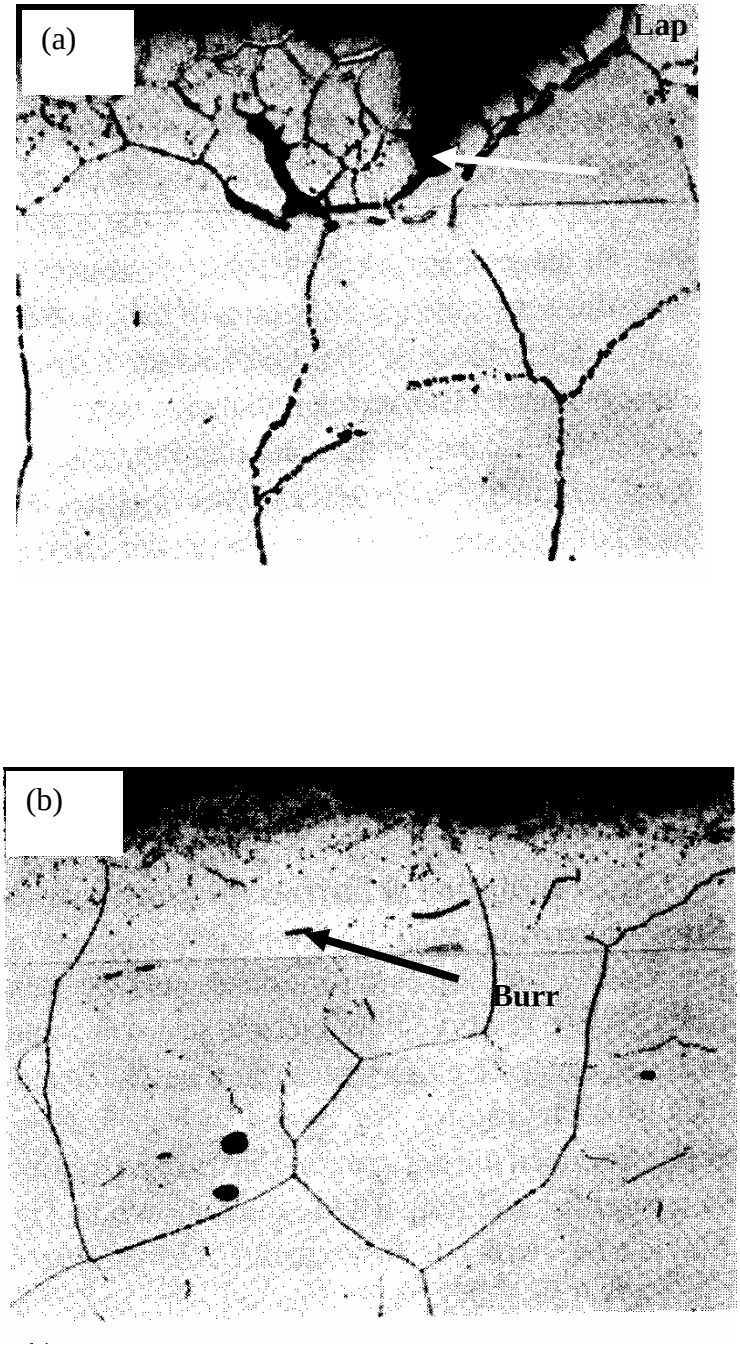

Figure 2.6. Optical micrographs showing the inner defects on the inner surface of type 304 stainless steel pipe (a) near weld root and (b) near through-crack 1000X [25].

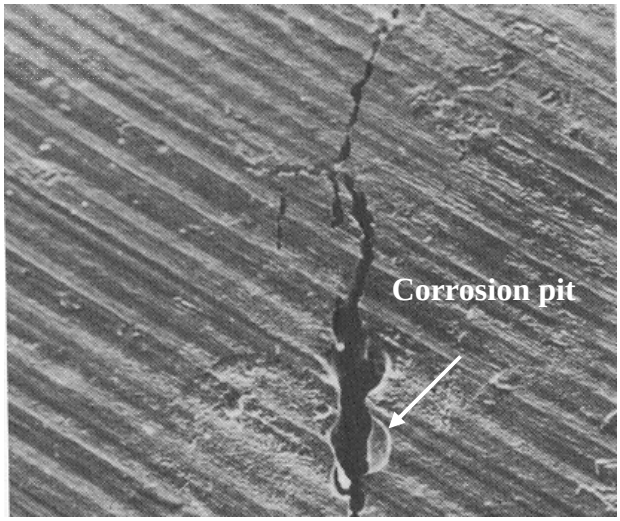

Figure 2.7. Stress corrosion crack initiation from a corrosion pit in a quenched and tempered high strength turbine disk steel (a) 275X [25].

2.6 Intergranular Corrosion and Stress Corrosion Cracking of Aluminum Alloys and Other Alloys

Intergranular corrosion (IGC) is an important issue for both general corrosion and stress corrosion cracking (SCC). It is caused by difference in the potential of grain boundary region and the adjacent grain bodies [50] and it can be defined as a preferential attack at or along the grain boundaries. The anodic region varies with different alloys system. In 2XXX series, the narrow band on either sides of the boundary that is depleted in copper is anodic to the matrix while in 5XXX series alloys, the anodic region is β-phase (Al_3Mg_2) constituent whenever it form a continuous path along a grain boundary. In copper-free 7XXX series alloys, it is generally considered to be the anodic zinc and magnesium-bearing constituents on the grain boundary but in copper bearing 7XXX series alloys, it is apparent that copper-depleted bands along the grain boundary is the

anodic region [51-52]. The 6XXX series alloys generally resist intergranular corrosion except slight intergranular cracking attack observed in aggressive environments.

The corrosion resistance of austenitic stainless steels is by and large outstanding but they are susceptible to both intergranular and transgranular stress corrosion cracking. Intergranualar cracking most often occurs in alloys that have been sensitized whereas transgranular cracking is independent of sensitization. The most important anionic agent for cracking austenitic stainless steel is the Cl^- ion and its attack constitutes the most important problem to the use of these steels. These alloys are most susceptible to hot concentrated chloride solutions and hot caustic solutions but failures have been reported in solutions with chloride contents as low as 5 part per million [53]. The resistance of carbon steel to IGC is generally decreased at temperature range of $550^oC–750^oC$ due to chromium-rich carbides (Cr_xC_y) that precipitates along the grain boundaries. The formation of chromium-rich carbides produces a chromium-depleted region closest to the carbide precipitates and thus, this depletion leads to IGC [54]. As sensitization increases, the IGC attack increases to the point where the sample ruptures with minimal resistance. Non-sensitized stainless steels experience stress corrosion cracking that takes the form of multibranched, transgranular cracking in solutions containing chlorides. Intergranular also occurs in systems that handle hydrogen sulfide. The cause can be traced to the formation of polythionic acids (H_2S_x, where x = 3,4,5) formed by the chemical reaction of residual metallic sulfides on oil-refinery equipment with moist air at room temperature. Sensitized stainless steels are vulnerable to polythionic acid attack

[55-56]. Duplex stainless steels demonstrate better resistance to sensitization and IGC compared with austenitic grades of similar carbon content [57].

Copper alloys with minor amount of phosphorous, zinc, antimony, nickel, silicon, and aluminum are susceptible to intergranular stress corrosion cracking (IGSCC) in ammonia and ammoniacal solutions. Both intergranular cracking and transgranular cracking are observed in these alloys depending on the pH of the solution. Transgranular cracking frequently occurs under more acidic (pH < 4) and more alkaline (pH > 8) conditions. Ammoniacal SCC of brasses shows intergranular cracking and a minimum time to failure at a pH of 7 [48]. The requirement of oxygen and water for intergranular stress corrosion cracking (IGSCC) is confirmed by the observation that anhydrous ammonia does not cause SCC of copper or any of its alloys [58]. Nitrogenous compounds, such as nitrates, amines, and oxides of nitrogen, as well as sulphate, sulphur dioxide, and steam, have caused similar failures.

The susceptibility of plain carbon and low–alloy steels are controlled by carbon content and strength level, respectively. Carbon steels with carbon contents lower than 0.10wt% appear to be the most susceptible. The behaviour of high-strength low-alloy steels is more a function of strength than alloy dependent. Steels with yield strengths of about 1379 MPa or higher are susceptible to this type of failure.

Titanium and many of its alloys are susceptible to SCC in certain environments such as distilled water, sea water, chlorinated solvents, red fuming nitric acid, and molten salts.

Brient [54] reported that the two environments that have received the greatest attention are aqueous solutions of NaCl at both neutral and acidic pH values and organic liquids such as carbon tetrachloride and methanol. Titanium of various purity levels along with the α alloys will corrode intergranularly if left unstressed in a methanol/halogen solution. The principal difference between cracking in methanol/halogen solutions and that in aqueous NaCl solutions arises from the fact that titanium will dissolve in methanol to produce methoxide, which results in corrosion when stress or halogens are present to break down the passive film. The mode of intergranular or transgranular corrosion depends on the slip mode and stress level. Alloys containing β phase usually do not corrode in the unstressed condition but do so readily when stressed. Generally, α and α+β alloys are susceptible while β and pure titanium are not. A critical concentration of tin or aluminum is usually required before significant SCC is observed. Also, precipitation of Ti_3Al phase and an increase in grain size promote susceptibility to SCC.

Cold worked aluminum alloys containing Mg ≥ 5 wt% can form continuous grain boundary films of β- phase when stored in room temperature for long period, and the intergranular corrosion and the resistance to stress corrosion cracking would be damaged seriously [59-60]. Thus, the annealing, cold work and precipitation treatment process is widely used for high concentrated Al-Mg alloys to remove the continuous intergranular networks and improve the distribution of β- phases and SCC and exfoliative corrosion [60-61]. Lin Zhaoqi *et al*. [62] studied the effect of intergranular segregation of Mg on the exfoliative corrosion in Al-Mg alloys containig 7wt%, 5wt%

and 3wt% Mg using energy dispersive X-ray spectroscopy (EDS), scanning transmission electron microscopy (STEM) and ASTM 11 immersion test. Their results show that Mg segregation to the grain boundaries in the specimens containing 3wt% Mg is not influenced by cooling rate (CR) and precipitation temperature (T_p) and the specimens show the highest exfoliative corrosion stability. Otherwise, Mg segregated at the grain boundaries of alloys containing 5 and 7wt% which is obviously influenced by CR and T_p. They have enough exfoliative corrosion stabilities only when both CR is lowered to critical temperature and T_p is raised to a critical temperature which leads to Mg segregation reduction at the grain boundaries and thus, the continuous grain boundary film of β-phase disappear.

As the Mg content of Al-mg alloys increases exceeding the limit of solubility at room temperature, the alloy becomes unstable with time at moderately service temperatures (as low as 70^{o}C) [63]. The unstableness appears in Al-Mg alloys as precipitation or Mg enrichment at the susceptibility to exfoliation, stress corrosion cracking or intergranualar corrosion attack. Magnesium surface enrichment can lead to detrimental effects on fabrication and performance of the alloyed. It can encourage ecological sensitivity of the alloy through its enrichment in the surface oxide above grain boundary sites, which encourage localized reactivity and hydrogen entry [64]. Flores *et al.* [65] studied the influence of Mg enrichment in the corrosion behaviour of AA5083 alloy in both as-received and sensitized (at 100^{o}C and 200^{o}C) conditions using Auger electron spectroscopy (AES). The specimens were immersed in 60% nitric acid for three days (72 h). It was reported that there was an increase in the amount of MgO on the alloy

surface as temperature increased. Aluminum oxide transformed to magnesium oxide layer which affected the open circuit behavior of the alloy when immersed in hot alkaline solution. Crystallographic characteristics of the grain boundaries and the presence of aggressive species from the electrolyte such as Cl^- influence the extent of intergranular attack.

Several researchers that studied SCC of AA5083 have found magnesium to segregate to both grain boundaries and free surfaces of aluminum [3,11,16-17,19,66-68]. Their results show different enrichment ratios for magnesium at both triple point and along the grain boundary for various temperature treatments. Although the presence of the β phase (Al_3Mg_2) has generally been accepted as the primary cause of SCC of Al-Mg alloys, this phase does not precipitate uniformly along the grain boundaries. It occurs along with the segregation of magnesium at grain boundaries. It was found that SCC occurs for conditions where relatively small concentration of the β phase is present [19,68].

The authors in reference [11] examined the role of elemental Mg segregation in intergranular stress corrosion cracking (IGSCC) of AA5083 with the aid of AES and analytical electron microscopy (AEM). They also quantified the relationship between crack-growth rate and volume fraction of the β phase along grain boundaries in AA5083 with aid of AEM and scanning electron microscopy (SEM) for the same thermal treatment periods. Samples used were aged at 175^oC for various lengths of time to induce precipitation of the β phase. Their results showed that the presence of elemental Mg in the grain boundaries does not affect IGSCC and that crack growth rate increases with anodic polarization relative to the open circuit potential (OCP) but not cathodic

polarization. It was suggested that the β phase could be a catalyst for crack-growth through anodic dissolution. It was also shown that the β phase corrosion rate is 10^{-2} A/cm^2 when polarized to the open-circuit potential of AA5083 in a solution of 3.5% NaCl. Figure 2.8 shows transmission electron microscope micrographs of AA5083 with different heat treatments.

Baer *et al*. [8] studied the influence of magnesium on the corrosion and electrochemical behaviour of aluminum. The corrosion potential and film formation of pure aluminum, aluminum implanted with magnesium, Al-7 wt% Mg alloy and pure Al_3Mg_2 phase were compared based on the measured open circuit potentials. From their results they suggested that segregated magnesium plays little role in the cracking and that hydrogen production at the β phase particles might be the most significant factor.

Searles *et al.* [16] performed constant extension rate testing (CERT) on sensitized AA5083 samples under open-circuit conditions and under potential control. In this study, three experimental techniques namely CERT, transmission electron microscopy (TEM) and SEM fractography were used. TEM was used to assess the degree of β precipitation on grain boundaries as a function of sensitization time and to analyse the composition of precipitates. Bright and dark field images were taken to illustrate the phase distribution and diffraction analysis was used for phase identification. Also, STEM was used together with the EMISPEC^{TM} software program for elemental mapping in the vicinity of the grain boundaries to identify precipitates and assess the depletion or segregation of magnesium. Both CERT and TEM evaluation support the

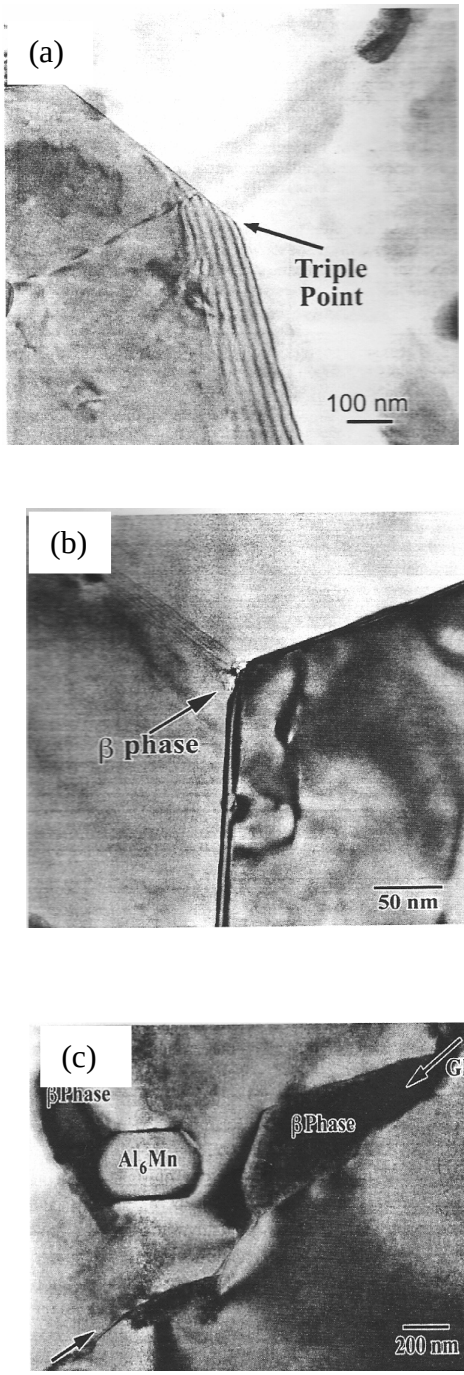

Figure 2.8. TEM micrographs for alloy AA5083 with the following treatment (a) solution treatment and quenched (b) solution treatment, quenched and aged for 1h at 175^{o}C (c) solution treatment, quenched and aged for 100h at 175^{o}C [11].

classical anodic dissolution mechanism originally proposed by the author in reference [8] to explain SCC in these alloys. Their results support earlier work [24] that also showed no variation in the mechanical properties of 5XXX alloys in air as a function of sensitization time. Searles *et al.* concluded that the contributions of hydrogen and anodic dissolution to IGSCC are difficult to separate since significant hydrogen production rates can only exist when the local or overall dissolution rate is high.

The role of hydrogen in the IGSCC behaviour of Al-Mg alloys was reported [18,69] based on the results of tests conducted with notched and fatigue pre-cracked compact tension specimens under constant Mode I (tension) and Mode III (torsion) load conditions. The difference in cracking behaviour was attributed to the triaxial state of stress present at the crack tip in tension, which allowed more hydrogen to penetrate the process zone in Mode I loading. Other work [27] suggested that free magnesium observed on the grain boundaries between β particles aids in the absorption of hydrogen in those regions. Hydrogen permeation studies supported the hypothesis in which pure aluminum and other magnesium-free alloys exhibit a low permeability compared to alloys in which magnesium segregation has occurred [70].

Decomposition of solid solution of AA5083 alloy was studied by Sampath *et al.* [7]. The samples were produced from a 6mm gauge alloy plate. Microstructures representing different stages of decomposition were produced from combinations of temperatures in the range of 50-225^{o}C and exposure times up to two weeks. The microstructures of heat treated sample were then examined using optical microscopy. The weight loss

experiment was conducted according to the ASTM G 67. Their results show that magnesium decomposition in the material is a complex microstructural reaction followed by a steady precipitation of magnesium intermetallics within the grain interiors for all the samples exposed to 50 h at the stated temperature range.

Jones *et al.* [11] used U-bend tests to study stress corrosion behaviour of alloy AA5083. The U-bend test results are given in Table 2.5. From the results, it is apparent that increasing sensitization time at 175^{o}C resulted in shorter failure times and increasing failure frequencies. The susceptibility of superplastic and non-superplastic AA5083 alloys to intergranular corrosion was studied by Chang *et al.* [71] using nitric acid mass loss test (NAMLT) (i.e. ASTM G 67). Their results show that the corrosion resistance of superplastically formed specimen was the worst among the entire specimens. The formation of cavities during the superplastic forming and sensitization effects were reported as the cause for the reduction in resistance to SCC. Table 2.6 shows the results of the NAMLT test for AA5083. According to these results, both the as-received and the post-annealled specimens were not prone to SCC since the measured weight loss in each case was less than 15 mg/cm^2.

Table 2.5. Results of U-bend test for AA5083 immersed in 3.5% NaCl [11].

	Number of cracked samples (Three of each)		
Heat Treatment	815 h	983 h	1319 h
1 h at 175°C	-	-	-
10 h at 175°C	-	-	-
24 h at 175°C	-	-	-
50 h at 175°C	-	1	1
100 h at 175°C	3	3	3

Table 2.6. Results of NAML test for AA5083 [61].

Specimen	Weight loss (mg/cm^2)
As-received (superplastic)	5.6 ± 0.4
Superplastically formed at 500°C	41.6 ± 4.5
Heat treated (superplastic) at 500°C	43.8 ± 3.7
Post-annealing after superplastic forming	4.7 ± 0.5
Post-annealing of heat treated (superplastic)	5.9 ± 0.3
As-received (non-superplastic)	3.2 ± 0.3
Heat treated (non-superplastic) at 500°C	38.3 ± 4.1
Post-annealing of heat treated (non-superplastic)	3.4 ± 0.3

3. MATERIALS AND EXPERIMENTAL METHODS

The experiments performed in this work were designed for two purposes. The first was to understand the effect of sensitization on the mechanical properties, hardness and microstructure of AA5083-H116. The second objective was to investigate the effect of sensitization on the intergranular corrosion resistance of the as-received and sensitized specimens at various temperatures for up to 672 h (4 weeks). In addition, a four-point bending test apparatus was designed to study the stress corrosion cracking behaviour of the alloy.

3.1 Materials

The material used in this study was AA5083-H116 and it was supplied in the form of a 9.61 mm (3/8") and 6.00 mm-thick extruded plates by Alcan Aluminum Limited, Kingston, Ontario. Table 3.1 shows the chemical composition supplied by the manufacturers.

Table 3.1 Chemical compositions of AA5083-H116 (Alcan).

Element	Cu	Fe	Mg	Mn	Si	Ti	V	Zr	Cr	Al
Wt %	0.027	0.317	4.258	0.547	0.087	0.005	0.009	0.009	0.074	Rest

3.2 Experimental Methods

3.2.1 Inductively Coupled Plasma/Mass Spectroscopy (ICP/MS)

Inductively coupled plasma/mass spectroscopy was performed to determine the chemical composition of the specimens tested. To carry out the ICP/MS test, 20 mg of powdered specimens were scraped from a rectangular piece of AA5083-H116, weighed in an analytical balance, and poured into a Teflon screw-capped jar (Savillex ^{R}). One ml of 3.2 N ultra pure hydrochloric and 0.5 ml of 8 N ultra pure nitric acids were added to the jar and tightly capped. The jar was heated on a hot plate at a temperature that ranged from 100 to 150^{o}C until the entire material was dissolved. After rinsing the jar with distilled water, the solution was transferred into a sample bottle. Additional water was added to the sample bottle to bring the final weight to 100g. A Perkim Elmer Elan 5000 inductively coupled plasma/mass spectroscopy (ICP/MS) was used to analyze the solution. Following the protocol of internal standardization, 100 parts per billion (ppb) Be, 50 ppb In, Tb, and Bi were added to the solution to forestall instrumental drift and matrix effect. The high thermal energy and electron-rich environment of the ICP converted the atoms into ions. The ions and each mass were detected by quadruple mass spectroscopy and thus allowing signals of individual isotopes of an element to be scanned.

3.2.2 Hardness Measurements

The specimens for hardness measurements were cut from the AA5083-H116 stock plate and sensitized in an air furnace at various temperatures (100^{o}C, 150^{o}C, 175^{o}C and 200^{o}C) for various lengths of time up to 672h. The specimens were metallurgically polished to 0.1 µm. Hardness measurements were carried out using a Buehler Micromet II Vickers Microhardness Tester with a load of 200g applied for 15s. The Vickers Hardness Number (VHN) was computed from the average length of the diagonals measured using the focal scale on the microscope of the Vickers hardness tester. For each specimen, at least twelve microhardness measurements were taken to ensure representative result.

3.2.3 Tensile Testing

Rectangular tensile specimens were prepared in accordance with ASTM B 557M-02a standard [72] from the 9.61 mm-thick AA5083 plate. They were cut in such a way that the gauge length was along the rolling direction of the plate. Figure 3.1 shows the exact size of the tensile test specimens, with a gauge length of 25 mm. The tensile specimens were sensitized at the same temperatures as the hardness samples and subsequently fractured in an Instron® Model 1137 tensile machine with cross head and chart speeds of 5 mm/min and 50 mm/min, respectively. Figure 3.2 shows the Instron® machine with the specimen on the holder. An initial strain rate of 0.0033s^{-1} was used. The formula used for calculating the initial strain rate is given in equation (3.1). The tensile strength and percent elongation data reported represent the average of three tests.

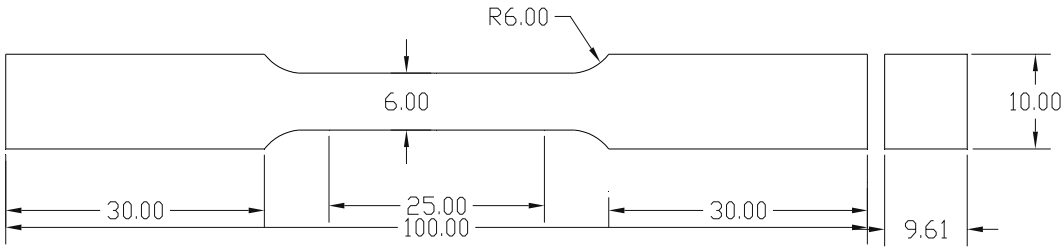

Figure 3.1. Dimensions of tensile specimens used. All dimensions in mm.

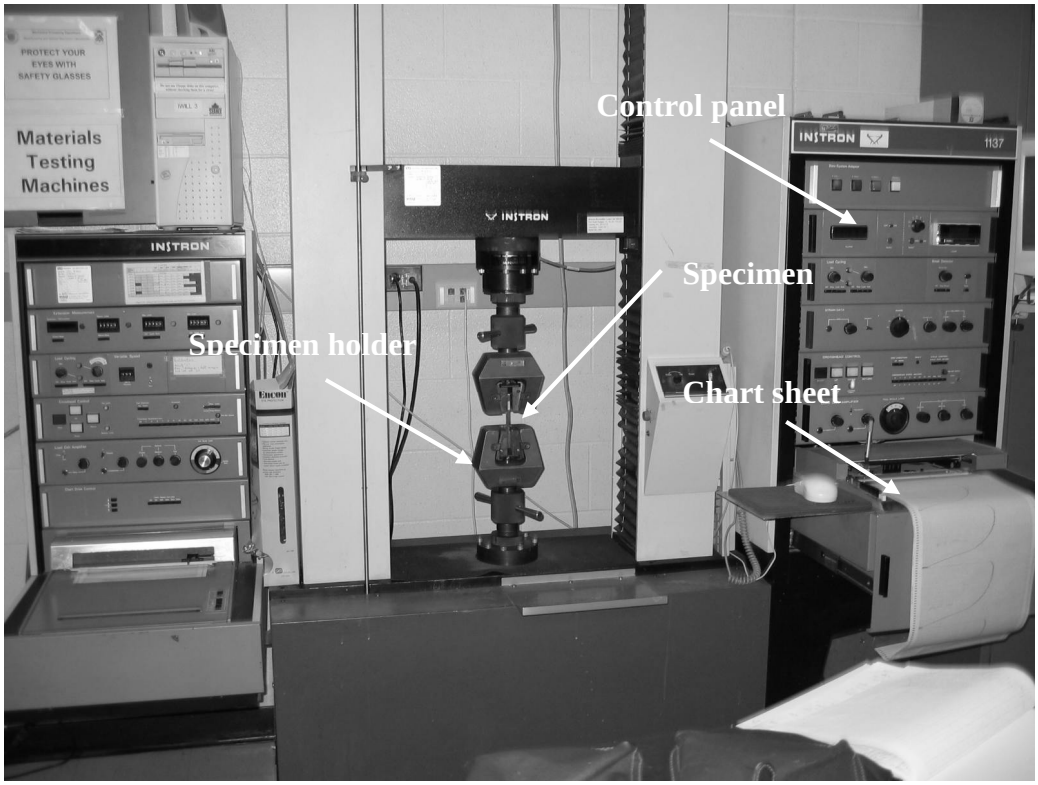

Figure 3.2. Photograph of Instron™ machine and specimen.

$$\text{Initial Strain Rate} = \frac{\text{cross head speed (mm/min)}}{\text{gauge length (mm/min)}} \tag{3.1}$$

3.2.4 Nitric Acid Mass Loss Test (NAMLT)

The susceptibility of AA5083-H116 alloy to IGC was determined using the Nitric Acid Mass Loss Test (NAMLT) as prescribed in the ASTM G-67 standards [73]. Figure 3.3 shows a typical specimen used for this test. The specimens were cut along the rolling direction and polished with a 320-grit emery paper and cleaned with methanol. Sensitization of the specimens was carried out in an air furnace at 80^{o}C, 100^{o}C, 150^{o}C, 175^{o}C and 200^{o}C for various lengths of time up to 672h. After sensitization, the specimens were etched in a 5 wt.% sodium hydroxide (NaOH) solution at 80^{o}C for 60s**,** de-smut in a 70vol.% nitric acid (HNO_3) for 30s, rinsed with de-ionized water and dried in air. They were subsequently weighed to an accuracy of ±0.1mg. The NAMLT was conducted by completely immersing each specimen into 70vol.% HNO_3 in a beaker at 30±1^{o}C for 24h. The corrosion products were removed from the specimens according to the ASTM G-1 standards [74]. The specimens were cleaned with de-ionized water and methanol and dried before the final weighing. The difference between the initial and final weights gave the mass loss due to acid attack. The NAMLT results presented in this study are the average of three samples.

3.2.5 Design and Construction of Four-Point Bending Test Apparatus

The four-point bending test apparatus for studying the SCC of AA5083-H116 (see Figure 3.4) was constructed from 1018 steel and coated with electroless nickel (0.002" thick) to prevent corrosion damage to its various components. It was designed in accordance with the ASTM G-39 [75] specifications but it also contained additional

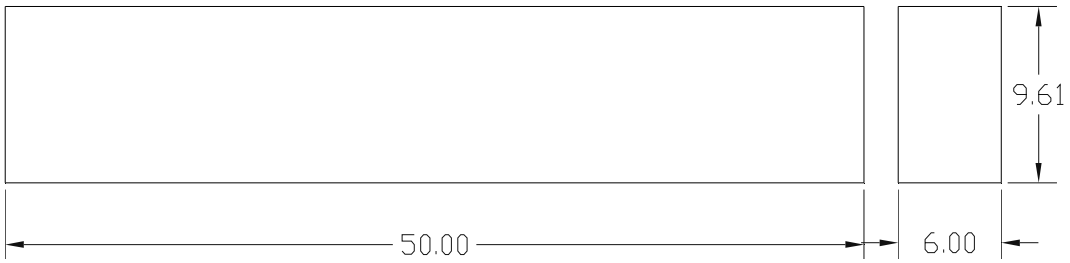

Figure 3.3. Specimen for nitric acid mass loss test. All dimensions in mm.

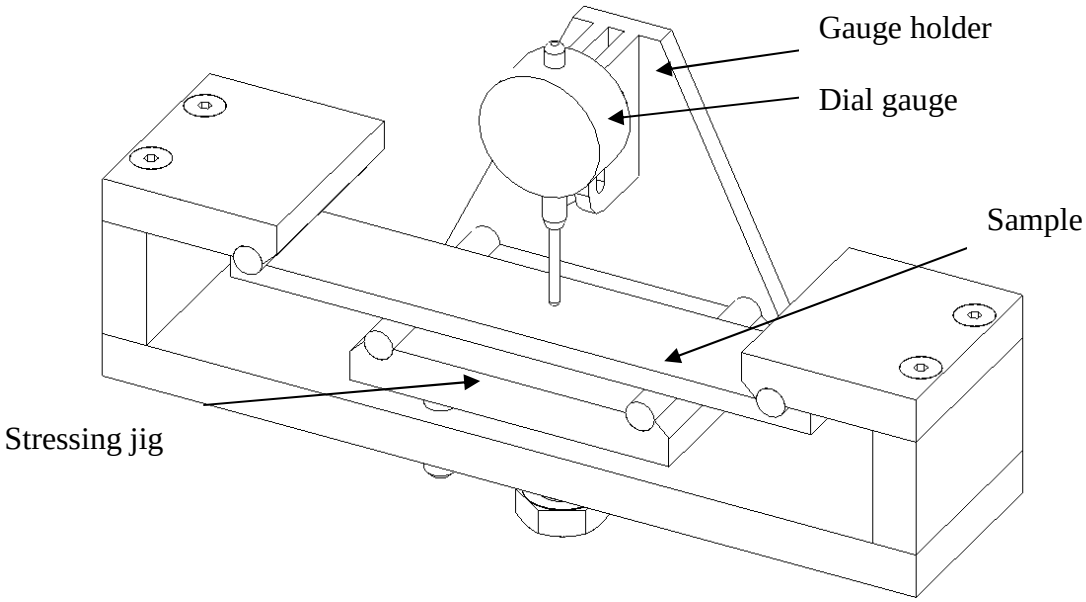

Figure 3.4. Four-point bending apparatus.

features such as the detachable dial gauge holder. The design was such that it retains the load applied on the specimen throughout the duration of the experiment.

3.2.6 Four-Point Bending Test

The susceptibility of AA5083-H116 to SCC was determined in accordance with the ASTM G-39 standards. The specimens were cut from 6mm thick sheet of the alloy such

that the original material surface was retained. The specimens were flat strips measuring 51mm wide and 254mm long. They were inscribed at each end for identification purpose and cleaned with methanol. Figure 3.5 shows a typical bending test specimen. The edges of the specimens were polished with 240 grit emery paper to remove sharp edges. They were subsequently sensitized in an air furnace at 100^{o}C, 150^{o}C, 175^{o}C and200^{o}C for various lengths of time up to 672h. Specimens were mounted on the four-point bending test apparatus, stressed with a stressing jig and immersed completely into a 3.5wt % sodium chloride solution and maintained at room temperature of 20 ± 2^{o}C.

The applied stress (σ) was determined from equation 3.2 [75].

$$\sigma = \frac{12Ety}{(3H^2 - 4A^2)} \tag{3.2}$$

where σ is the maximum tensile stress, E is the modulus of elasticity, t is the thickness of the specimen, y is the maximum deflection (between outer supports), and H is the distance between inner and outer supports.

The pH of the solution was maintained at 7.0 throughout the duration of the experiment by periodically adding appropriate quantity of NaOH or HCl based on the daily pH readings. To forestall the inhibition or promotion of corrosion by corrosion products, the solution was changed completely on a weekly basis until cracks were observed with the aid of magnifying glass on the surface of the specimens. Figure 3.6 shows the entire experimental setup.

Figure 3.5. Bending test specimen. All dimensions in mm.

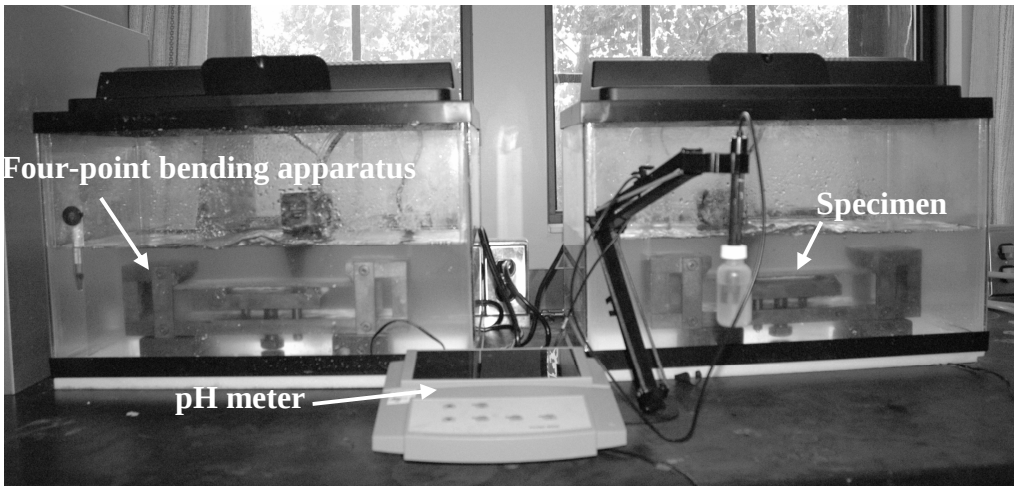

Figure 3.6. Experimental setup for the four-point test.

3.2.7 Metallography

To observe the general microstructure of both as-received and sensitized samples via an optical microscope was used. The specimens used for metallography studies were cut from the as-received plate and sensitized in an air furnace at various temperatures (100^{o}C, 150^{o}C, 175^{o}C and 200^{o}C) for different length of time. Subsequently, they were metallurgically polished to 0.1µm, cleaned with methanol and dried in air. They were then etched with a solution containing 10 vol.% H_3PO_4 and 90 vol.% distilled water

heated to 60^{o}C. The specimens were immersed inside the solution for five minutes. This etchant is used in standard metallographic practice to reveal magnesium rich intermetallic particles (β phase). Subsequently, they were dried and kept in a container with desiccant to prevent oxidation and other damages such as scratching of the surfaces prior to surface studies using optical microscopy.

3.2.8 Scanning Electron Microscopy and Energy Dispersive X-ray Spectroscopy.

For quantitative and semi-quantitative analyses using electron microscopy, rectangular specimens of as-received and sensitized AA5083-H116 were metallurgically polished using emery papers ranging from 240 to 600 grit, cleaned with methanol and dried in air. The specimens were further polished using 1 µm diamond paste and micropolishing cloth to obtain a high degree of smoothness. The distribution and chemical composition of the various intermetallic phases present in the test specimens were studied using a JEOL Model 5600 Scanning Electron Microscope (SEM) equipped with an EDAX Genesis 7000 Energy Dispersive X-ray Spectrometer (EDS). The fracture surfaces of the tensile specimens as well as etched specimens were studied using JEOL JSM Model 5900 LV SEM equipped with an INCA EDS. All specimens were examined at an acceleration voltage of 20 KV.

4. EXPERIMENTAL RESULTS AND DISCUSSION

This chapter will present and discuss results obtained for AA5083-H116 in this study, namely: chemical analysis, effect of sensitization on microstructure through the aid of optical microscopy, microstructural analysis using Energy Dispersive Spectroscopy (EDS) and Scanning Electron Microscopy (SEM), effect of sensitization on intergranular corrosion (IGC) susceptibility using nitric acid mass loss test, and sensitization effect on mechanical properties. The results of the four-point bending test will not be discussed as the experiment is in progress.

4.1 Chemical Analysis

The chemical composition of the as-received AA5083-H116 material was determined using inductively coupled plasma/mass spectroscopy (ICP/MS) and EDS to ensure that it conforms to published literature data. The elemental compositions obtained with the ICP/MS and EDS are given in Table 4.1 along with those supplied by the manufacturer, Alcan Aluminum Limited, Kingston, Ontario. It can be seen that the chemical analysis result obtained from the ICP/MS test is in close agreement with that supplied by the company while that of EDS is a little bit off from the other two results. The EDS analysis gives an approximate indication of the elements present and their relative proportion. Figure 4.1 shows a typical EDS spectrum of the as-received specimen.

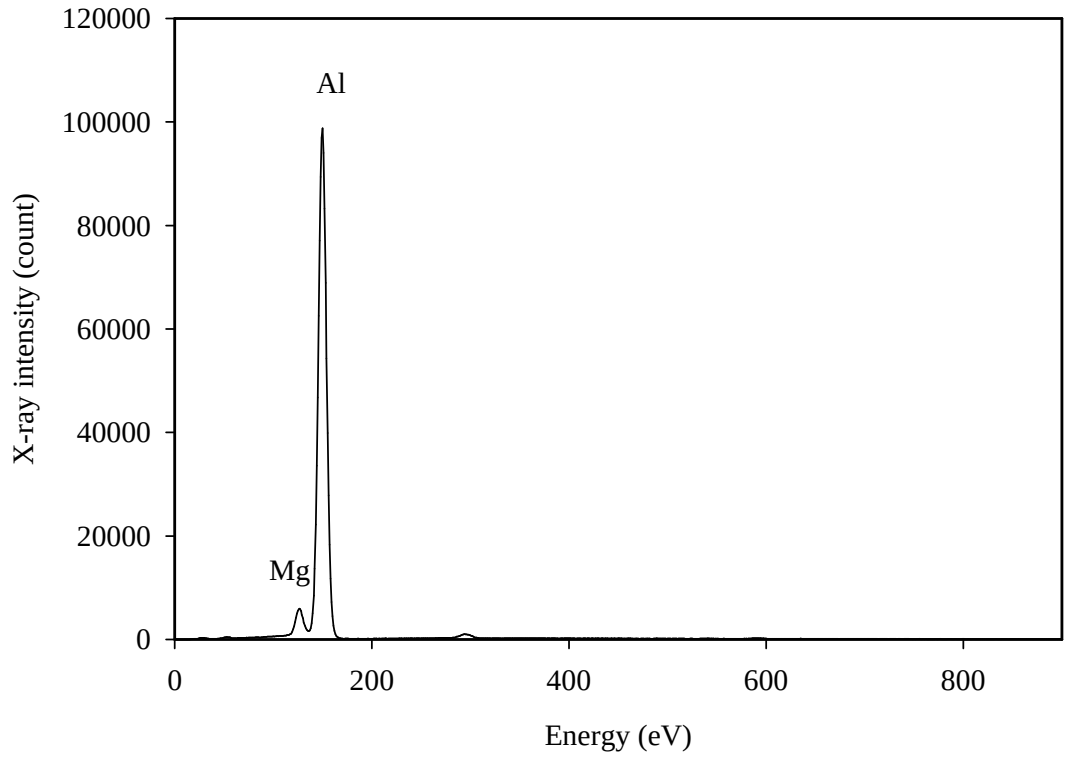

Figure 4.1. EDS spectrum of the as-received matrix.

Table 4.1.Chemical composition of AA5083-H116.

	Elements (Wt %)									
Source	Mg	Al	Si	Ti	V	Cr	Mn	Fe	Cu	Zr
ICP/MS	4.942	94.608	0.040	0.004	0.012	0.091	0.538	0.275	0.030	0.000
EDS	5.477	93.363	0.146	0.090	0.089	0.141	0.430	0.143	0.119	0.00
ALCAN	4.258	94.676	0.087	0.005	0.009	0.074	0.547	0.317	0.027	0.000

4.2 Effect of Sensitization on Microstructure

Metallographic investigations were carried out on both the as-received and sensitized specimens to have better understanding of the effect of sensitization temperature and time on the mechanical properties and susceptibility of AA5083-H116 to IGC.

4.2.1 Metallography

Figures 4.2 - 4.5 show the effect of sensitization temperature and time on the grain structure of specimens sensitized at various temperatures for different time. It can be seen that the grain boundaries are becoming much more visible as a result of the precipitate of intermetallic particles at the grain boundaries and within the matrix. It can be seen on close examination that the grain size of sensitized specimens decreased with increasing sensitization temperature and time (See Figures 4.4 and 4.5).

Figure 4.6 elaborates this observation for specimens sensitized for 672 h (4 weeks) at various temperatures. It was further revealed that the specimen sensitized at 175^{o}C (Figure 4.6 (d)) contained more particles within the matrix compared to the as-received specimen and specimens sensitized at other temperatures. It is not clear why there seems to be more of these particles in specimens sensitized at 175^{o}C than those sensitized at other temperatures. It is obvious from Figure 4.5 that the grain structure (morphology) of specimens sensitized at 200^{o}C (Figure 4.6 (e)) was appreciably different from those sensitized at lower temperatures. The difference in the grain size can be attributed to more extensive recrystallization of the specimens than in the specimens annealed at lower temperatures which resulted into significant structural changes. This is not very

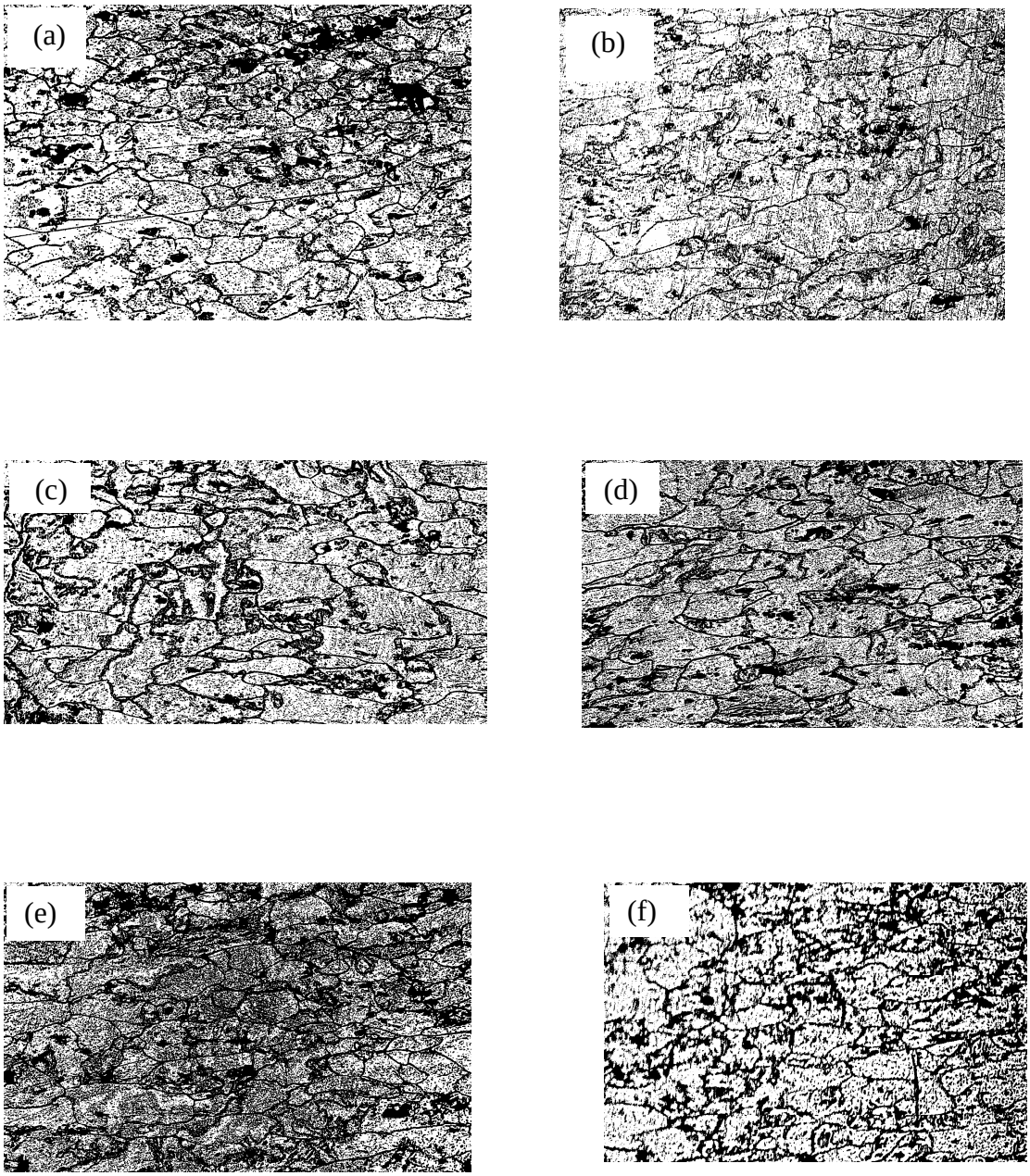

Figure 4.2. Effect of sensitization on the microstructure of (a) the as-received specimen and specimens sensitized at 100^{o}C for (b) 8h (c) 168 h (d) 336 h (e) 504 h (f) 672 h. [100 X]

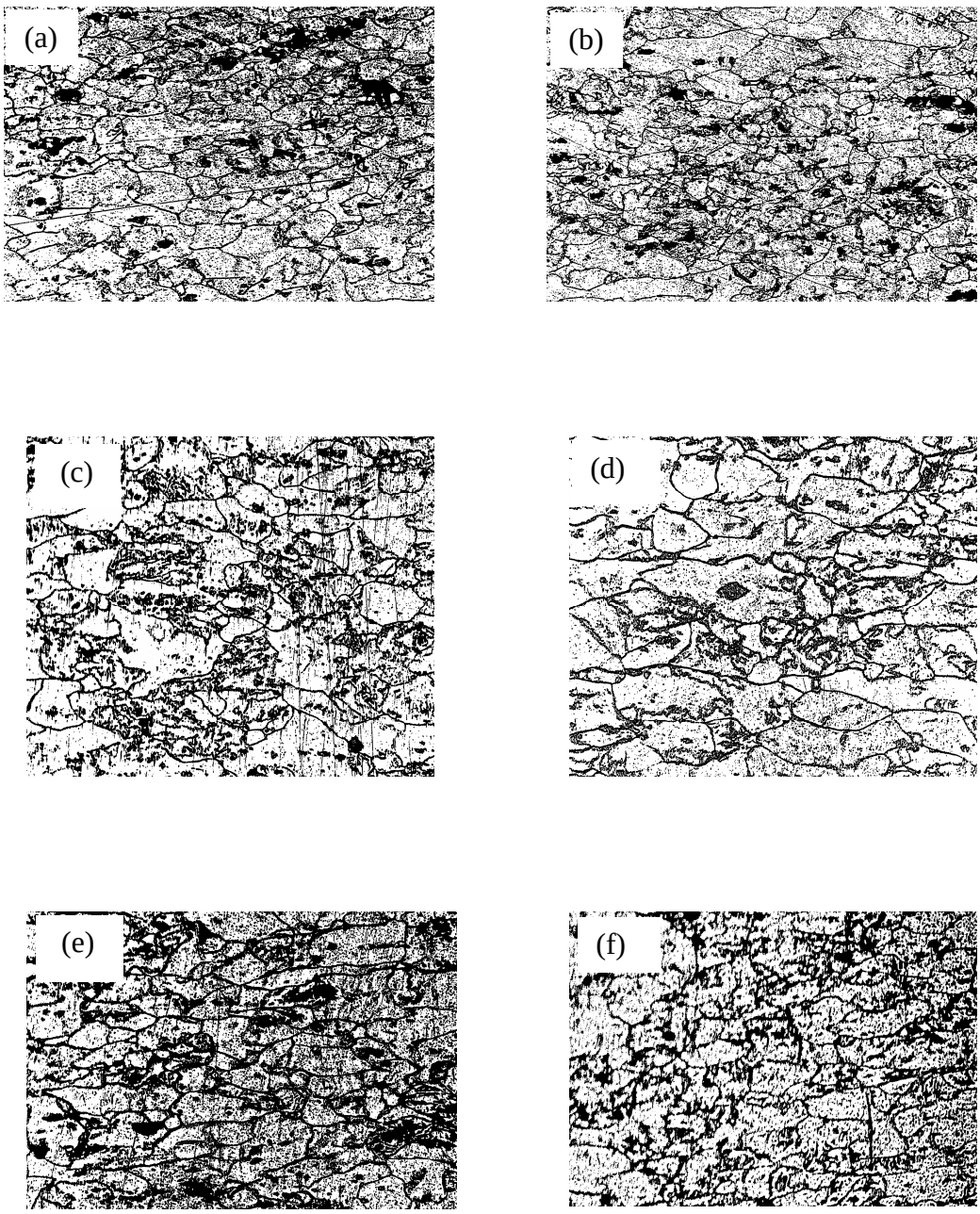

Figure 4.3. Effect of sensitization on the microstructure of (a) the as-received specimen and specimens sensitized at 150^{o}C for (b) 8h (c) 168 h (d) 336 h (e) 504 h (f) 672 h. [100 X]

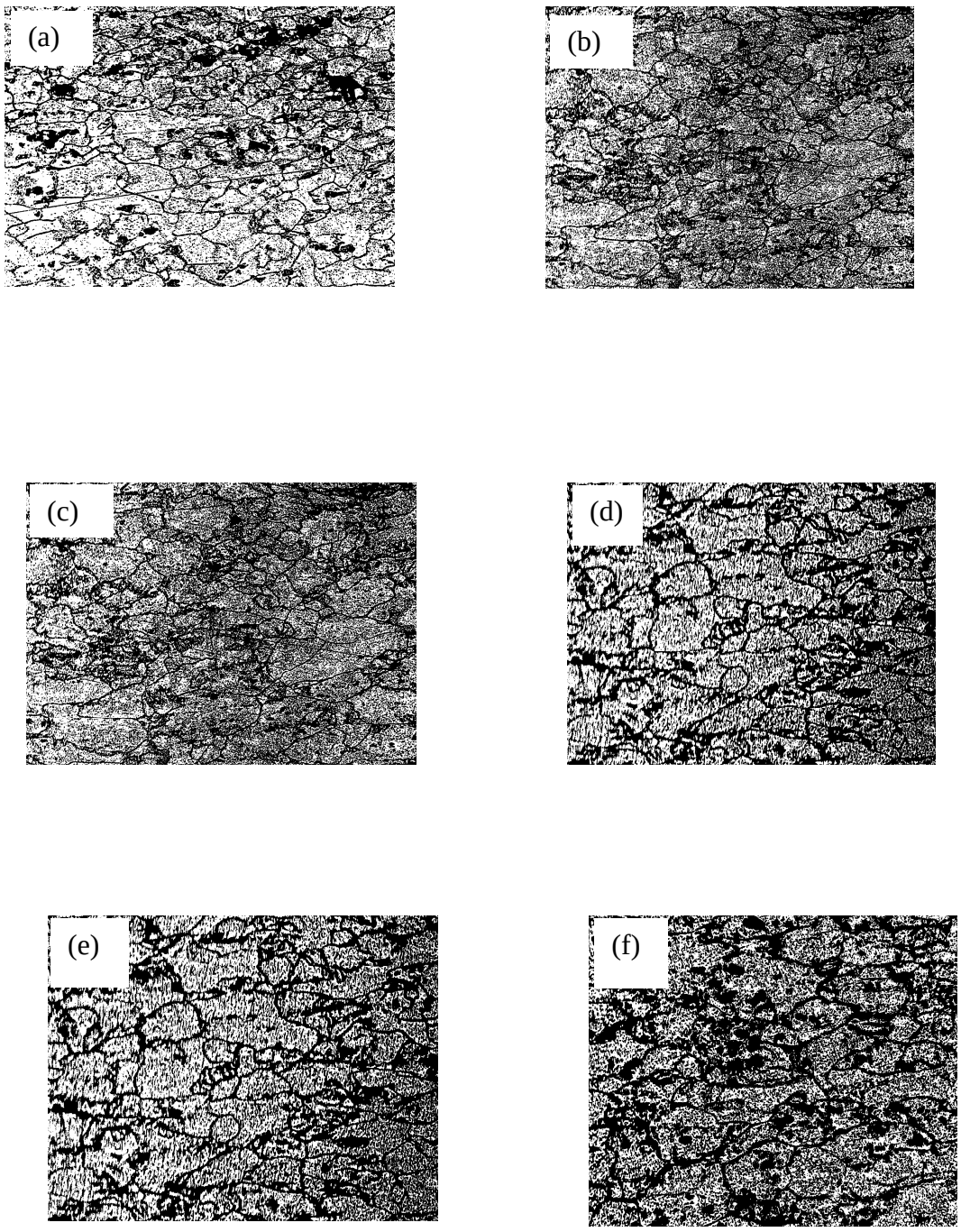

Figure 4.4. Effect of sensitization on the microstructure of (a) the as-received specimen and specimens sensitized at 175^{o}C for (b) 8h (c) 168 h (d) 336 h (e) 504 h (f) 672 h. [100 X]

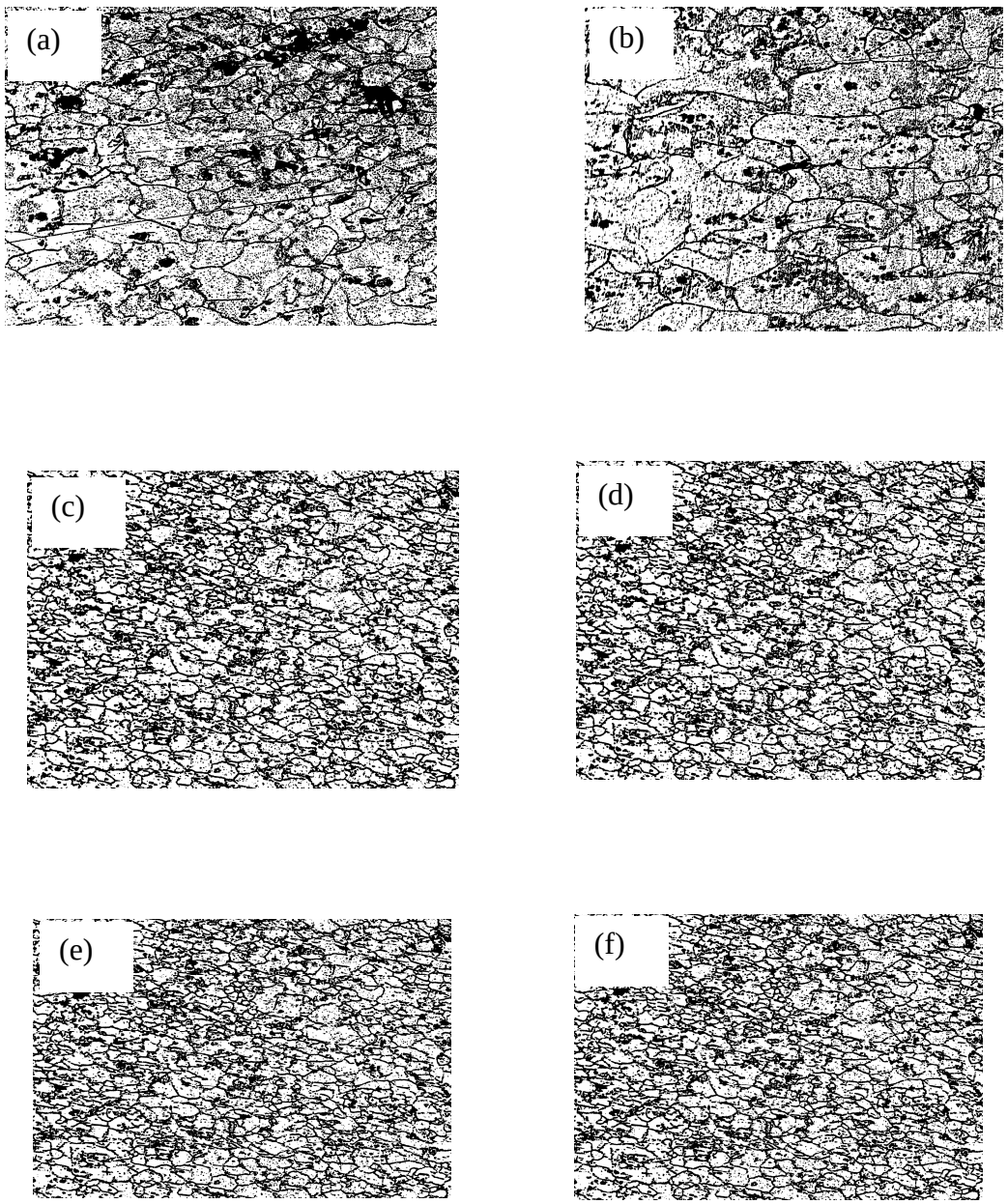

Figure 4.5. Effect of sensitization on the microstructure of (a) the as-received specimen and specimens sensitized at 200^{o}C for (b) 8h (c) 168 h (d) 336 h (e) 504 h (f) 672 h. [100 X]

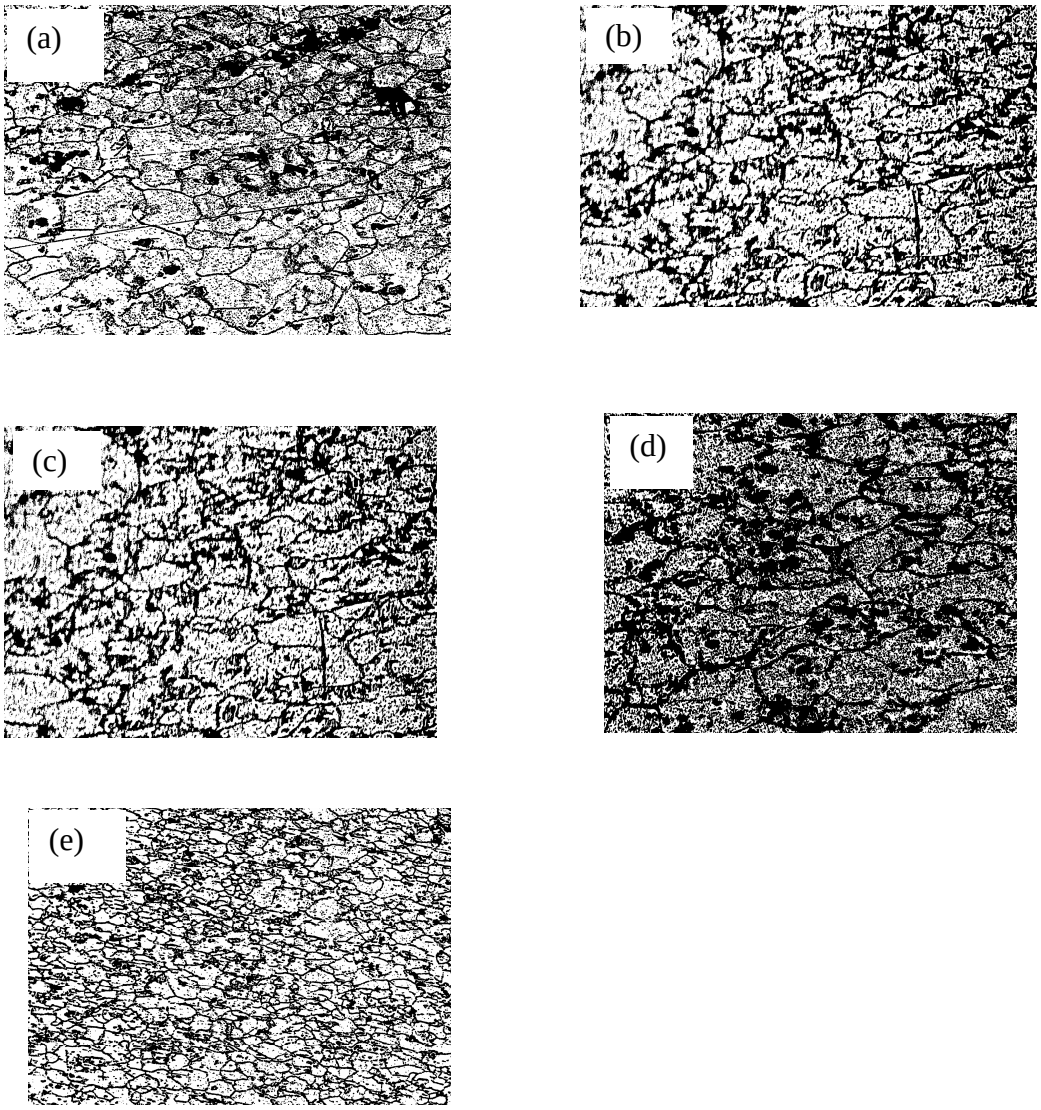

Figure 4.6. Effect of sensitization on the microstructure of (a) the as-received specimen and specimens sensitized for 672 h at various temperatures (b) 100°C, (c) 150°C, (d) 175°C and (e) 200°C. [100 X]

unusual since the extent of recrystallization in metallic alloys is a function of temperature and time. The new grains that formed as a result of sensitization are likely to have lower dislocation density compared to the rolled samples and, as a result, the mechanical properties of the newly developed structure will be inferior [76-78].

4.2.2 Microstructural Analysis

X-ray mapping of elements in the material often produces a number of images, each image representing the concentration of one element or chemical constituent. To identify the host phases in the specimens and the distribution of particles, specimens were examined in an EDAX Genesis 7000 Energy Dispersive X-ray Spectrometer. The microsructure of both the as-received and sensitized specimens revealed the presence of intermetallics particles within the structures. Figures 4.7 (a)–(d) show SEM micrographs of the as-received (upper left) and specimens sensitized at different temperature for 168h (1 week). Tables 4.2 and 4.3 show EDS point analyses of these intermetallic particles while Figures 4.8 (a) and 4.8 (b) show their EDS spectra. Tables and EDS spectra revealed the presence of Al-Fe-Mn, Mg-Si or magnesium silicate and they are identified in the micrographs as labels A and B, respectively. The occurrence of such intermetallics in Al-Mg alloys have been reported in Reference [22,25,29].

The authors in Reference [79] reported that if the content of iron, iron plus manganese or iron plus chromium is above 1-2% depending on the magnesium content, the primary phases that are likely to form are $FeAl_3$, $Al_6(FeMn)$, $Al_{15}Si_2(FeMn)_3$, $Al_7(FeCr)$ or$Al_{13}Si_4(FeCr)$. These primary crystals do not affect the strength of AA5083

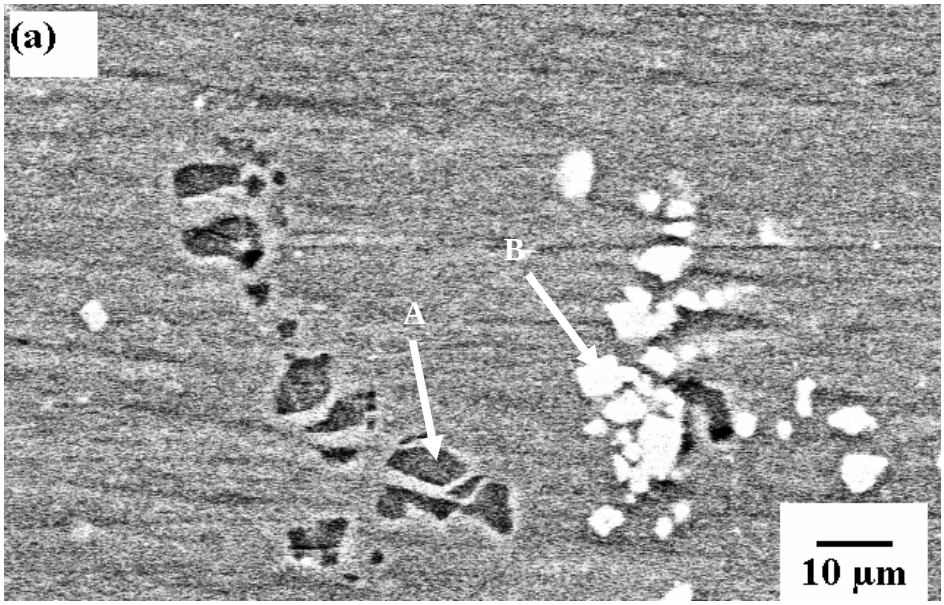

Figure 4.7 (a). SEM micrograph of the as-received specimens showing Al-Fe-Mn-rich particle (arrow A) and Mg-Si-rich particle (arrow B).

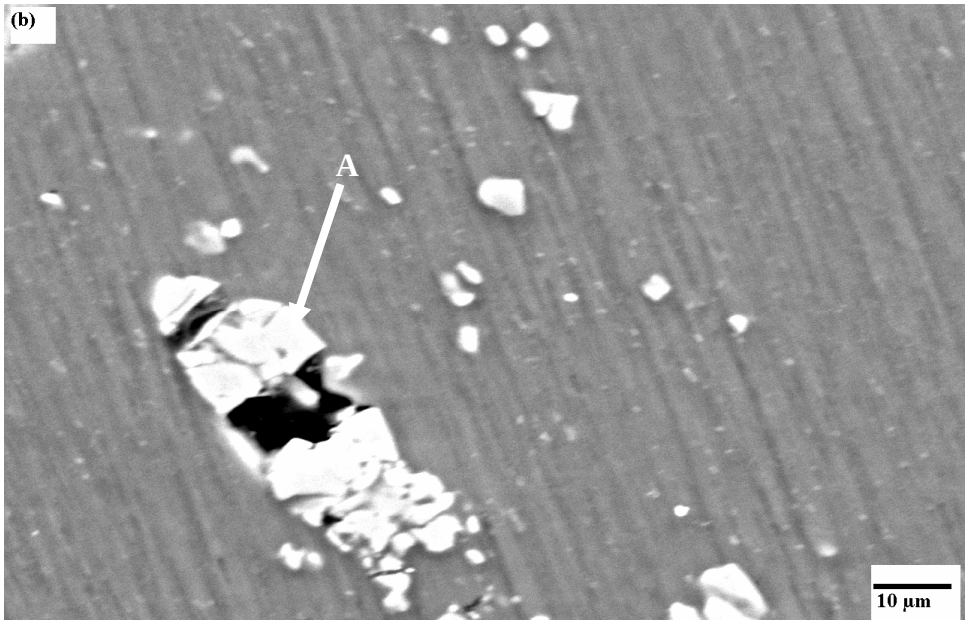

Figure 4.7 (b). SEM micrograph of specimens sensitized at 100^{o}C for 168 h showing Al-Fe-Mn particle (arrow A).

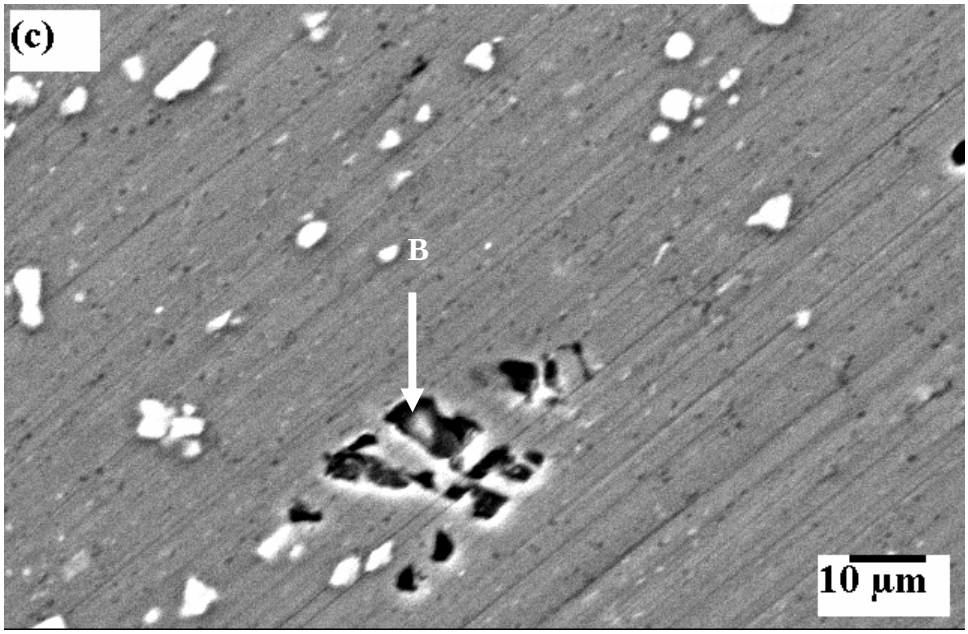

Figure 4.7 (c). SEM micrograph of specimens sensitized at 150^{o}C for 168 h showing Mg-Si-rich particle (arrow B).

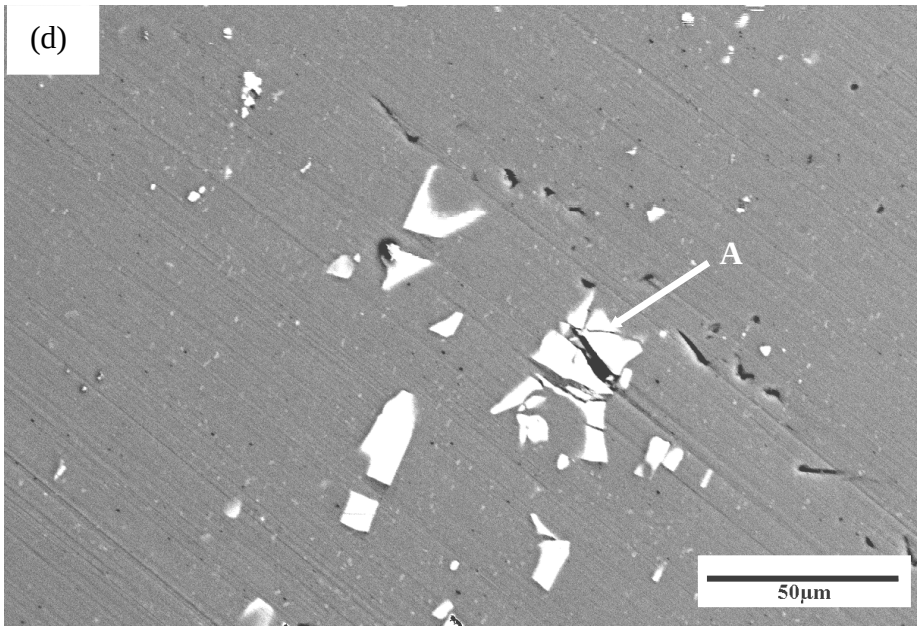

Figure 4.7 (d). SEM micrograph of specimens sensitized at 200^{o}C for 168 h showing Al-Fe-Mn-rich particle (arrow A).

Table 4.2. EDS point analysis from Al-Fe-Mn (A) intermetallic particle.

	Elements (wt %)					
Particle #	Mg	Al	Si	Mn	Fe	Likely phases
1	1.13	64.43	3.41	11.48	18.20	$Al_{23}Fe_2Mn_3$
2	2.89	79.87	0.08	6.06	11.18	$Al_{27}Fe_2Mn$
3	2.88	79.35	0.14	6.05	11.16	$Al_{27}Fe_2Mn$
4	3.28	72.00	1.49	8.56	13.55	$Al_{100}Fe_9Mn_6$
4	2.10	65.80	0.09	8.94	23.17	$Al_{61}Fe_{10}Mn_4$
5	3.70	82.77	0.12	5.82	7.71	$Al_{112}Fe_5Mn_4$

substantially but have serious effect on formability, fatigue resistance and surface finish [79]. The chemical analysis (ICP/MS), EDS point analysis and chemical composition supplied by Alcan of the as-received sample show that addition of iron and manganese or iron and chromium are less than 1%. Therefore, the likely phases in Table 4.3 and 4.4 may be different from those listed above.

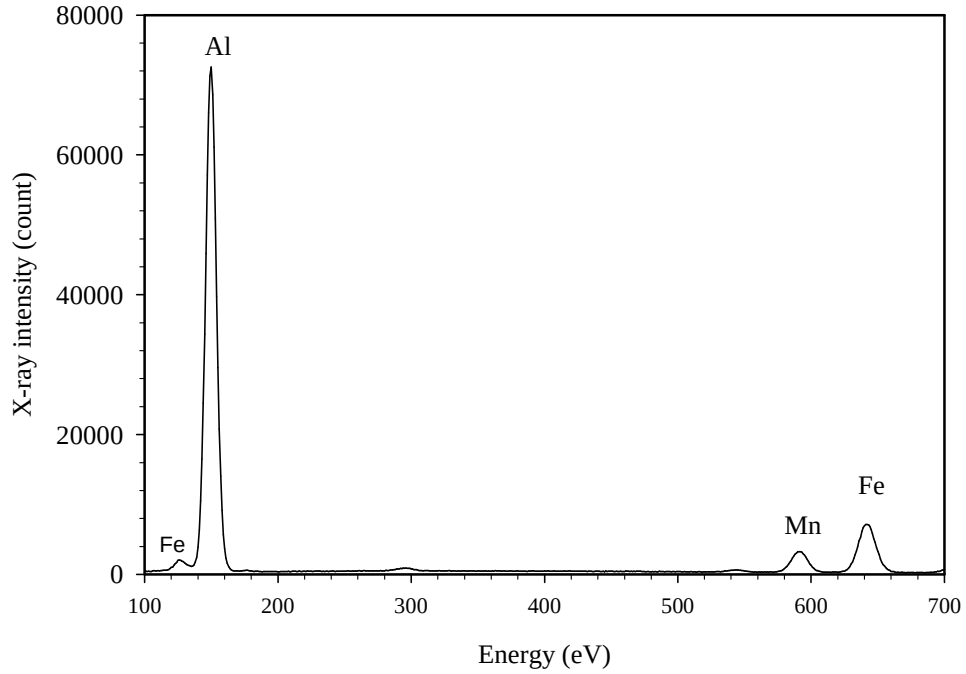

Figure 4.8 (a). EDS spectrum of Al-Fe-Mn particle (arrow A).

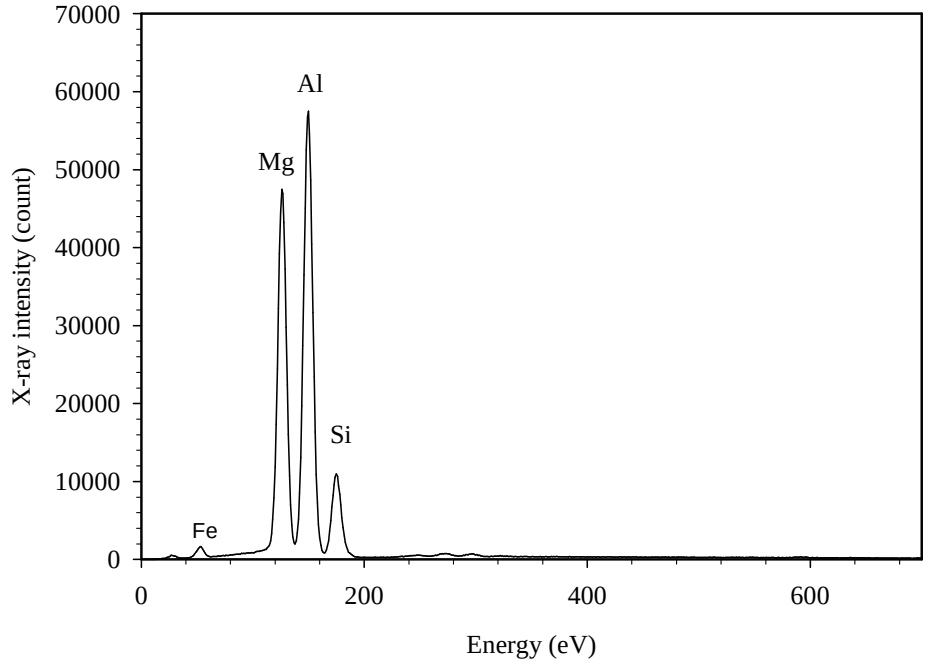

Figure 4.8 (b). EDS spectrum Al-Mg-Si particle (arrow B).

Table 4.3. EDS point analysis from Mg-Si (B) intermetallic particle.

	Elements (wt %)				
Particle #	Mg	Al	Si	O	Likely phases
1	18.86	55.37	19.17	6.60	Mg_7Si_6
2	31.01	42.87	20.43	5.69	Mg_7Si_4
3	26.91	52.41	16.94	3.73	$Mg_{13}Si_7$
5	27.32	54.55	18.13	0.00	$Mg_{17}Si_{10}$
6	17.32	55.35	18.44	8.44	Mg Si
7	12.34	65.11	13.81	8.57	Mg Si

Table 4.4. Magnesium content (wt %) in the matrix of the as-received specimen and specimen sensitized.

		100°C		150°C		175°C		200°C
Particle #	A-R	168	672	168	672	168	672	168
1	5.47	5.13	5.48	5.45	4.54	4.80	5.46	5.30
2	5.50	5.09	5.47	5.47	5.52	4.96	5.34	5.24
3	5.52	5.14	5.41	5.42	5.52	5.09	5.32	5.24
4	5.20	5.10	5.23	5.26	5.35	5.09	5.39	5.17
5	5.50	5.09	5.52	5.51	4.89	4.96	5.38	5.24
6	5.55	5.04	5.48	5.40	5.50	4.51	5.34	5.17
Average	5.46	5.10	5.43	5.42	5.22	4.90	5.37	5.23

It can be observed that the intermetallic particles have various sizes which are independent of the sensitization temperature. It can also be seen that Al-Fe-Mn particles fractured in both the as-received and specimens sensitized at 100^{o}C, 150^{o}C and 200^{o}C for 168 h, 336 h and 168 h, respectively. The fractured parts are close to each other without any evidence of any matrix cracking in between the broken parts. Thus, the particle fracture could not be attributed to specimen polishing. Also, it could not be due to sensitization treatment because fracture particles were found in almost all the specimens including as-received specimens. Therefore, the most probable source is the fabrication process. Figures 4.9 and 4.10 show SEM micrographs of the as-received specimens and their X-ray maps showing the distribution of magnesium, aluminum, silicon, manganese and iron in the alloy. Figures 4.9 and 4.10 revealed that white and

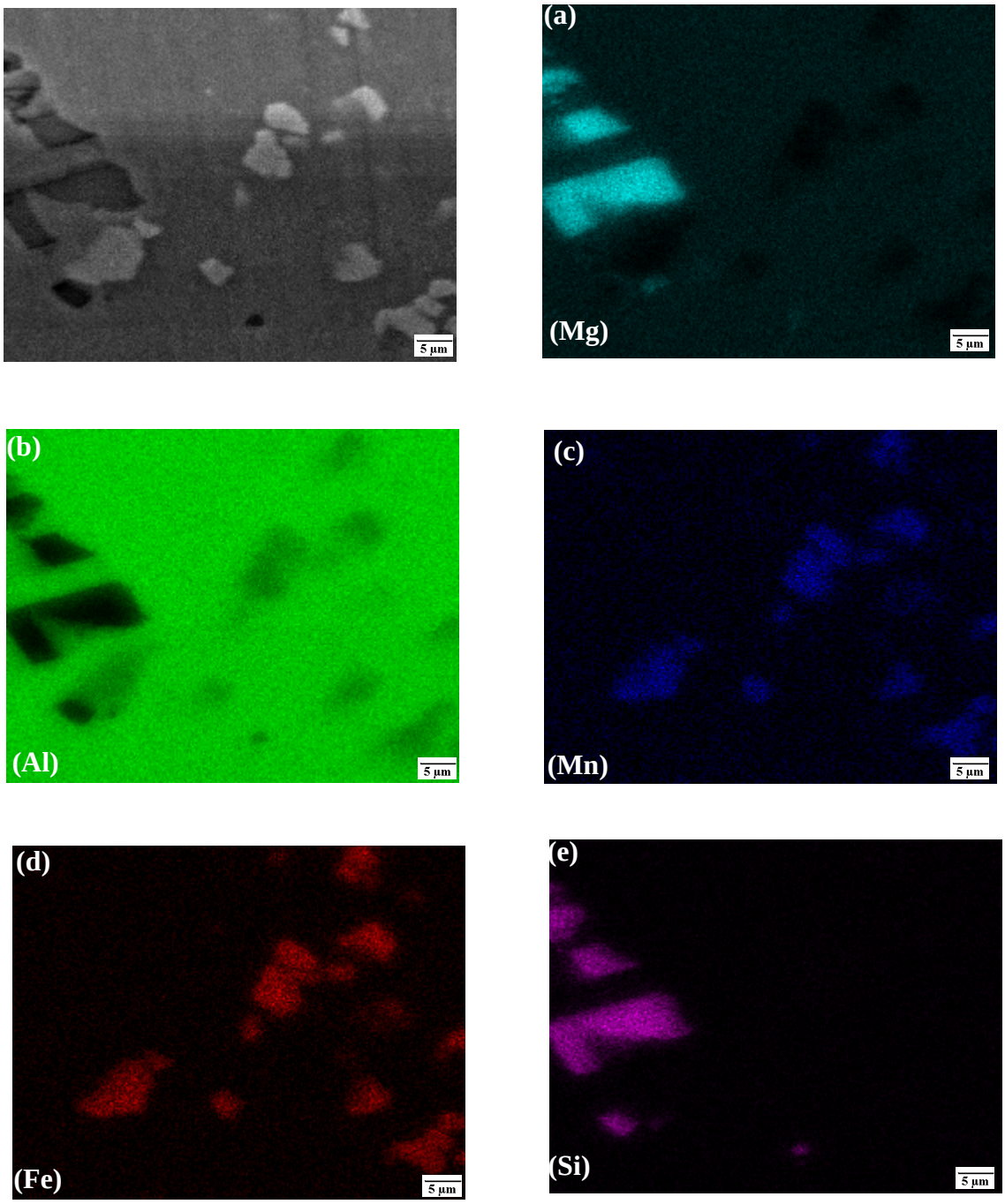

Figure 4.9. X-ray maps showing (a) Mg (b) Al (c) Mn (d) Fe (e) Si in as-received specimens.

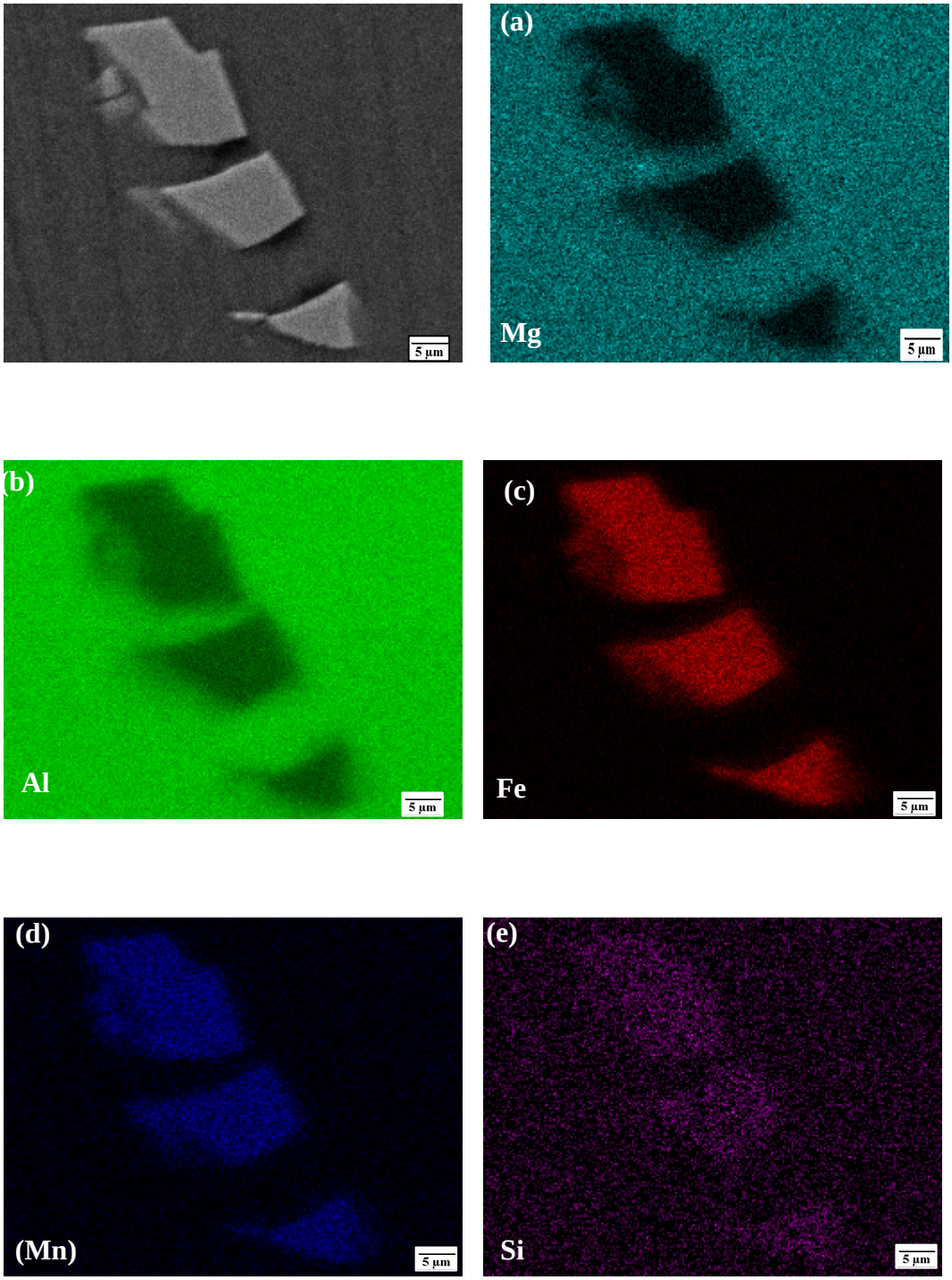

Figure 4.10. X-ray maps showing (a) Mg (b) Al (c) Mn (d) Fe (e) Si in specimens sensitized at 100^{o}C for 168 h.

dark particles are Al-Fe-Mn rich particle and Mg-Si-(Fe) rich particle, respectively which is consistent with EDS point analysis (Figures 4.8(a) and 4.8 (b)).

To know the phases at the grain boundaries and also to know their distribution, etched specimens were analysed using EDS. Figures 4.11 (a) – (c) show SEM micrographs of etched specimens while Table 4.4 shows magnesium content in the as-received and sensitized specimen. It can be seen that the intermetallics particles at the grain boundaries had been seriously attacked by the etchant to the extent that they are completely corroded and no particles found on the grain boundaries as pointed out by the arrows. The table shows that there is a little variation in magnesium content in the as-received specimen and also in the sensitized specimen but it did not follow any specific trend.

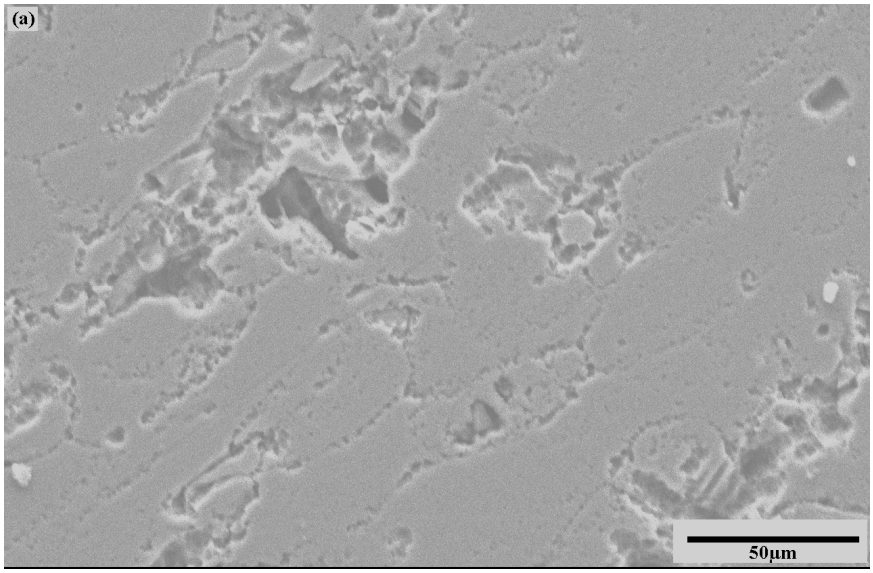

Figure 4.11 (a). SEM micrograph of etched as-received samples.

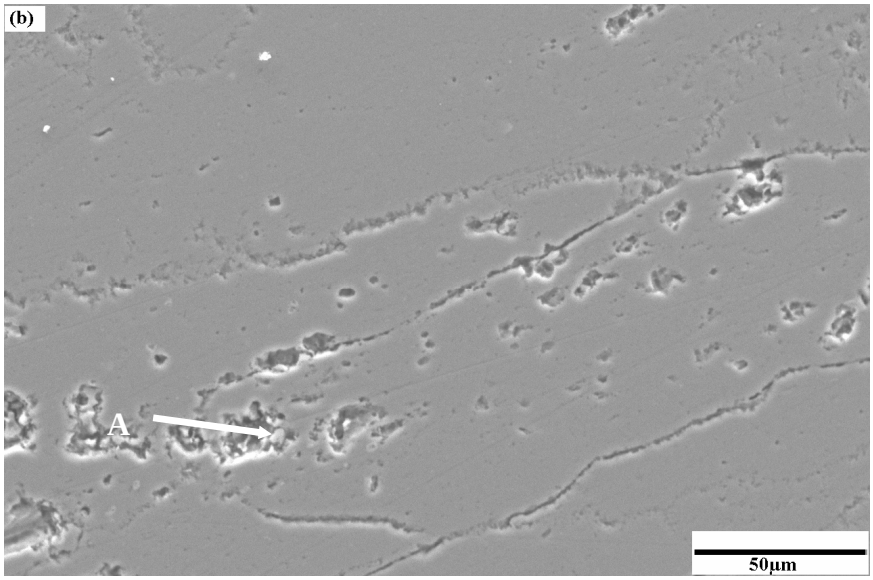

Figure 4.11 (b). SEM micrograph of etched samples sensitized at 100^{o}C for 168 h showing Al-Fe-Mn-rich particle (arrow A).

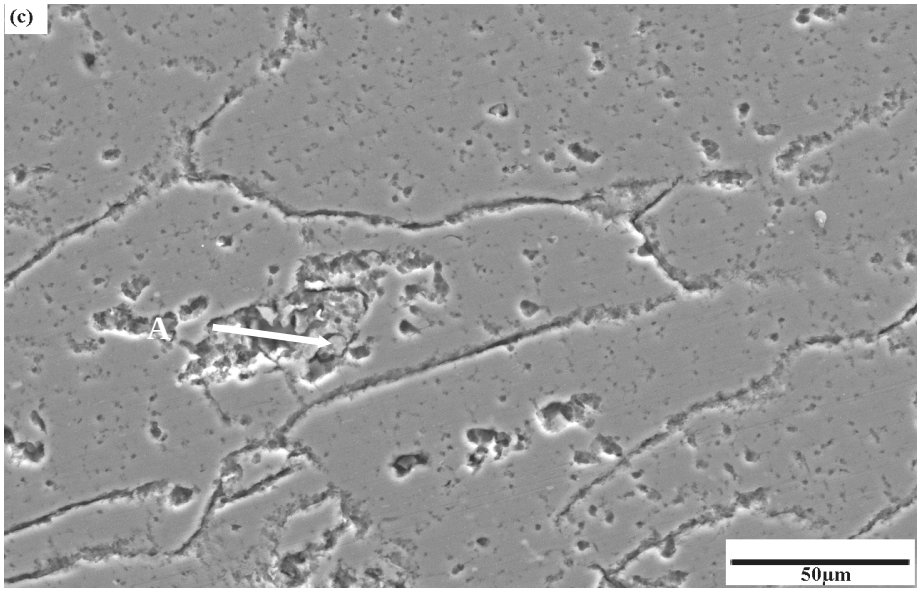

Figure 4.11 (c) SEM micrograph of etched sensitized samples at 100^{o}C for 672 h showing Al-Fe-Mn particle (arrow A).

Figure 4.12 show X-ray maps showing the distribution of magnesium, aluminum, silicon, manganese and iron in the intermetallics phases. The X-ray maps did not show any evidence of magnesium diffusion to the grain boundaries. Therefore, reduction in mechanical properties (hardness and tensile strength) at elevated sensitization temperatures and longer time could not be credited to diffusion of magnesium to the grain boundaries.

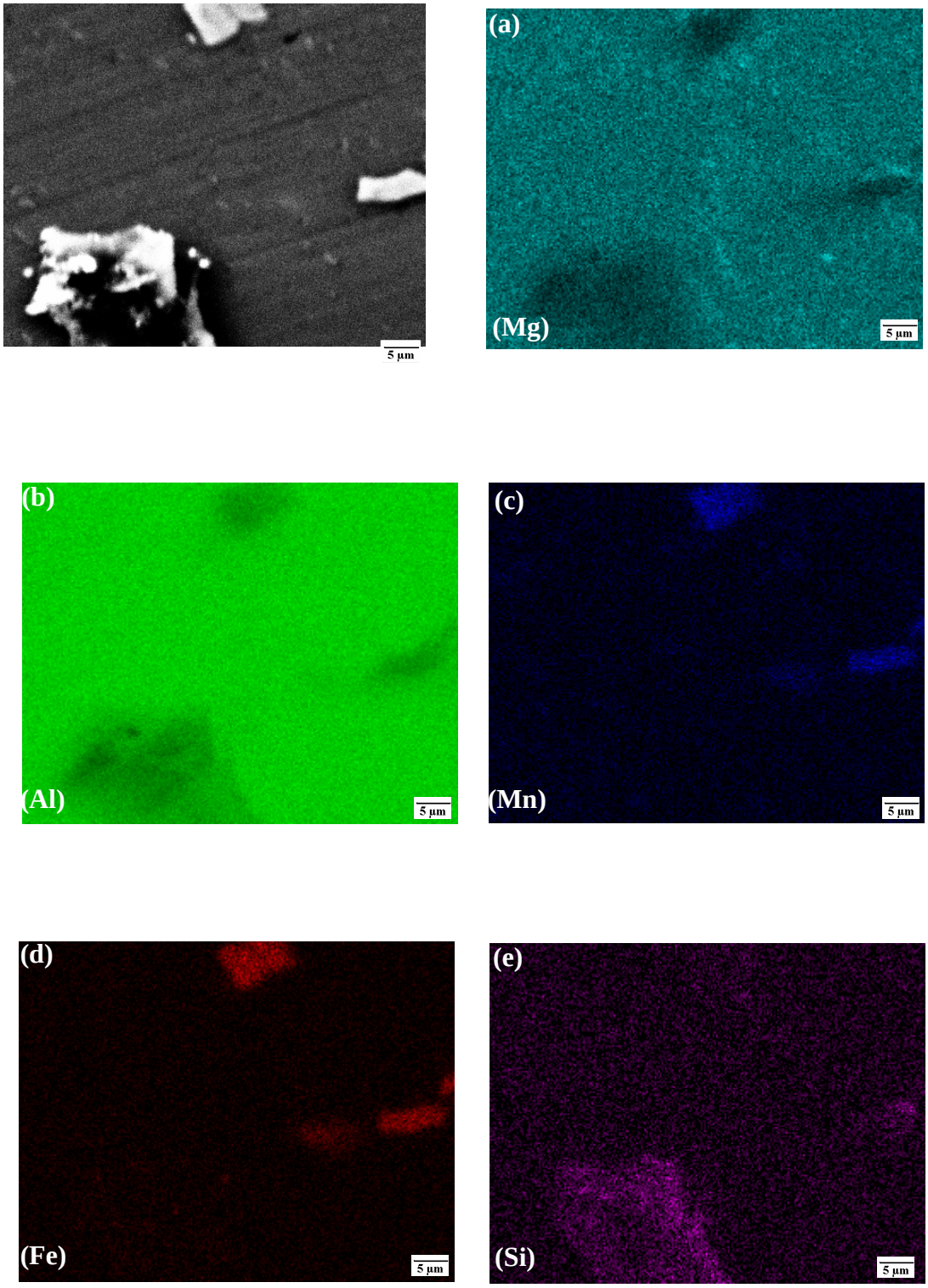

Figure 4.12. X-ray maps showing (a) Mg (b) Al (c) Mn (d) Fe (e) Si in Al-Fe-Mn

4.3 Effect of Sensitization on IGC Susceptibility

The effect of sensitization on the intergranular corrosion susceptibility of AA5083 is presented. The results gave adequate knowledge on the safe environmental/processing temperature and duration when the material could be used without being vulnerable to IGC.

Figure 4.13 shows the effect of sensitization temperature and time on the susceptibility of AA5083-H116 to IGC for specimens sensitized at 80^{o}C, 100^{o}C, 175^{o}C and 200^{o}C for up to 672h (4 weeks) using nitric acid mass loss test (NAMLT). It can be seen that the susceptibility of this material to IGC, which is measured in terms of mass loss per unit area (mg/cm^2), increased with sensitization temperature and resident time at a given temperature. According to ASTM G-67 standards [63], when the mass loss per unit area of a material subjected to the NAML test is less than or equal to 15 mg/cm^2, the material is considered to be resistant to IGC but when it is greater than or equal to 25 mg/cm^2, then the material is susceptible to IGC. For intermediate mass loss, metallographic examination is required to establish whether or not the loss in mass is due to the intergranular attack. Figure 4.14 shows test specimens sensitized at 150^{o}C for various sensitization times immersed inside nitric acid for 24h. The colour variation indicates that the degree of acid attack on the specimens varied. It is worthy to note in Figure 4.13 that the susceptibility to IGC at 150^{o}C and 175^{o}C is greater than at 200^{o}C, thus indicating the existence of a critical sensitization temperature somewhere between 150^{o}C and 200^{o}C where susceptibility to IGC is the highest. This finding is consistent with the results in reference [80], where it was reported that the temperature where the precipitation rate of the β phase reached a maximum was between 150^{o}C and 200^{o}C.

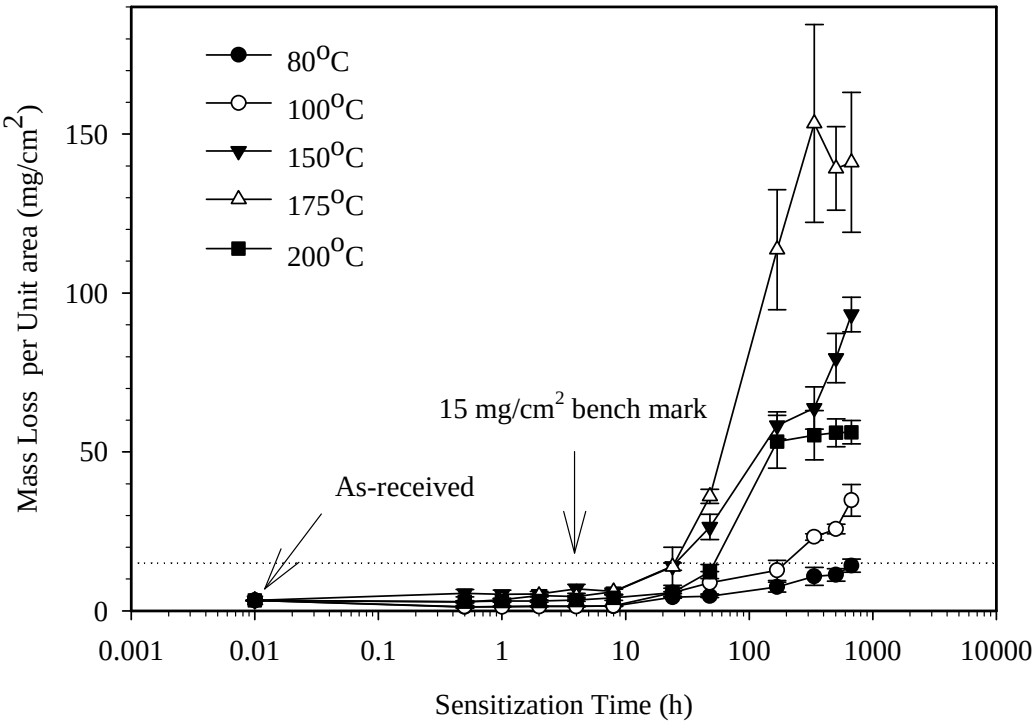

Figure 4.13. Effect of sensitization temperatures and time on the susceptibility of AA5083-H116 to IGC. Note: The error bars are standard deviation.

The minimum resident times for this alloy to be susceptible to IGC at various sensitization temperatures were read from Figure 4.13 and shown in Table 4.5.

It is apparent from Figure 4.13 that mass loss per unit area for specimens sensitized at 175°C decreased after 336 h (2 weeks). Van der *et al.* [80] reported that the precipitation rate of β phase (Al_3Mg_2) in AA5083 reduced after 200°C due to increased solubility of magnesium in aluminum. The author in reference [25] also reported that whenever random precipitation of Al_3Mg_2 occurs within the grains and along the grain boundaries due to heat treatment, susceptibility to both IGC and SCC would be reduced as a result of reduction in corrosion current density on each anodic region. Therefore, the reduction

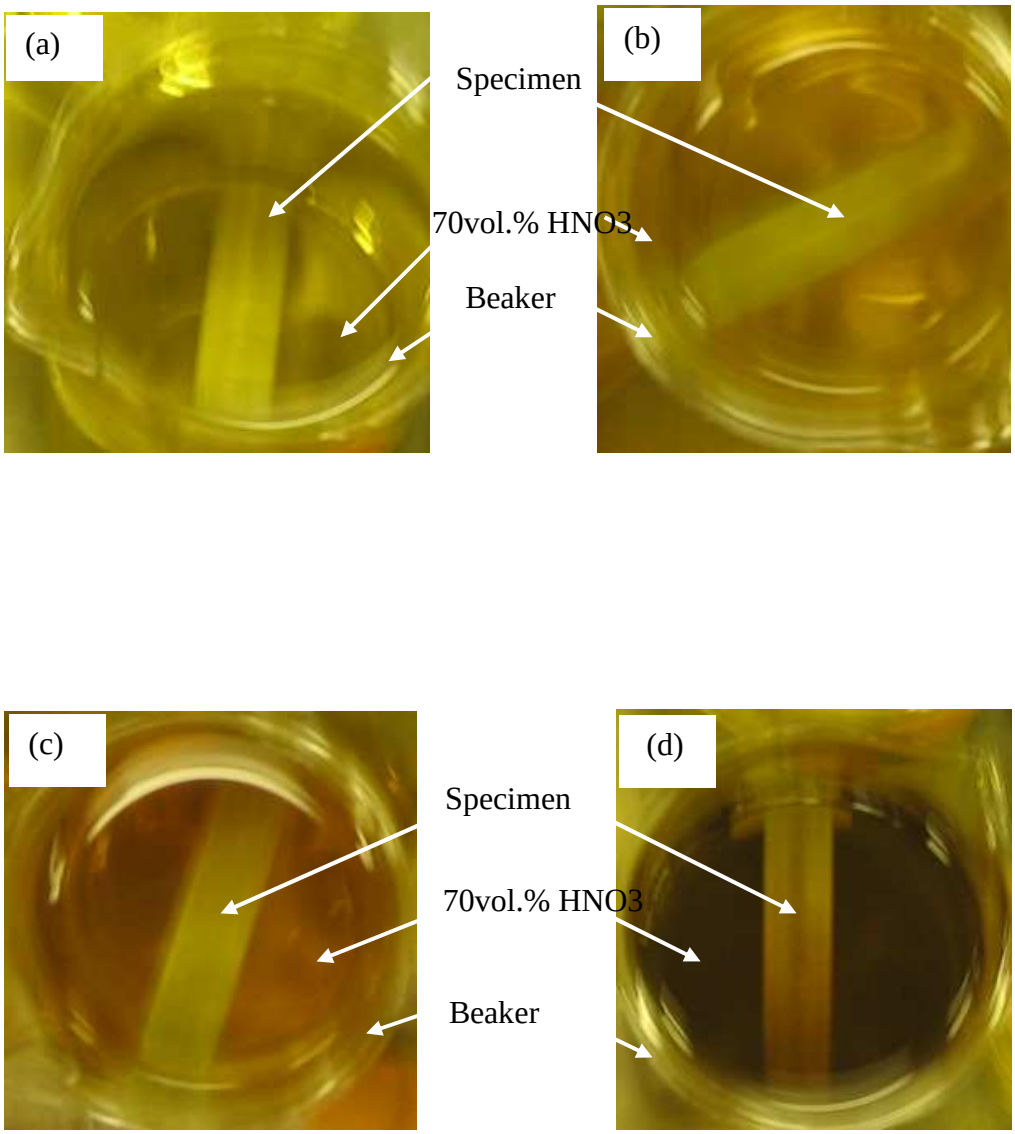

Figure 4.14. Samples sensitized at 150^{o}C for duration of (a) 4 h, (b) 24 h, (c) 168 h and (d) 672 h immersed inside nitric acid for 24 h.

in mass loss after 336 h (2 weeks) for specimens sensitized at 175^{o}C is believed to be due to precipitation of Al_3Mg_2 within the grains.

Table 4.5. Minimum resident time for AA5083-H116 to be susceptible to IGC at various temperatures.

Sensitization temperature (^{o}C)	80	100	150	175	200
Critical Time (h)	*	209.0	26.0	25.5	55.0

***** indicates that the material was not vulnerable to IGC for the entire test period.

To determine the critical temperature (and the corresponding time) at which the sensitization of AA5083-H116 is most rapid, a C-curve (see Figure 4.15) was generated from Figure 4.13 by drawing a horizontal line at NAML value of 15 mg/cm^2 and extracting the corresponding temperature data. It can be seen that the critical temperature and critical resident time are approximately 165^{o}C and 10h, respectively. To ensure the reproducibility of this procedure, C-curves were also generated for NAML values of 25 and 30 mg/cm^2 and the resultant critical temperature was consistent with that determined for 15 mg/cm^2. Sampath *et al*. [7] have reported that the critical temperature for precipitation of Mg containing intermetallics in AA5083-O is approximately 150^{o}C, which is consistent with what had been reported for precipitation of Mg_5Al_8 in Al-Mg alloys by Perryman *et al*. [81]. The NAMLT results show that the as-received specimens and specimens sensitized at 80^{o}C for 672h (4 weeks) are resistant to IGC but at higher temperatures (from 100^{o}C to 200^{o}C), the material is vulnerable to IGC.

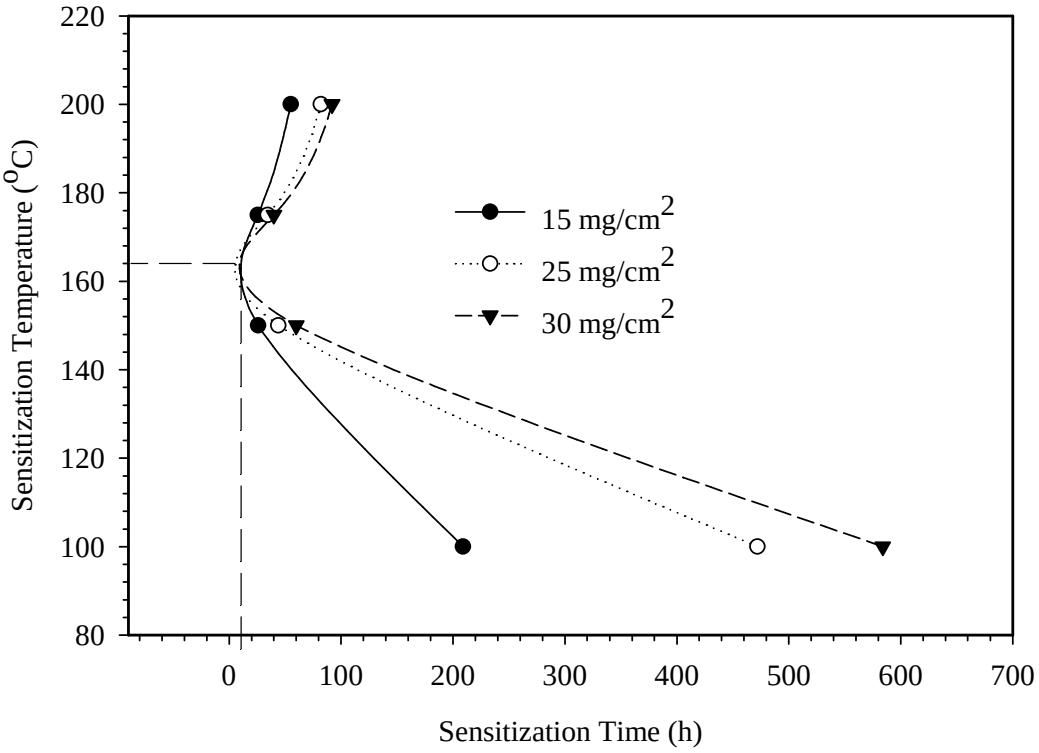

Figure 4.15. Time-temperature curves for determining the critical sensitization temperature and time for AA5083-H116.

Table 4.6 shows the effect of sensitization on the IGC susceptibility of two tempers of AA5083. The data for AA5083-O temper were taken from the work of Sampath *et al.* [7] while those of AA5083-H116 are from the present study. It is obvious that the susceptibility of AA5083-H116 material to IGC is greater than that of AA5083-O. The difference in the level of susceptibility to IGC could therefore be attributed to temper treatment. Temper H116 involves strain hardening of materials with a special control of temperature while temper O is simple annealing of the material. During annealing heat treatment, rearrangement of dislocations to produce more stable configuration occurs

Table 4.6. Variation in susceptibility of AA5083 to IGC with temper treatment.

Sensitization temperature →	Mass loss per unit area (mg/cm^2)							
	100°C		150°C		175°C		200°C	
Sensitization time(h)	O*	H116	O*	H116	O*	H116	O*	H116
168	5	12.7	30	58.4	32	113.7	30	53.2
336	13	34.8	34	93.2	36	141.1	33	56.2

* Data taken from Reference [7].

which enhances resistance to stress corrosion cracking [82]. The rearrangement of dislocation may have direct influence on the microstructure of the grain boundaries which led to the observed improvement in IGC resistance of O temper-treated materials.

4.4 Effect of Sensitization on Mechanical Properties

4.4.1 Hardness

Microhardness measurements were performed on the as-received and sensitized materials to evaluate the effect of sensitization on the hardness of AA5083-H116. Figures 4.16 and 4.17 show the variation of microhardness with sensitization temperature and time for the alloy in the longitudinal direction (LD) and the transverse direction (TD), respectively. The average hardness values of the as-received material in the LD and TD directions are 97 and 95 VHN, respectively, which are in agreement with the values reported in the literature [83-84]. It can be observed that the hardness

decreased with increasing sensitization temperature and time for both directions. Also, it is interesting to note that hardness along the longitudinal direction for both as-received and sensitized samples is slightly greater than that along the transverse direction (see appendix A and B for the average values and standard deviation of the measurements and hardness versus sensitization time charts of both longitudinal and transverse direction on the same axes respectively). Authors in references [76-78] reported that variation of grain size and dislocation density along different rolling directions which occur during heat treatments leads to variation of hardness. The reduction in hardness with sensitization temperature and time can be explained with the effect of sensitization on the microstructure of sensitized materials as observed in Figures 4.4 - 4.6 which leads to the more reduction in dislocation density of specimens sensitized at 200^{o}C as shown Figure 4.5. This may also account for the drastic changes in hardness of specimens sensitized at elevated temperatures (175^{o}C and 200^{o}C) compared to those of the as-received specimens and specimens annealed at lower sensitization temperatures (100^{o}C and 150^{o}C).

Based on the findings presented in this section, it should be possible to determine whether or not the material has been sensitized based on simple hardness measurements and also, sensitization time or temperature could be estimated if one of the parameters is known.

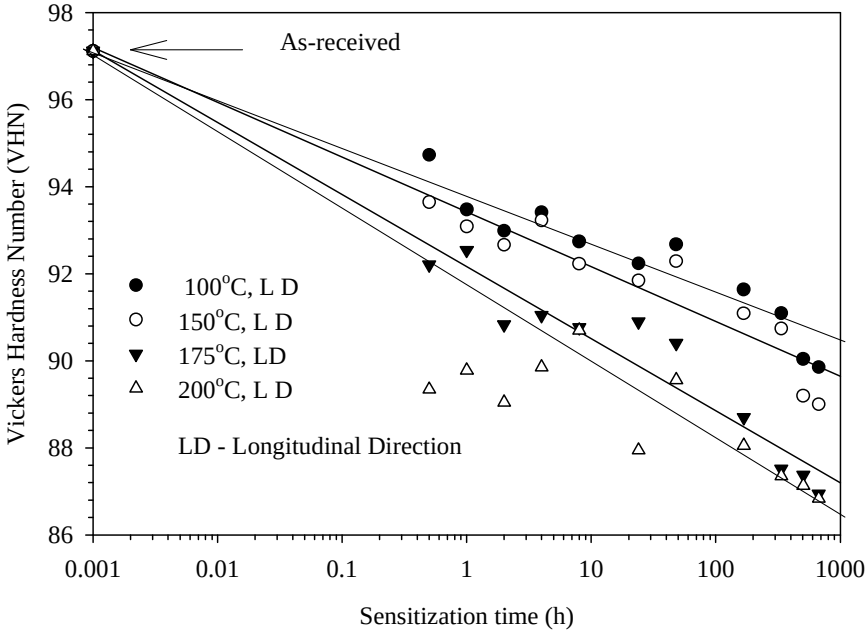

Figure 4.16. Variation of hardness with sensitization temperature and time along the longitudinal direction.

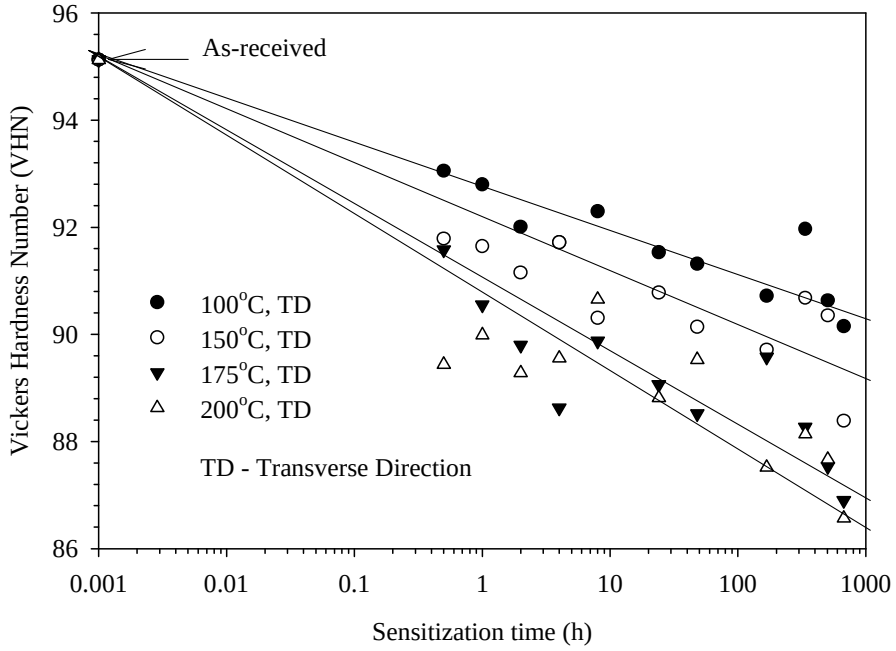

Figure 4.17. Variation of hardness with sensitization temperature and time along the transverse direction.

4.4.2 Tensile and Yield Strengths

The effect of sensitization temperature and time on the tensile properties of AA5083 was studied by performing tensile tests on the as-received and sensitized specimens. The results were used to compute tensile and yield strengths.

Figures 4.18- 4.21 show the stress versus strain curves obtained for the as-received and sensitized materials. The tensile and 0.2% offset yield strengths reported here were determined from these curves. It can be seen that there was a slight variation in stress–strain curves of AA5083-H116 as sensitization temperature and time increased. The variation in the tensile strength of the tested specimens with annealing temperature and time is shown in Figure 4.22. The curves show similar trend except that there was a reduction in tensile strength with increasing sensitization temperature and time. The tensile strength of specimens sensitized at 100^{o}C remained virtually constant up to 336h before an appreciable reduction in tensile strength set in.

This reduction in tensile with sensitization temperature and time can be attributed to the same effect of sensitization on the microstructure of sensitized materials as observed in Figures 4.4 - 4.6. The variation in tensile which was as a result of heat treatments can also be explained with the variation of grain size and dislocation density along different rolling directions of stock plate [76-78]. Therefore, variation of grains size and dislocation density due to sensitization may account for the drastic changes in tensile of specimens sensitized at elevated temperatures (175^{o}C and 200^{o}C) compared to those of

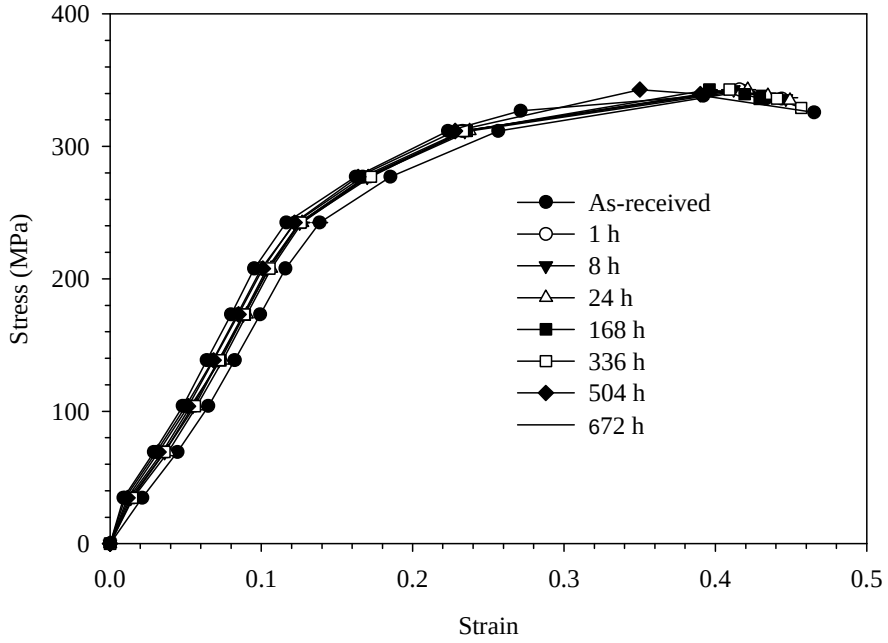

Figure 4.18. Stress versus strain curves for as-received and sensitized specimens at 100°C.

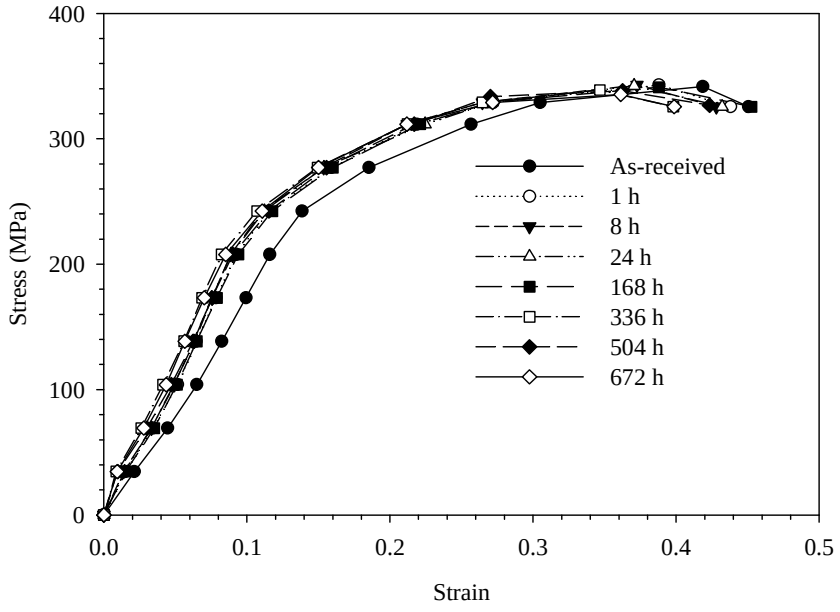

Figure 4.19. Stress versus strain curves for as-received and sensitized specimens at 150°C.

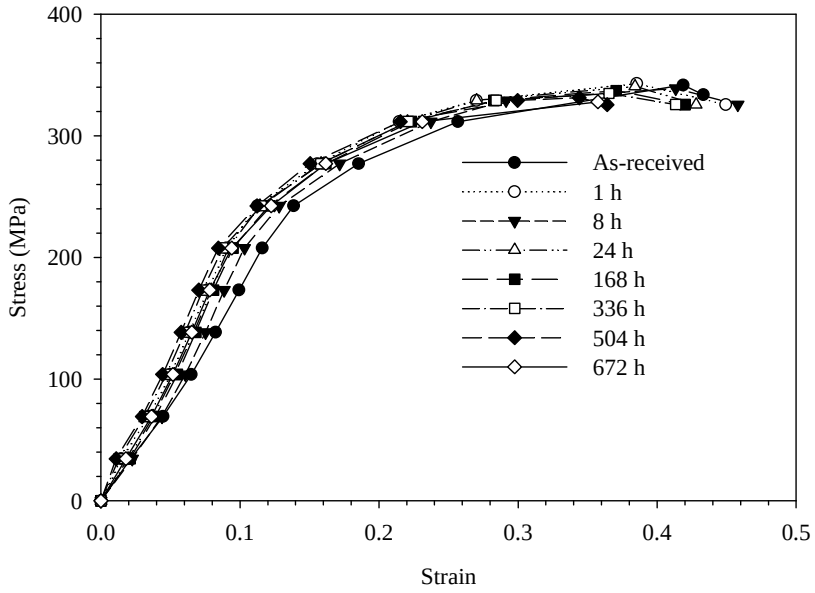

Figure 4.20. Stress versus strain curves for as-received and sensitized specimens at 175^{o}C.

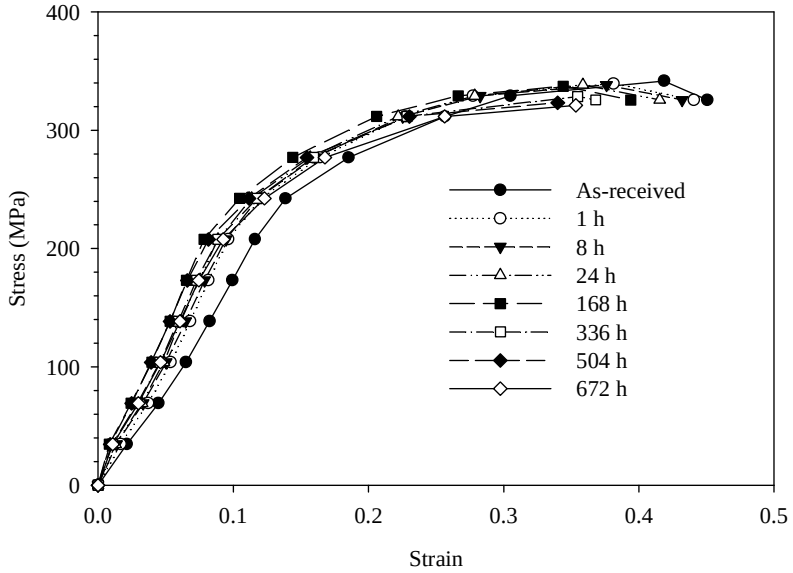

Figure 4.21. Stress versus strain curves for as-received and sensitized specimens at 200^{o}C.

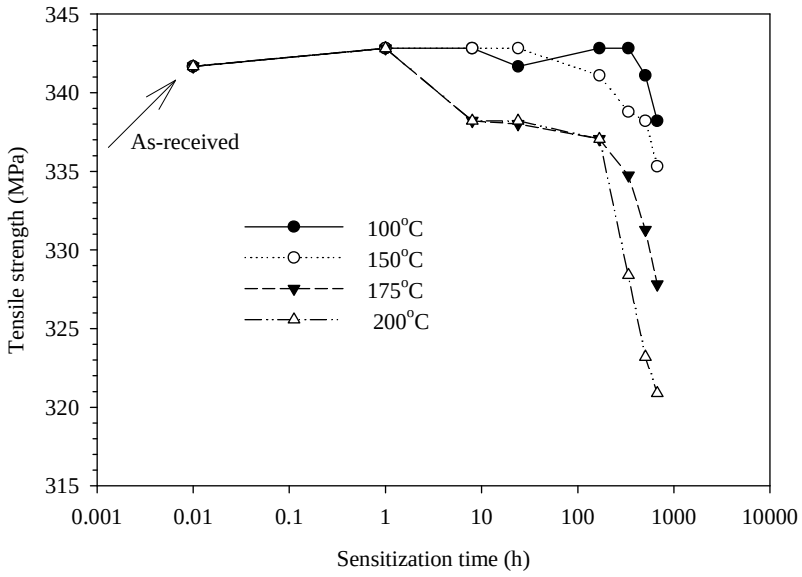

Figure 4.22. Variation of tensile strength with sensitization temperature and time.

the as-received specimens and specimens annealed at lower sensitization temperatures (100°C and 150°C).

Figure 4.23 shows the variation of yield strength of the tested specimens with sensitization temperature and time. It can be seen that the yield and tensile strength curves show a similar trend. It is obvious that the yield strength of the specimen sensitized at 200°C was seriously affected compared to the samples sensitized at lower temperatures. The reduction in yield strength with sensitization temperature and time can also be explained with the same microstructural changes that occurred during sensitization.

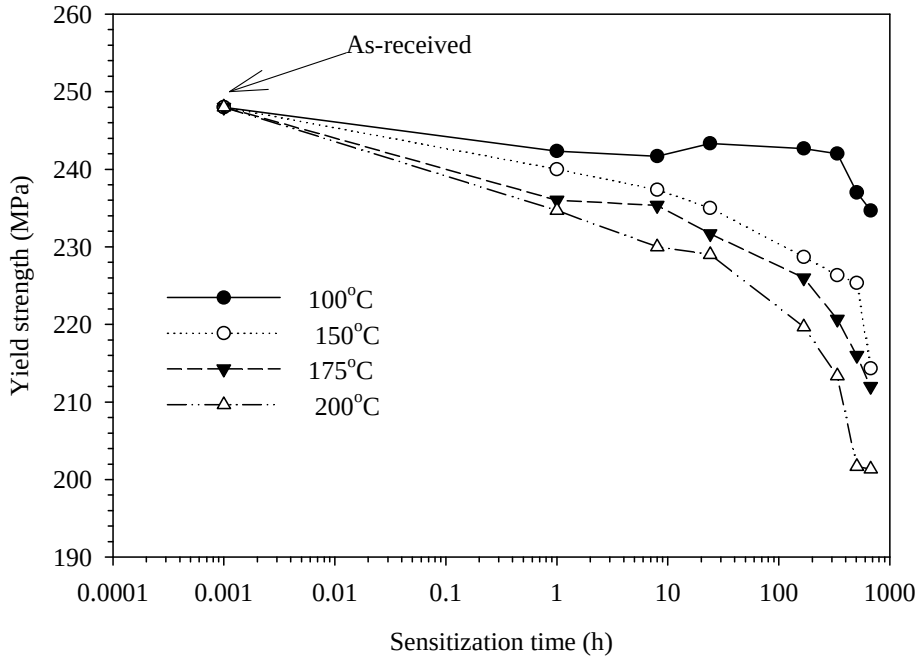

Figure 4.23. Variation of yield strength with sensitization temperature and time.

The average tensile and yield strengths of the as-received sample were calculated to be 341 MPa and 248 MPa, respectively which are slightly greater than 315-317 MPa and 228-230 MPa quoted, respectively for AA5083-H116 in Reference [29,80]. In general, both the yield and tensile strengths of the as-received material are greater than that of sensitized samples. Both the strength and hardness properties of AA5083-H116 are affected more at elevated sensitization temperature and longer time than specimen sensitized at lower temperatures and below for shorter time.

The fracture surfaces of the tensile specimens of the as-received and sensitized specimens were examined with a JEOL JSM Model 5900 LV SEM to characterize the failure modes. Figures 4.24 (a) – (d) show the SEM fractographs of the as-received

specimen and specimen sensitized at 100^{o}C for different lengths of time. The fracture surfaces displayed a wide range of dimple sizes, cleavage, intermetallic particles and particle fracture.

White arrows A, B and C on the fractographs represent Al-Fe-Mn rich particle, Mg-Si particles and particle crack, respectively. Brittle fracture features and ductile features (dimples) were seen on the fractographs. Many of the dimples were initiated by the fracture of particles while some were initiated at interfaces between the matrix and intermetallics particles. Figures 4.24 (a) – (d) show that samples sensitized for 672h have more brittle fracture features compared to other sensitization time. Figures 4.25 (a) – (b) show qualitative EDS point analysis of Al-Fe-Mn rich particle and Mg-Si rich particle.

Similar fracture surface features were observed for samples sensitized at 150^{o}C and 200^{o}C as shown in Figures 4.26(a) – (c) and 4.27 (a) - (c), respectively. In addition to the features mentioned above, matrix crack was found on sample sensitized at 200^{o}C and it was indicated with arrows labelled D. Qualitative EDS point analysis of particles shown in Figures 4.26 (a) – (c) and 4.27 (a) – (c) were shown on Figure 4.28 (a) - (b).

The worst scenario in deterioration of hardness, tensile and yield strengths observed in specimens sensitized for 672 h could therefore, be explained with variation in the level of brittleness of sensitized specimens with increasing sensitization time. The more the brittleness features in any material, the lower the strength and hardness properties. The

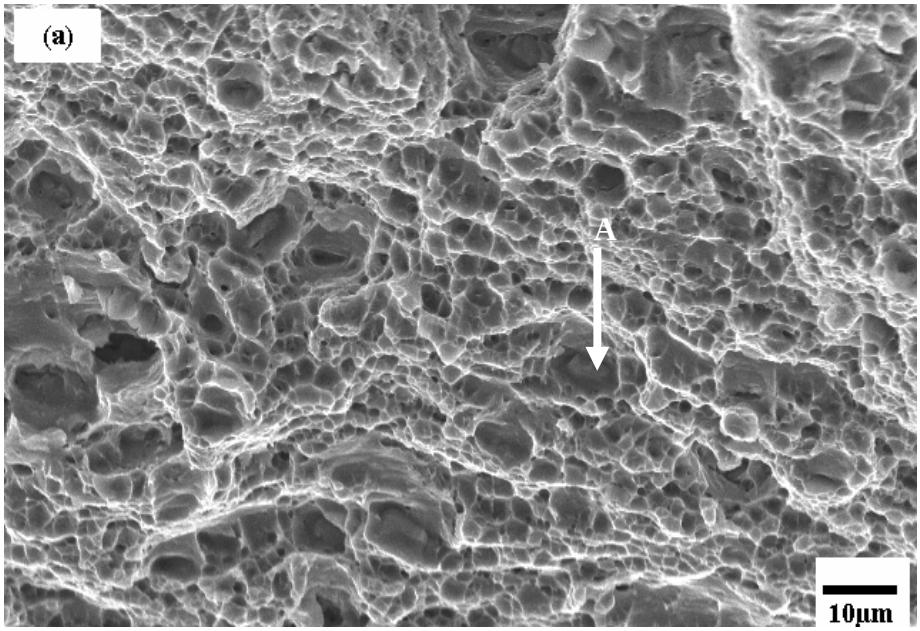

Figure 4.24 (a). Typical SEM fractograph of as-received tensile specimens showing Al-Fe-Mn particle (arrow A).

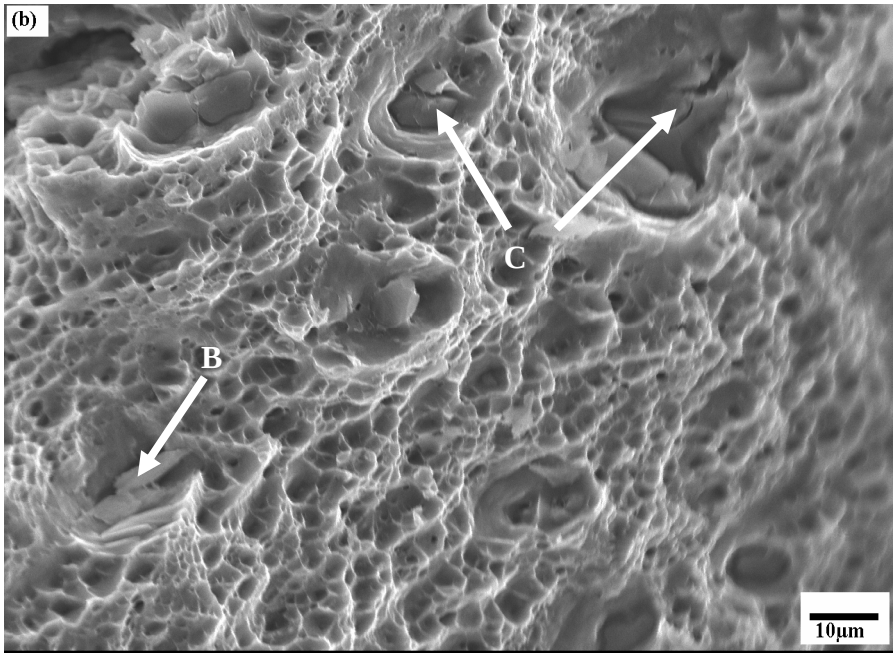

Figure 4.24 (b). Typical SEM fractograph of tensile specimens sensitized at 100^{o}C for 168 h showing Mg-Si particle (arrow B) and particle crack (arrow C).

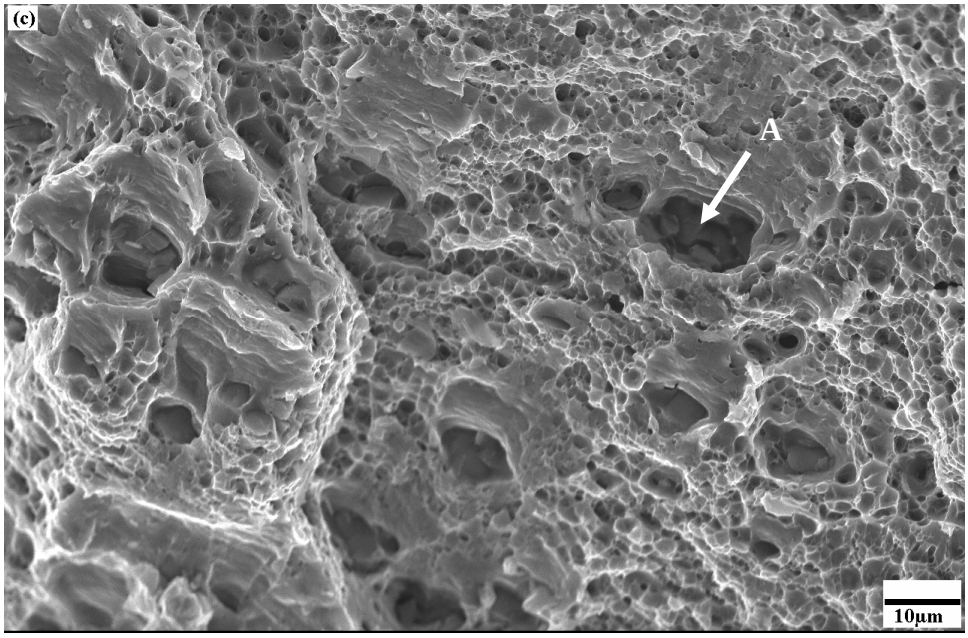

Figure 4.24 (c). Typical SEM fractograph of tensile specimens sensitized at 100^{o}C for 336 h showing Al-Fe-Mn particle (arrow A).

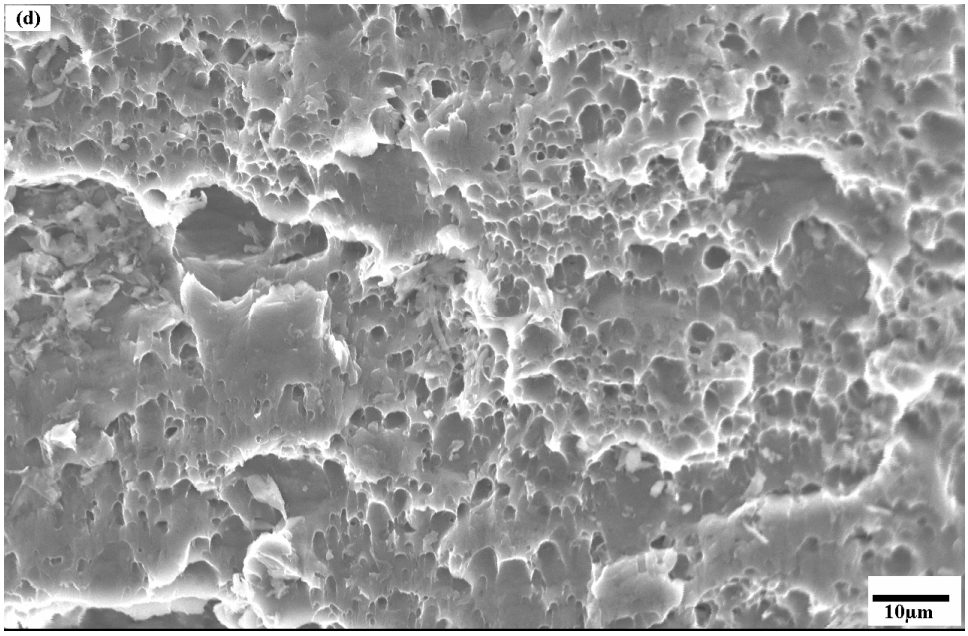

Figure 4.24 (d). Typical SEM fractograph of tensile specimens sensitized at 100^{o}C for 672 h.

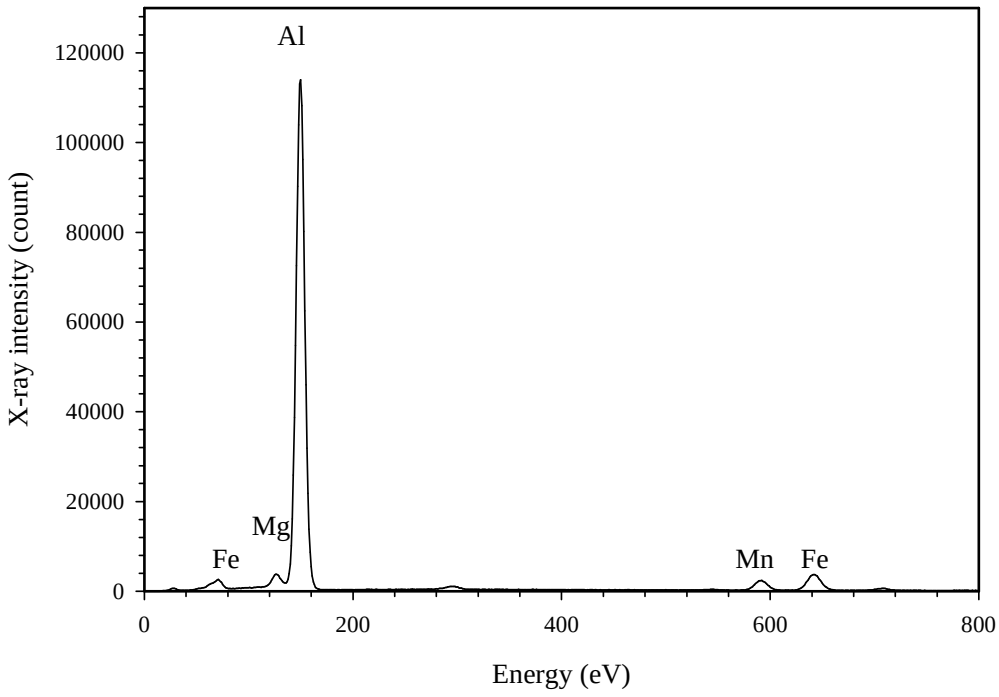

Figure 4.25 (a). EDS spectrum of Al-Fe-Mn rich particle.

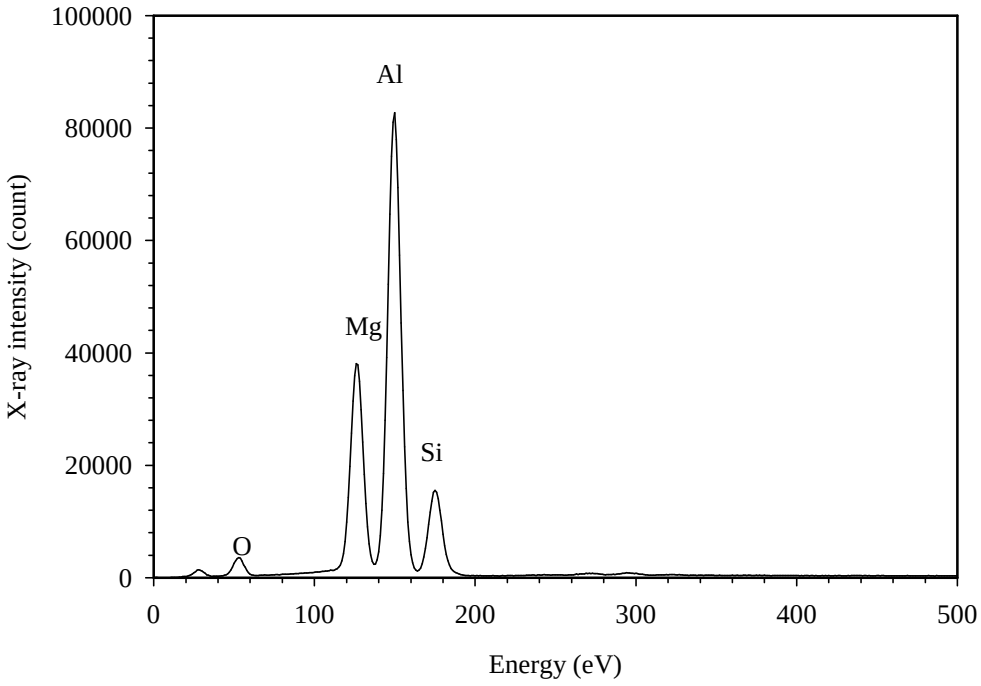

Figure 4.25 (b). EDS spectrum of Mg-Si rich particle.

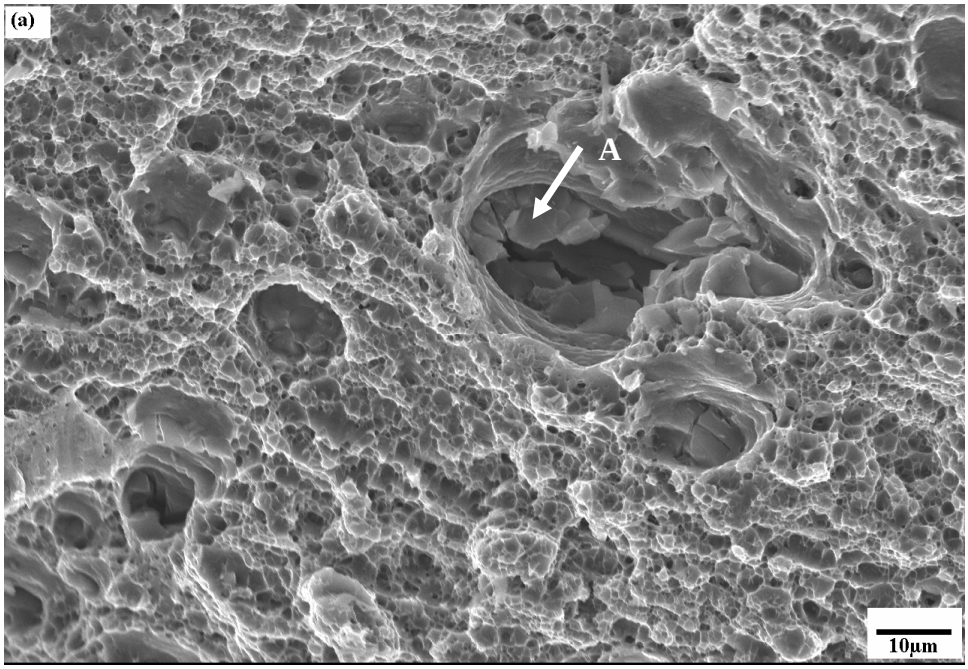

Figure 4.26 (a). Typical SEM fractograph of tensile specimens sensitized at 150^{o}C for 168 h showing Al-Fe-Mn particle (arrow A).

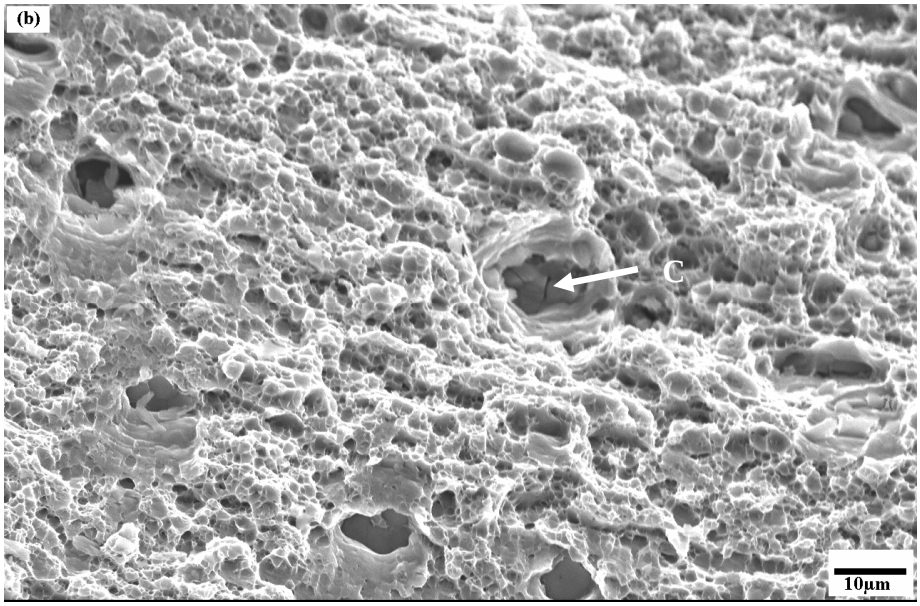

Figure 4.26 (b). Typical SEM fractograph of tensile specimens sensitized at 150^{o}C for 336 h showing particle crack (arrow C).

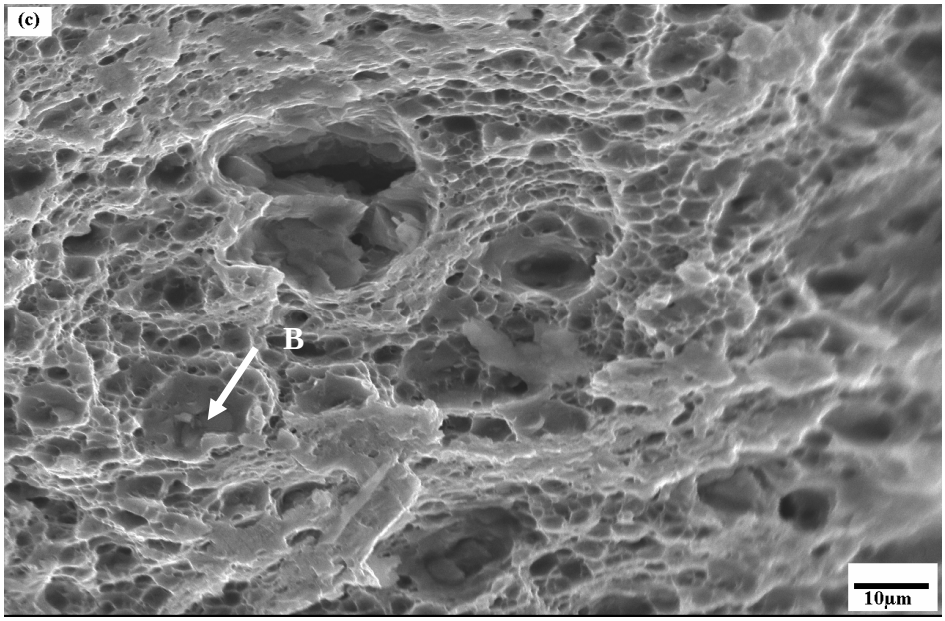

Figure 4.26 (c). Typical SEM fractograph of tensile specimens sensitized at 150^{o}C for 672 h showing Mg-Si particle (arrow B).

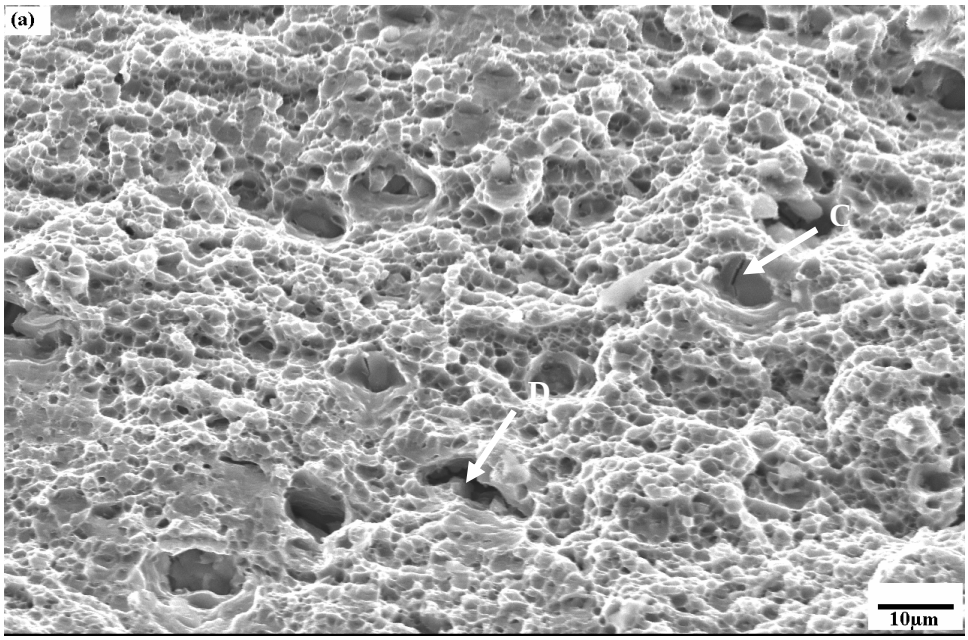

Figure 4.27 (a). Typical SEM fractograph of tensile specimens sensitized at 200^{o}C for 168 h showing particle crack (arrow C) and matrix crack (arrow D).

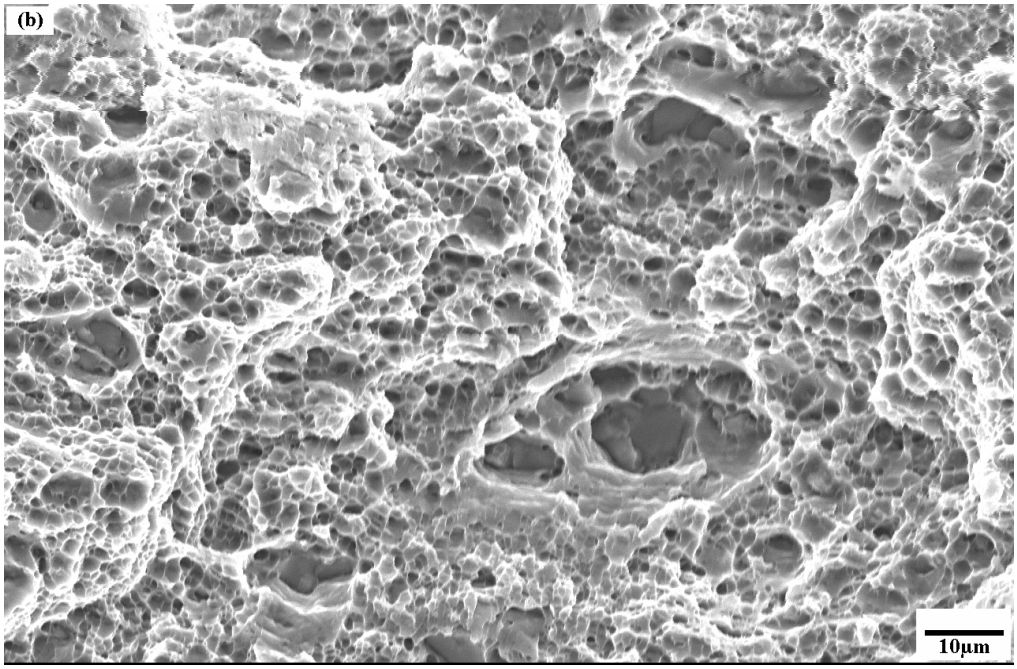

Figure 4.27 (b). Typical SEM fractograph of tensile specimens sensitized at 200^{o}C for 336 h.

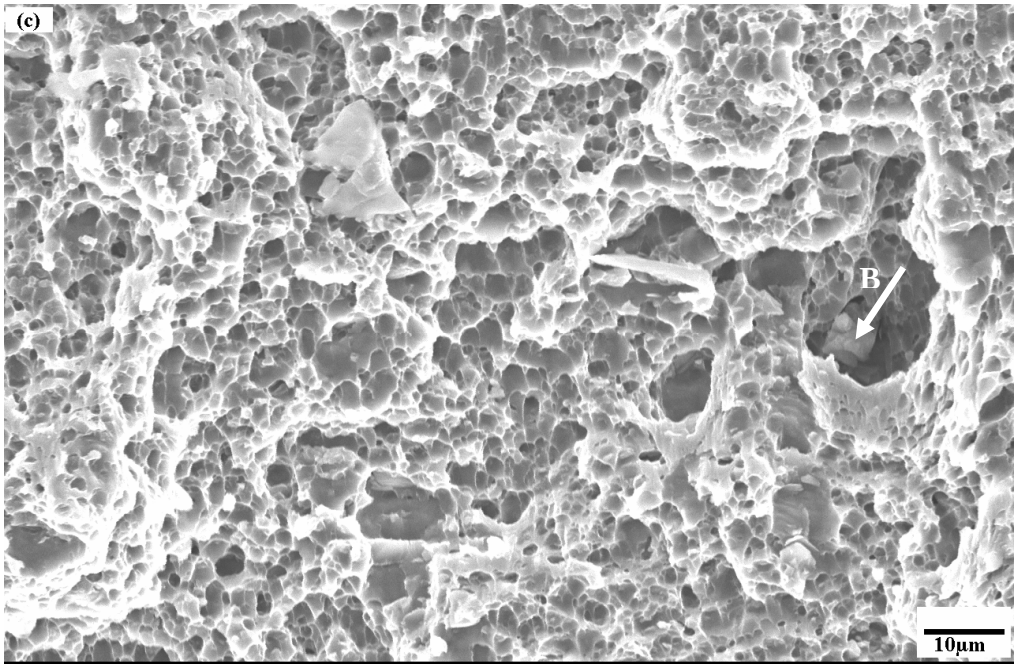

Figure 4.27 (c). Typical SEM fractograph of tensile specimens sensitized at 200^{o}C for 672 h showing Mg-Si particle (arrow B).

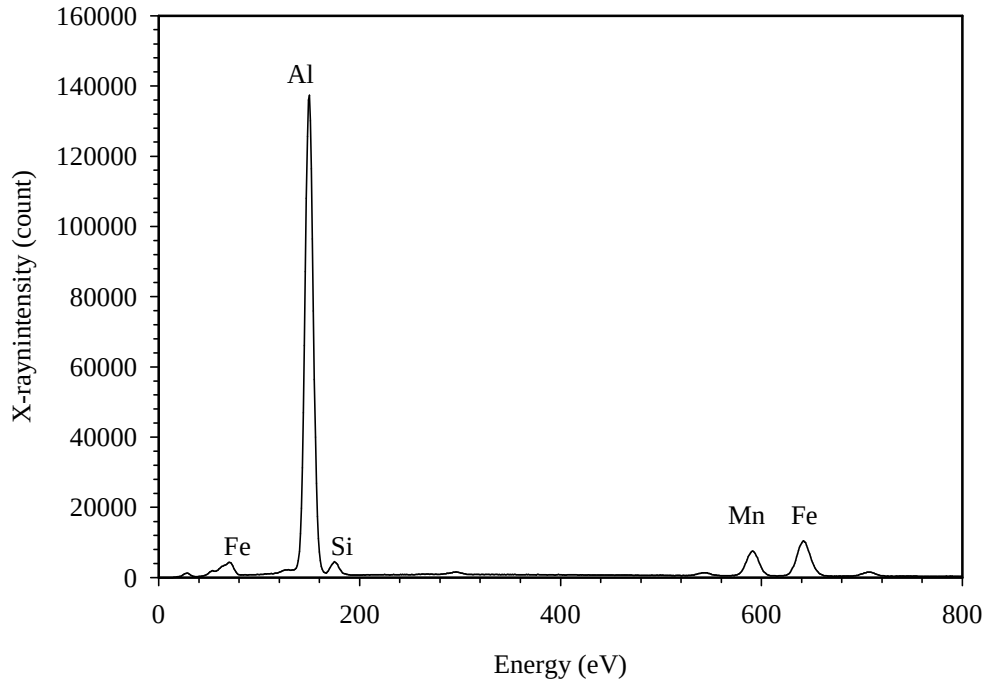

Figure 4.28 (a). EDS spectrum of Al-Fe-Mn-rich particle (arrow A).

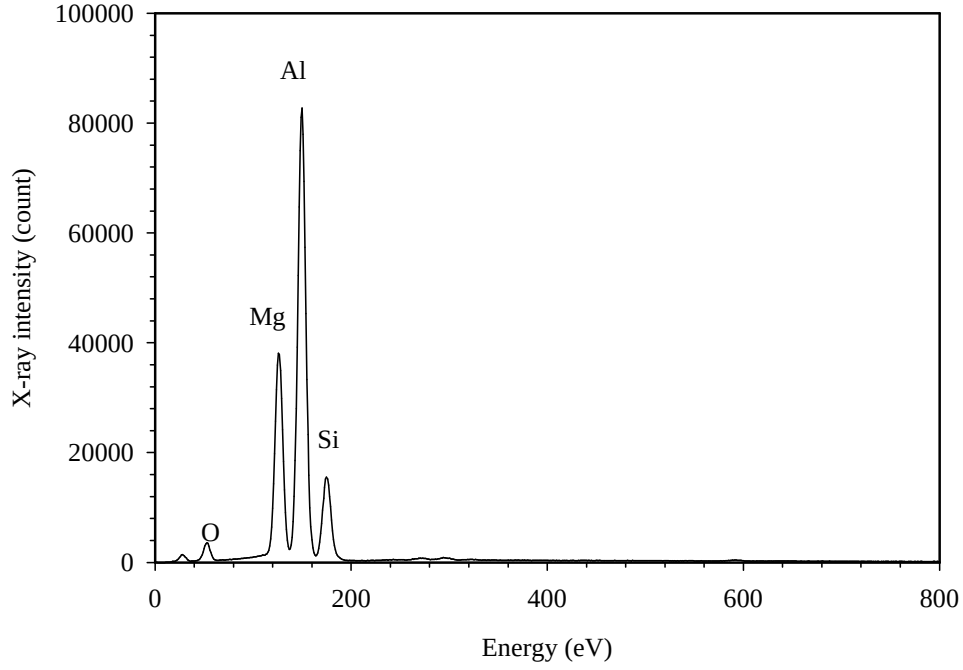

Figure 4.28 (b). EDS spectrum of Mg-Si-rich particle (arrow B).

fracture surface studied also revealed that the failure mechanisms of this material subjected to any mechanical loading can be ascribed to the particle and matrix cracking.

5. CONCLUSIONS AND RECOMMENDATIONS

5.1 Conclusions

In this work, both as-received and sensitized AA5083-H116 were characterized using different experimental techniques such as inductively coupled plasma/mass spectrometry (ICP/MS), microhardness measurements, tensile test, optical microscopy, scanning electron microscopy (SEM), energy dispersive X-ray spectrometry (EDS) and nitric acid mass loss test (NAMLT). Sensitization was carried out at different temperatures for various lengths of time. The following conclusions are drawn from the study.

5.1.1 Mechanical Properties

All the mechanical properties investigated in this study were adversely affected by increasing sensitization temperature and time. The worst scenario occurs at the highest sensitization temperature and time. These effects are attributed to a reduction in dislocation density at elevated temperatures and, depending on the sensitization temperature, to recrystallization. The hardness measurement data could be used to determine whether the material has been sensitized or not. Besides, sensitization temperature or time could be evaluated if one of the parameters is known.

5.1.2 Intergranular Corrosion Susceptibility

The resistance of AA5083-H116 to IGC generally decreased with increasing sensitization temperature and time. The minimum sensitization time required for this material to be vulnerable to IGC was established for different sensitization temperatures and the least time (10h) corresponds to 165^{o}C, which is the critical temperature. The as-received specimen and specimens sensitized at 80^{o}C for 672h (4 weeks) were resistant to IGC but at higher temperatures (from 100^{o}C to 200^{o}C) the material is vulnerable to IGC only if the sensitization time is up to or above the minimum time established for the temperature.

5.1.3 Microstructure

Two main intermetallic phases were found in AA5083-H116. These are Al-Fe-Mn and Mg-Si phases. The failure of this material under tension is attributed to particle and matrix cracking.

In this study, it can be generally concluded that sensitization of the alloy at higher temperatures is detrimental to both tensile, hardness properties and corrosion resistance.

5.2 Recommendations

The following investigations are suggested for future work to enable a better understanding of stress corrosion cracking of AA5083.

1. A detailed study of grain boundary structures using analytical electron microscopy (TEM, EELS) should be carried out to enable better understanding of the various precipitates that form on the grain boundaries and their effects on the properties of AA5083-H116.
2. The effect of pH and temperature on stress corrosion cracking behaviour of AA5083 should be evaluated by varying the pH and temperature of the corrosive medium.
3. Bent-beam stress corrosion cracking experiment should be performed to have better understanding of the stress corrosion cracking behaviour of AA5083.

REFERENCES

1. G. B. Burger, A. K. Gupta, P. W. Jeffrey and D. J. Lloyd, "Microstructural Control of Aluminum Sheet Used in Automotive Applications", *Materials Characterization,* Vol. 35, n1, (1995), 23-29.
2. Borvik Toore, Clausen Arild H, Hopperstad Odd Sture and Langseth Magnus, "Perforation of AA5083-H116 Aluminium Plates with Conical-nose Steel Projectiles", *International Journal of Impact Engineering,* Vol. 30, n4, (2004), 367-384.
3. J. S. Vetrano, R. E. Williford and R. H. Jones, "Influence of Microstructure and Thermal History on the Corrosion Susceptibility of AA5083", in Automotive Alloys I, edited by S.K. Das, TMS Annual Meeting, Orlando, FL, (The Minerals, Metals and Materials Society, Warrendale, PA), (1997), 77-85.
4. D. R. Baer, C. F. Windisch, Jr., M. H. Engelhard, M. J. Danielson, R. H. Jones and J. S. Vetrano, "Influence of Mg on the Corrosion of Al", *Journal of Vac. Sci. Technol. A* 18 (1), (2000), 131-136.
5. M. O. Speidel and M. V. Hyatt, "Stress Corrosion Cracking of High Aluminum Alloys", in Advances in Corrosion Science and Technology, edited by M.G. Fontana and R.W. Staehle, Vol. 2, (1972), 115-335.
6. J. L. Searles, P. I. Gouma, and R. G. Buchheit, "Stress Corrosion Cracking of Sensitized AA5083 (Al-4.5Mg-1.0Mn)", *Metallurgical Materials Transasctions A* 32, (2001), 2561-2573.
7. D. Sampath, S. Moldenhauer, H. R. Schipper, K. Mechsner and A. Haszler, "Decomposition of Solid Solution of the AA5083 Alloy upon Exposure to Elevated Temperatures", *Materials Science Forum*, Vols. 331-337, (2000), 1089-1094.

8. Z. F. Wang, “The Effect of Microstructure on the Polarization and Stress Corrosion Cracking in Al-5 Mg Alloys”, (Paper presented at Corrosion /2000, Orlando, FL. 26-31 March 2000).
9. J. C. Chang and T. H. Chuang, “Stress Corrosion Cracking Susceptibility of the Superplastically Formed 5083 Aluminum Alloy in 3.5Pct. NaCl Solution”, *Metallurgical and Materials Transactions A*: Vol. 30A, n 12, (1999), 3191-3199.
10. http://www.uscg.mil/d13/units/msopuget/al%5Ffracturing.htm (25/01/2006).
11. R. H. Jones, D. R. Baer, M. J. Danielson and J. S. Vetrano, “Role of Mg in the Stress Corrosion Cracking of an Al-Mg Alloy”, *Metallurgical and Materials Transactions A*, Vol. 32A, (2001), 1699-1711.
12. R. H. Jones, “The Influence of Hydrogen on the Stress-Corrosion Cracking of Low-Strength Al-Mg Alloys”, *JOM*, Vol. 55, n2, (2003), 42-46.
13. R. H. Jones and C. F. Windissch Jr., “Stress Corrosion Cracking of Lightweight Automotive Materials”, *TMS Annual Meeting*, (2003), 43-54.
14. R. H. Jones, V. Y. Gertsman, J. S. Vetrano and C. F. Windissch Jr., “Crack-Particle Interactions During Intergranular Stress Corrosion of AA5083 as Observed by Cross-Section Transmission Electron Microscopy”, *Scripta Materialia*, Vol. 50, n 10, (2004), 1355-1359.
15. D. R. Baer, C. F. Windisch Jr., M. H. Engelhard, M. J. Danielson, R. H. Jones and J. S. Vetrano, “Influence of Mg on the Corrosion of Al”, *Journal of Vacuum Sci. and Tech. Part A*, Vol. 18, n1, (2003), 131-136.
16. J. L. Searles, P. I. Gouma, And R. G. Buchheit, “Stress Corrosion Cracking of Sensitized AA5083 (Al-4.5Mg-1.0Mn)”, *Materials Science Forum*, Vols. 396-402, (2002), 1437-1442.
17. J. S. Vetrano, D.R. Baer and R.H. Jones, “Solute Segregation and β-phase Precipitation at Internal Interfaces in AA5083”, in Automotive Alloys II, *TMS Annual Meeting*, Sam Antonio, TX, S.K. Das, ed., TMS, Warrendale, PA, (1998), 117-123.

18. J. R. Pickens, J.R. Gordon and J.A.S. Green, “The Effect of Loading Mode on the Stress Corrosion Cracking of Aluminum Alloy 5083”, *Mettalurgical Transaction A*, Vol. 14A, (1983), 925-930.
19. J. S. Vetrano, D.R. Baer and R.H. Jones, in “Automotive Alloys II”, edited by S.K. Das, *TMS Annual Meeting*, Orlando, FL (The Minerals, Metals and Materials Society, Warrendale, PA), (1997), 77.
20. R. A Corbett, B. J. Saldanha, “Metals Handbook: Corrosion”, 9th ed., Vol. 13, *ASM International*, Metals Park, OH, (1998).
21. Talbot and Talbot, Corrosion and Technology, CRC Press Boca Raton Boston, New York Washington London, (1998).
22. J. R. Davis, Aluminum and Aluminum alloys, (1999).
23. D. Craig and S. David, Corrosion Data, *ASM International*, Material Park, 2nd ed., (1995), 18-25.
24. ASM Handbook, *ASM International*, Metals Park, OH, 9, (1995), 352.
25. R. H. Jones, Stress Corrosion Cracking, *ASM International*, Materials Park, Ohio, (1992).
26. D. A. Jones, Principles and Prevention of Corrosion, Prentice Hall Inc., New Jersey, (1996).
27. A. F. Beck and P. R. Sperry, “Fundamental Aspects of Stress Corrosion Cracking”, *National Association of Corrosion Engineers*, Houston, TX, (1969), 513-521.
28. F. King, Aluminum and its Alloys, Ellis Horwood, Ltd, Chichester, (1987).
29. J. E. Hatch, Aluminum: Properties and Physical Metallurgy, *America Society for Metals*, Metals Park, Ohio, (1998).
30. F. W. Smith, Structure and Properties of Engineering Alloys 2nd ed., McGraw-Hill Inc., New York, (1993).
31. T. A. Michalske and S. W. Freiman, “A Molecular Interpretation of Stress Corrosion in Silica” *Nature*, Vol. 295, (1982), 511-512.
32. A. Jones, Principles and Prevention of Corrosion, second edition, Prentice Hall, Upper Saddle River, (1996).

33. J. F. Fellers and B. F. Kee, “Crazing Studies of Polystyrene. I. A New Phenomenon Logical observation” *Journal of Appl. Polymer Science*, Vol. 18, (1974), 2355-2365.
34. E. H. Andrews, Developments in Polymer Science, *Applied Science*, (1979).
35. H. T. Sumison and D. P. Williams, in Fatigue of Composite Materials, STP 569, *American Society for Testing and Materials*, (1975), 226-238.
36. C. Zeben, in Analysis of the Test Methods for High Modulus Fibers and composites, STP 521, *American Society for Testing and Materials*, (1973), 65-73.
37. E. Mattsson, Basic Corrosion Technology for Scientists and Engineers, Chichester: Ellis Horwood; New York : Halsted Press, (1989).
38. R. B. Mears, R. H. Brown and E. H. Dix, Jr., “A Generalized theory of the Stress Corrosion of Alloys”, in *Symposium on Stress Corrosion Cracking of Metals*, ASTM and AIME, (1945), 323-344.
39. D. O. Sprowls and R. H. Brown, “Stress Corrosion Mechanisms for Aluminum Alloys”, *Fundamentals aspects of Stress Corrosion Cracking*, NACE, (1969), 466-506.
40. M. O. Speidel, “Current Understanding of Stress Corrosion Crack Growth in Aluminum Alloys”, *The Theory of Stress Corrosion Cracking in Alloys*, NATO, (1971), 289-342.
41. R. J. Dest and A. R. Troiano, “Stress Corrosion and Hydrogen Embrittlement in an Aluminum Alloy”, *Corrosion*, Vol. 30 (1974), 274-279.
42. J. Albrecht, “Hydrogen Embrittlement of a High Strength Aluminum Alloy”, *Scripta Metallurgica*, Vol. 11, (1977), 893-897.
43. G. H. Koch, “Hydrogen Induced Fracture of a high Strength Aluminum Alloy”, *Corrosion*, Vol. 35, (1979), 73-78.
44. J. A. S. Green, H. W. Hayden and W. G. Montague, “Influence of Loading Mode on the Stress Corrosion Susceptibility of Various Alloy/Environment Systems”, *Effects of Hydrogen on Behaviour of Materials*, AIME, (1976), 200-209.

45. G. M. Scamans, R. Alani and P. R. Swann, “Pre-Exposure Embrittlement and Stress Corrosion Failure in Al-Zn-Mg Alloys”, *Corrosion Science*, Vol. 16, (1976), 443-459.
46. C. D. S. Tuck, “Evidence for the Formation of Magnesium Hydride on the Grain Boundaries of Al-Mg and Al-Zn-Mg Alloys During Their Exposure to Water Vapor”, Third Conference on the Effect of hydrogen on Behavior of Materials, AIME, (1980).
47. R. K. Viswanadham, T. S. Sun and J. A. S. Green, “Influence of Moisture Exposure on the Compositions of Oxides on Al-Zn-Mg Alloy: An Auger Electron Spectroscopy Study”, *Corrosion*, Vol. 36, (1980), 275-278.
48. R. M. Parkins, *Material Science and Technology*, Volume 1, (1985), 480.
49. K. Tamaki, S. Tsujikawa and Y. Hisamatsu, in advancesin Localized Corrosion, H. S. Isaacs and V. Bertocci, Ed., *National Association of corrosion Engineers,* (1988).
50. R. M. Riecke, A. Athens, and I. O. Smith, *Mater. Sci. Technol*., Vol. 2, (1986), 1066-1075.
51. W. L. Fink and L. A. Willey, “Quenching of 75S Aluminum Alloy”, Met. Technol., Vol.14, No. 8, (1947), 5.
52. M. S. Hunter, G. R. Frank and D. L. Robinson, in proceedings of Conference: Fundamentals Aspects of Stress-Corrosion Cracking, R. W. Staehle, NACE, (1969), 497.
53. M. E. Holmberg and T. V. Bruno, “Metallurgy and the New Corrosion Engineer: What He Should Know About Corrosion Induced Failures”, *Mater. Protect.*, (19966), 8.
54. C. L. Brient, Stress Corrosion Cracking, in Metallurgical Aspects of environmental Failures, Elsevier Science, (1985).
55. H. L. Logan, The Stress-Corrosion Cracking of Metals,John Wiley, New York, (19966).
56. H. H. Ulig and R. W. Revie, Corrosion and Corrosion Control, 3rd ed., Wiley Interscience, (1985).

57. J. E. Truman, “Stress Corrosion Cracking of Martensitic and ferritic Stainless Steels”, *Int. Met. Rev.*, Vol. 6, (1981), 301.

58. D. R. McIntyre and C. P. Dillon, Guidelines for Preventing Sress Corrrosion cracking in the chemical process Industries, MTI Publ. No. 15, Materials Technology Institute of the Chemical Process Industries, (1985), 108.

59. E. H. Dix, W. A. Anderson and M. B. Shumaker, “Influence of Service Temperature on the Resistance of Wrought Aluminum-Magnesium Alloys to Corrosion”, *Corrosion*, Vol. 15, 1959, 55-62.

60. D. Altenpohl, Aluminum and Aluminiumlegierungen, Springer-Verlag, (1965), 680.

61. A. Giarda, M. Paganelli, Aluminum, Vol. 46, No. 9, (1970), 639.

62. L. Zhaoqi, J. Jiaren, Z. Gang and R. Huongqiang “Effect of Intergranular Segregation of Mg on the Exfoliative Corrosion in Al-Mg Alloys”, *Colloque de Physique*, Vol. 1, No. 1, (1990), 575-580.

63. G. M. Scamans, N. J. H. Holroyd and C. D. S. Tuck, “Role of Magnesium Segragation in the Intergranular Stress Corrosion Cracking of Aluminum Alloys”, *Corrosion Science*, Vol. 27, n 4, (1987), 329-347.

64. G. M. Scamans, R. Alani and P. R. Swann, “Pre-Exposure Embrittlement and Stress Corrosion Failure in Al-Zn-Mg Alloys”, *Corrosion Science*, Vol. 16, (1976), 443-459.

65. J. R. Flores, H. Terryn, O. Steenhaut, and J. H. W. De Wit, “Influence of Mg Enrichment in the Corrosion Behavior of Al-Mg Alloys, *Electrochemical Society Proceedings*, Vol. 23, (2003), 131-140.

66. C. Lea and C. Molinari, “Magnesium Diffusion, Surface Segregation and Oxidation in Al-Mg Alloys”, *Journal of Materials Science*, Vol. 19, n7, (1984), 2336-2352.

67. F. J. Esposto, C. S. Zhang, R. R. Norton and R. S. Timsit “Segregation of Mg to the Surface of an Al-Mg Single Crystal Alloy and Its Influence on the Initial Oxidation at Room Temperature”, *Surface Science*, Vol. 302, n 1-2, (1994), 109-120.

68. R. G. Song, “Grain Boundary Segregation and Hydrogen-Induced Fracture in 7050 Aluminum Alloy”, *Acta Mater.*, 44, (1996), 3241.
69. R. C. Weast, “CRC Handbook of Chemistry and Physics”, 67th edition, CRC Press, Boca Raton, (1987), E42.
70. G. M. Scamans, N. J. H. Holroyd and C. D. S. Tuck, “Role of Magnesium Segragation in the Intergranular Stress Corrosion Cracking of Aluminum Alloys”, *Corrosion Science*, Vol. 27, n 4, (1987), 329-347.
71. J. C. Chang and T. H. Chuang, “Degradation of Corrosion Resistance for Al 5083 Alloy after Thermal and Superplastic Forming Processes”, *Journal of Materials and Engineering and Performance*, Vol. 9, n 3, (2000), 253-260.
72. Standard Test Methods for Tension Testing Wrought and Casting Aluminum and Magnesium- Alloy Products [Metric][1], ASTM B557-02a, (2003).
73. Standard Test Method for Determining the Susceptibility to Intergranular Corrosion of 5XXX Series Aluminum Alloys by Mass Loss After Exposure to Nitric Acid (NAMLT Test), ASTM G 67, (2003).
74. Standard Practice for Preparing, Cleaning and Evaluating Corrosion Test Specimens, ASTM G 1, (2003).
75. Standard Practice for Preparation and Use of Bent-Beam Stress-Corrosion Test Specimens, ASTM G 39, (2003).
76. A. Thornton and Vito J. Colangelo, Fundamentals of Engineering Materials, Prentice-Hall, Inc., Englewood Cliffs, New Jersey, (1985).
77. D. Callister, Jr., Fundamentals of Materials Science and Engineering, Fifth Ed., John Wiley & Sons, (2001).
78. James, F. Shackelford, Introduction to Materials Science for Engineers, Fifth edition, Prentice Hall, New Jersey, (2000).
79. http://www.key-to-metals.com/Articles.htm (08/02/2006).
80. J. A. Vander Hoever, L. Zhuang, Ijmuiden, B. Schepers, P. Desmet, J.P. Baekelandt and Duffel, “A New 5xxx series Alloy Developed for Automotive Applications”,Aluminum, 78, Jahrgang, 9, (2002), 750-754.
81. E. C. W. Perryman and S. E. Hadden, *J. Inst. Metals*, (1950), 77, 207-216.

82. M. S. Ray, The Technology and Applications of Engineeering Materials, Prentice-Hall international, UK, (1987).

83. http://asm.Matweb.com/search/SpecificMaterial.asp?bassnum=MA5083H116 (26/12/2005).

84. Cambridge Engineering Selector 4.0 (CES), Granta Design Ltd, Cambridge, UK.

APPENDIX

A. Average values for hardness measurements

A1. Average values of hardness measurements (VHN) and standard deviation (STD) along the longitudinal direction.

Sensitization time (h)	100°C	STD	150°C	STD	175°C	STD	200°C	STD
0.001	97.1133	1.8084	97.1133	1.8084	97.1133	1.8084	97.1133	1.8084
0.500	94.7267	0.8536	93.6400	1.3276	92.2067	1.2364	89.3400	1.5112
1.000	93.4733	1.0786	93.0867	0.7745	92.5400	1.3032	89.7800	1.3848
2.000	92.9867	1.5461	92.6600	1.7412	90.8333	1.2647	89.0467	1.1904
4.000	93.4067	1.3815	93.2267	1.5377	91.0467	1.4123	89.8533	1.1194
8.000	92.7400	1.7246	92.2267	2.1965	90.7667	1.5713	90.7000	1.4076
24.000	92.2333	1.0768	91.8400	1.4407	90.8933	1.2052	87.9467	1.7370
48.000	92.6733	1.6450	92.2867	1.6725	90.4000	1.0165	89.5600	1.2419
168.000	91.6333	1.1417	91.0867	1.1014	88.7000	1.5967	88.0533	1.4687
336.000	91.0933	1.5255	90.7400	1.6637	87.5133	1.7427	87.3533	0.6622
504.000	90.0400	1.3425	89.1933	1.5528	87.3733	1.2709	87.1333	1.7126
672.000	89.8533	1.3371	89.0000	1.4496	86.9400	1.1932	86.8333	1.5274

A2. Average values of hardness measurements (VHN) and standard deviation (STD) along the transverse direction.

Sensitization time (h)	100°C	STD	150°C	STD	175°C	STD	200°C	STD
0.001	95.1267	3.1535	95.1267	3.1535	95.1267	3.1535	95.1267	3.1535
0.500	93.0533	1.6709	91.7867	2.7599	91.5800	1.5285	89.4400	1.4840
1.000	92.8000	1.4733	91.6467	2.4022	90.5533	1.7181	89.9867	2.0126
2.000	92.0067	1.6703	91.1533	1.7378	89.8000	2.4405	89.2800	1.1873
4.000	91.7200	2.8428	91.7200	2.8428	88.6267	1.9868	89.5533	1.3510
8.000	92.3000	0.7598	90.3067	1.8182	89.8733	1.7729	90.6533	2.3715
24.000	91.5333	1.2836	90.7800	1.6742	89.0600	1.7381	88.8133	1.5143
48.000	91.3200	1.8056	90.1400	1.9933	88.5200	1.0998	89.5267	1.7027
168.000	90.7200	1.4721	89.7133	1.6788	89.5800	2.1154	87.5200	1.6995
336.000	91.9667	1.0268	90.6800	1.6916	88.2667	2.2564	88.1400	1.7181
504.000	90.6333	1.3400	90.3533	1.6840	87.5333	1.8571	87.6667	1.7059
672.000	90.1533	1.4509	88.3867	1.1882	86.9000	1.5591	86.5667	2.0726

B. Variation of hardness along the longitudinal (LD) and transverse (TD) directions
with sensitization time.

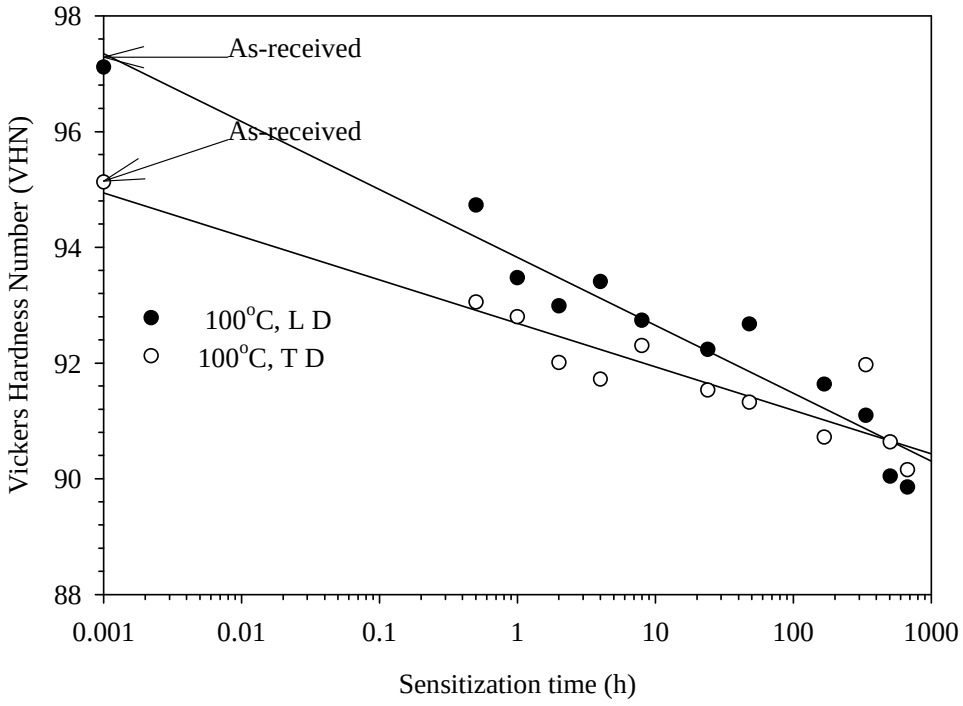

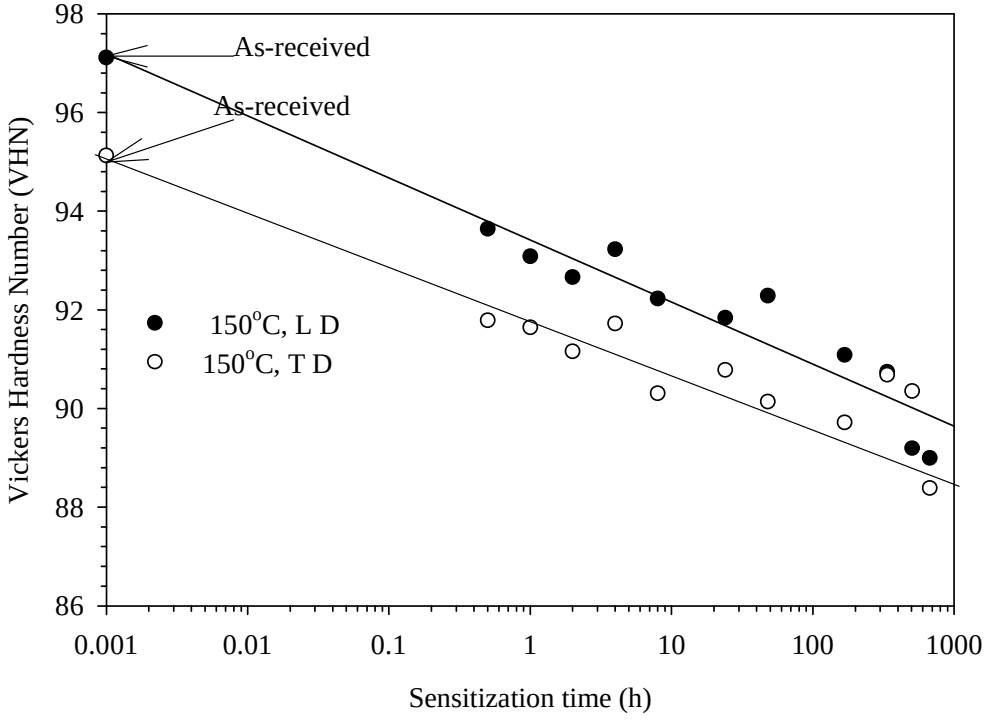

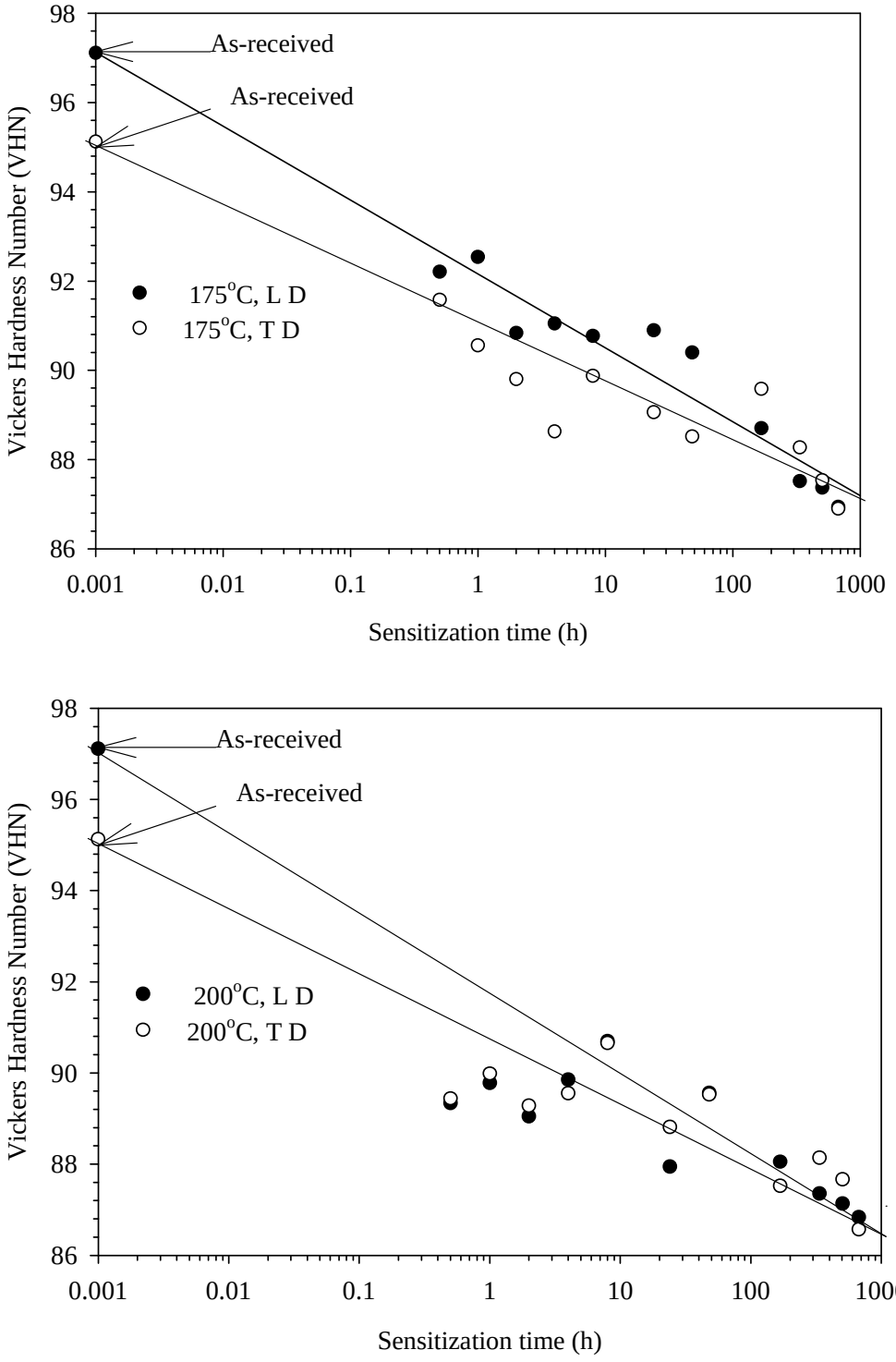

Figure B. Variation of hardness with sensitization time.

C. Average values and standard deviation of tensile and yield strength.

C1. Average values and standard deviation of tensile strength.

Sensitization time (h)	100°C	STD	150°C	STD	175°C	STD	200°C	STD
0.001	341.6667	1.9993	341.6667	1.9993	341.6667	1.9993	341.6667	1.9993
1.000	342.8209	0.0000	342.8209	0.0000	342.8209	0.0000	342.8209	0.0000
8.000	342.8209	0.000	342.8209	0.0000	338.2038	1.9993	338.2038	2.6448
24.000	341.6667	1.9993	342.8209	0.0000	338.0124	0.9996	338.2038	1.9993
168.000	342.8209	3.4628	341.0895	2.9989	337.0495	2.6448	337.0495	1.9993
336.000	342.8209	0.0000	338.7810	2.6448	334.7410	1.9993	328.3924	0.9996
504.000	341.0895	2.4486	338.2038	1.9993	331.2781	1.9993	323.1982	0.9996
672.000	338.2038	7.9971	335.3181	1.9993	327.8153	1.9993	320.8896	0.9996

C2. Average values and standard deviation of yield strength.

Sensitization time (h)	100°C	STD	150°C	STD	175°C	STD	200°C	STD
0.001	248.0000	7.2111	248.0000	7.2111	248.0000	7.2111	248.0000	7.2111
1.000	242.3330	2.3094	240.0000	3.4641	236.0000	5.1962	234.6667	8.6217
8.000	241.6667	7.7675	237.3333	4.0415	235.3330	6.5036	230.0000	7.0000
24.000	243.3333	5.0332	235.0000	7.0000	231.6667	3.2146	229.0000	5.2915
168.000	242.6660	7.0664	228.6667	8.2753	226.0000	6.2450	219.6667	7.6376
336.000	242.0000	5.2915	226.3333	9.6090	220.6667	4.7258	213.3333	9.0738
504.000	237.0000	3.6056	225.3333	1.5275	216.0000	6.5326	201.6667	4.1633
672.000	234.6667	4.6188	214.3333	7.5056	212.0000	4.5092	201.3333	5.6862

D. Average values and standard deviation of percentage of elongation.

Sensitization time (h)	100°C	STD	150°C	STD	175°C	STD	200°C	STD
0.001	14.4533	2.0260	14.4533	2.0260	14.4533	2.0260	14.4533	2.0260
1.000	14.4000	0.5657	15.6000	0.5657	14.0000	2.8284	16.0000	0.0000
8.000	14.1733	0.5001	14.0000	0.0000	18.4000	2.1166	14.6667	3.0551
24.000	14.0000	1.0583	15.3333	2.3094	15.3333	1.1547	16.6667	2.3094
168.000	13.5467	0.9246	19.3333	2.3094	14.0000	2.0000	14.6667	2.3094
336.000	14.0800	0.9457	15.3333	1.1547	19.3333	1.1547	19.2000	1.3856
504.000	14.2600	0.1980	16.2000	0.2828	16.0000	2.8284	17.8000	1.9799
672.000	14.0000	2.0000	16.0000	0.0000	18.6667	2.3094	18.0000	2.0000